Robust Magnetic Resonance Temperature Mapping for Real-Time Guidance of Interventional Therapies

By

Megan Elizabeth Poorman

Dissertation

Submitted to the Faculty of the

Graduate School of Vanderbilt University

in partial fulfillment of the requirements

for the degree of

DOCTOR OF PHILOSOPHY

in

Biomedical Engineering

August 31, 2018

Nashville, Tennessee

Approved:

William A. Grissom, Ph.D.

Adam W. Anderson, Ph.D.

Charles F. Caskey, Ph.D.

Mark D. Does, Ph.D.

E. Brian Welch, Ph.D.

DEDICATION

To Grandmary and Grandbob

ACKNOWLEDGMENTS

When I decided to attend Vanderbilt for my graduate studies I knew I was committing to a top-ranked university with stellar research and close medical collaborations. What I didn't realize was how much the university invested in the growth of its students. In my time as a PhD student at Vanderbilt I've traveled the world to present at conferences, attended workshops to learn about new areas of my field, and spent time living in another country collaborating with world-renowned researchers. These experiences have changed the course of my research career and would not have been possible without the constant encouragement and unwavering support of my mentors at Vanderbilt. I am continually amazed at the level of investment that my advisor, Dr. Will Grissom, devotes to his students. Whether it be juggling multiple interdisciplinary projects, sending me to workshops and conferences solely for my own development, or enthusiastically supporting my decision to apply for a research grant abroad, he has, without fail, always had my back. I am incredibly fortunate to have worked with such a positive, encouraging, and intelligent mentor.

I cannot talk about mentors without mentioning Dr. Charles Caskey and Dr. Crystal Coolbaugh who served as great sources of advice, collaboration, inspiration, and friendship throughout my time in Nashville. Dr. Chrit Moonen and Dr. Wilbert Bartels of the UMC Utrecht took the chance on me as a foreign graduate student and, along with countless others, made my time on the Whitaker Grant in the Netherlands unforgettable and productive. I want to thank my committee members, Dr. Adam Anderson, Dr. Mark Does, and Dr. Brian Welch, and the entire VUIIS for cultivating the collaborative and pioneering environment that convinced me to come to Vanderbilt. The culture here has encouraged me to succeed and made my time here impactful, both in the lab and in everyday life. I must also acknowledge Dr. Michael Miga and Dr. Dan Brown, and Michelle Bukowski of VISE who opened up my world to clinical relevance, interdisciplinary collaboration, and public outreach. I also want to thank my many collaborators across the school of engineering and medical center without whom much of this work would not have been possible.

A huge thank you goes to my parents, Peter and Stephanie Poorman, and brother, David Poorman, who always told me that I could do anything I set my mind to, celebrated our birthday candles in binary, and sent me never-ending care packages of tortillas. I am overwhelmingly grateful for my friends, both near and far, who have supported me through this Ph.D. Ali Senz, Erin Reas, and Haley Nickel all deserve awards for putting up with my overall mental exhaustion on phone calls and reminding me of home. My graduate school cohort, especially Meredith Jackson, Evan Kazura, Jeremy Ford, and Kristy Walsh reminded me to celebrate the small things and that a good round of volleyball cured all. All of the members of the Grissom lab (Anuj Sharma, Pooja Gaur, Julianna Ianni, Chris Hasselwander, Jun Ma, Sumeeth Jonathan, Charlotte Sappo, Huiwen Luo, Zhipeng Cao, and Xinqiang Yan) and the occupants the basement office (particularly Kurt Schilling, Aliya Gifford, Jason Ostenson, and Michael Pridmore) made our windowless dungeon an enjoyable place to be and proved to be great travel companions. My friends at the UMC Utrecht, particularly Julia Noordhout, Cyril Ferrer, and the bouldering crew, made me feel at home even though home was many time zones away. Finally, Jake Benzing, who played the roles of workout buddy, supportive partner, travel inspiration, and comic relief all at once. Without his love and companionship my time at Vanderbilt would not have been nearly as fun.

Parts of this dissertation appear in the following manuscripts:

Poorman, M, Chaplin, V, Wilkens, K, Dockery, M, Giorgio, T, Grissom, W, and Caskey, C, "Open-source, small-animal magnetic resonance-guided focused ultrasound system". Journal of Therapeutic Ultrasound 4(1):22, 2016. doi: 10.1186/s40349-016-0066-7

Poorman, M, Braškutė, I, Bartels, LW, and Grissom, W, "Multi-echo fat-suppressed MR thermometry using iterative separation of baseline water and fat images". (Under Revision)

TABLE OF CONTENTS

LIST OF TABLES

Table Page

LIST OF FIGURES

Chapter 1

INTRODUCTION

1.1 Clinical Motivation

Minimally-invasive thermal therapies, such as focused ultrasound, laser, microwave, and Radiofrequency (RF) ablation, are a viable alternative to more invasive surgical procedures. These interventional techniques can be used treat everything from cancer [1] to epilepsy [2], and can even be used for immunotherapy [3] and drug delivery [4]. These novel treatment mechanisms are set to change the standard of medical care from lengthy, invasive procedures to therapies that can selectively target and treat an area of interest while minimizing damage to healthy tissues. The selectivity provided by minimally-invasive options not only improves patient outcomes, but reduces recovery times and medical costs. Interventional techniques are widely available in a research setting, but current clinical practice has been slow to adopt these promising modalities. For thermal therapies, which are the focus of this dissertation, this slow percolation of technology into the clinic is due in part to a lack of robust, spatially-resolved temperature monitoring during treatment as well as a lack of studies demonstrating safety and efficacy over the wide variety of application areas.

Minimally-invasive thermal procedures are currently applied percutaneously under imaging guidance, often with X-ray Fluoroscopy, Computed Tomography (CT), ultrasound (US), or optical and electromagnetic tracking. However, these modalities only supply anatomical localization, may expose patients to harmful ionizing radiation (as is the case with CT), and offer a limited view of heat development and tissue changes during treatment. Some ablative systems intended for interventional use incorporate thermocouples into the ablation needle, but this provides only a single point measurement near the probe. Accurate, spatially-resolved temperature mapping is critical in order to assess the delivered thermal dose [5] and prevent unwanted damage to healthy tissue. Ultrasound imaging can provide tempera-

ture information through measuring changes in the speed of sound, attenuation coefficient, and backscattering [6]. However, US thermometry is limited in sensitivity, resolution, and imaging depth. Magnetic resonance imaging (MRI) can provide high resolution anatomical images with unparalleled tissue contrast in a real-time manner using non-ionizing radiation, irrespective of tissue geometry and slice orientation. Many MRI parameters also exhibit a sensitivity to temperature. These changes can be quantified from the acquired images dynamically during imaging, providing the necessary spatially-resolved temperature maps in real-time. Temperature mapping with MRI was first explored in the 1980s [7] and many MR Thermometry techniques have been developed for clinical use. However, currently most of these methods are limited to specific use cases in water-based tissues, such as brain or muscle, and fail in more difficult treatment scenarios such as in fatty breast tissues, during motion, and in the presence of time-varying magnetic fields. Additionally, the probes used for RF and microwave ablation (two of the most commonly used modalities) are often made from metallic materials that interfere with the MRI signal and create erroneous temperature maps. These sources of error are common in many treatment scenarios and must be addressed before MR-guidance of therapies in adipose tissues and near metal probes can be implemented.

The surgical devices used to perform minimally invasive thermal treatments are also undergoing rapid development. Conventional devices such as RF, microwave, and laser ablators require direct contact with the target tissue, which necessitates surgical access to target. The ablator must be inserted into the body percutaneously and may need to be reinserted multiple times to fully treat the desired volume of tissue. While the tissue damage caused by these incisions is small compared to that of open surgery, they could increase the risk of tumor seeding along the insertion path unless ablation of the insertion path is performed [8]. Focused ultrasound (FUS) is a therapeutic modality that has garnered interest due to its ability to heat tissues noninvasively from outside the body without damaging intervening healthy tissues. Coupled with MRI guidance, FUS can be used to induce bioeffects at a

specific location within the body, enabling a completely incision-less surgery. However, with the exception of a few applications, MR-guided focused ultrasound (MRgFUS) is still in the early stages of clinical development. More studies are needed to prove safety, efficacy, and mechanisms. In such a rapidly-developing field, experiments can be slow to progress due to the complexity, high cost, and a lack of well-validated, accessible systems for repeatability studies. A standardized entry-level pre-clinical MRgFUS system is needed to aid in the exploration of the impact of FUS therapy.

1.2 Dissertation Synopsis

In order to advance MRI-guided minimally-invasive therapies, this dissertation tackles these two specific barriers to progress:

1. Temperature errors in artifact-prone regions due to the presence of adipose tissue and metallic needles

2. The high cost and limited access to experimental pre-clinical MR-guided Focused Ultrasound systems

This includes the development of novel MR thermometry methods to perform online correction of temperature mapping errors in fatty tissues, pulse sequence development to recover image signal and temperature precision near metallic probes, and the design and validation of a custom MR-guided focused ultrasound system for preclinical studies.

Chapter 3 details a novel temperature mapping algorithm that enables proton resonant frequency-shift (PRFS) thermometry in the presence of adipose tissue. This algorithm combines model-based water/fat separation with model-based penalized-likelihood temperature estimation to account for the signals from both water and fat in real-time to overcome the computational and model limitations of existing methods. The method collects a baseline library of pre-treatment images over a range of motion states, performs water/fat separation

on those images, and then incorporates the separated baseline water and fat images into a heating image model, avoiding the need to perform water/fat separation on each heating image. Clinical implementation of this method would allow for robust treatment guidance in fatty tissues such as breast and liver and encourage further dual-constrast MR thermometry pulse sequence development.

Chapter 4 describes an MR imaging simulator that calculates images near metallic ablation probes and performs offline optimization of a novel multiple echo Z-shimmed pulse sequence. The simulator and optimized sequence recovers image signal and temperature precision near metallic ablation probes for guidance of thermal therapies. This work overcomes limitations of existing near-metal imaging approaches by using conventional gradient echo PRFS thermometry techniques and enabling pulse sequence optimization to be performed prior to imaging a patient on the scanner. This method will enable thermal guidance of ablative treatments using metallic probes in delicate environments where high temperature precision is needed near a probe, such as during hippocampal ablation for epilepsy management.

Chapter 5 covers the design, development, and validation of an open-source, small-animal MR-guided focused ultrasound system. This system was designed to perform closed-loop controlled hyperthermic sonication on murine models of cancer. The system consists of a low-cost machined plexiglass thermotherapy table, capable of holding an ultrasound transducer at isocenter within a small-bore MRI system, and a modular software distribution. The software provides real-time visualization of heating in the target tissues and closed-loop feedback to control the level of heating for an extended period of time. It was provided open-source to the focused ultrasound community as a start-up system to aid researchers in developing their own systems and application areas.

Chapter 2

BACKGROUND

2.1 MR Thermometry

2.1.1 MR Image Formation

MRI is a non-ionizing imaging modality that can provide high-resolution images of tissues in any orientation within the body. To form images, an object or patient is placed within the bore of a strong, static magnetic field. This causes protons within the subject to align with the magnetic field along the longitudinal axis, causing a bulk magnetization in the direction of the magnetic field. RF pulses are applied perpendicular to the magnetic field at the Larmor frequency which tips the protons away from the longitudinal axis towards the transverse plane. The protons will precess at the Larmor frequency as they relax back to their low energy state, inducing an electrical current in receiver coils placed around the subject which is measured and recorded. The relaxation of protons back to the longitudinal axis will differ depending on the local magnetic environment and the sequence of RF pulses and magnetic fields that are applied. This rate of relaxation can be described by the time constants T_1 and T_2 which describe the magnetization relaxation rates in the longitudinal and transverse planes, respectively.

To localize these electrical signals to a spatial location, gradient coils are used to apply linear magnetic fields within the magnet. The application of these gradients induces spatially-dependent frequency and phase shifts in the collected signal which are recorded in k-space, or frequency space. The signal from the RF coil is recorded as gradients are applied to traverse through k-space. Once filled, the k-space data is Fourier transformed to the spatial domain to generate an image of the object.

Since the invention of MRI in the 1970s, it has grown from a purely anatomic and

structural imaging modality to an adaptable tool capable of real-time functional measures and quantification. MRI's sensitivity to changes in temperature and ability to map them spatially on anatomical images in real-time has led to the field of MR Thermometry.

2.1.2 Temperature-sensitive MRI parameters

Many MR parameters have a dependence on temperature including the longitudinal and transverse relaxation rates (T_1 and T_2), the apparent diffusion coefficient (ADC), the magnetization transfer rate (MT), the proton density (PD), and the proton resonant frequency-shift (PRFS). Both the MT and PD are rarely used for temperature mapping due to limited sensitivity while the ADC, relaxation rates, and the PRFS all have high sensitivity to the PRFS. The ADC has good sensitivity to temperature but requires long scan times and can be confounded by non-linearities that occur when tissue properties change, as might be the case during heating due to coagulation. Temperature mapping with relaxation rates has good accuracy and sensitivity but can require long scan times to measure the rates. They have been used in aqueous tissues but have been most useful in adipose tissue. The PRFS is widely used to map temperature in water-based tissues due to its linearity with temperature over a clinically-relevant range (-15°C to 100°C) [9] and independence of underlying aqueous issue type and coagulation [10]. The next sections will discuss PRFS thermometry, thermometry in fat, and challenges faced during thermometry near metal.

2.1.3 PRF-shift Thermometry

Figure 2.1 demonstrates how heating induces a PRFS. As water is heated, molecular motion increases and the hydrogen bonds between molecules begin to stretch and break. This decrease in hydrogen bonding causes the electrons to sit closer to the hydrogen nucleus, effectively shielding it from the main magnetic field, B_0. The shielding reduces the local magnetic field, B_{loc}, causing a decrease in the resonant frequency of water, ω_0, such that the affected molecule now resonates at a lower frequency, ω_{loc} [11]. This change in resonant

frequency changes gradient echo image phase. The PRFS varies linearly with temperature in aqueous tissues at a rate of $\alpha = -0.01 ppm/°C$.

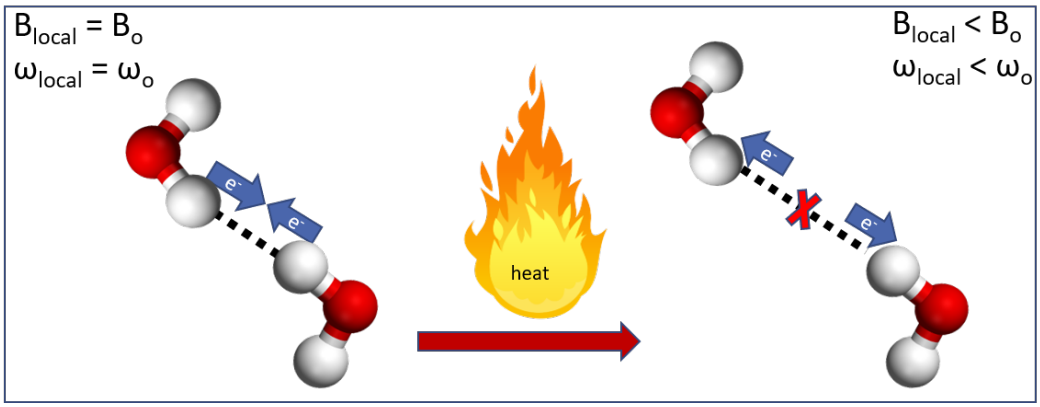

Figure 2.1: The proton resonant frequency shift with heating. As heat is applied, the resonant frequency decreases.

PRFS temperature maps are typically acquired using a gradient-recalled echo (GRE) pulse sequence that acquires a set of baseline images prior to heating and a time series of images during heating. The phase difference between a baseline and heating image is proportional to temperature. Alternatively, spectroscopic techniques can be used to directly measure the shift in water resonance. Spin echo images, which inherently refocus the dephasing caused by the resonant frequency shift, cannot be directly used for PRFS temperature mapping.

2.1.3.1 PRF-shift phase mapping algorithms

The phase difference between the baseline and heating images is proportional to the PRFS [12] and can be converted to temperature using Equation 2.1,

$$\Delta T = \frac{\Phi(T) - \Phi(T_0)}{\gamma \alpha B_0 T E} \tag{2.1}$$

where ΔT is the temperature change in °C, Φ is the image phase map at heating temperature T or baseline temperature T_0, γ is the gyromagnetic ratio in MHz per Tesla, B_0 is the magnetic field strength in Tesla, and TE is the echo time in seconds. Direct subtraction of image

phase is straightforward to compute but is prone to errors resulting from spatiotemporally varying sources of distortion, including off-resonance, tissue motion, and respiration. Many approaches have been reported that make PRFS thermometry more robust to these sources of error [13, 14, 15, 16, 17, 18, 19]. Another challenge is the presence of fat in heated voxels. Since fat experiences a much smaller PRFS with temperature than water, the presence of both species within a voxel can corrupt the PRFS measurement [20]. This is particularly a problem when monitoring therapies such as focused ultrasound ablation of breast tumors, which are highly embedded in adipose tissue [21].

PRFS measurements require only a single echo, but acquiring multiple echoes can mitigate some sources of error. The long echo times required to obtain high temperature SNR ($TE \approx T_2^*$ [22]) can result in phase (and subsequently temperature) wrapping whenever the frequency shift exceeds the spectroscopic bandwidth of 1/TE [23]. Including multiple echoes in the readout increases the spectroscopic bandwidth, resulting in a larger range of temperatures that can be measured without phase wrapping. Using multiple high-bandwidth echoes can also mitigate geometric distortions due to chemical shift [18], increase temperature SNR, and provide sensitivity to other chemical species such as adipose tissue [23].

2.1.4 Thermometry in Adipose Tissue

To prevent temperature errors due to fat, PRFS temperature mapping typically uses spectral-spatial pulses to obtain water-only images [24, 25]. However, these pulses are sensitive to off-resonance and place a lower limit on slice thickness [12]. An alternative is to use multiple gradient echo imaging sequences to separate water and fat signals computationally, and use the fat signal as a heat-insensitive reference for off-resonance compensation. Water/fat separation in anatomic imaging has been used to separate the short T_1 fat signal from that of water in order to better visualize important clinical structures such as tumors or edema [26]. Separating each tissue type can also be used to provide quantitative information about tissue composition for disease characterization [27]. State-of-the-art water/fat

separation approaches expand upond conventional three-point Dixon method [28, 29] and produce separations with excellent robustness to off-resonance [30, 31, 32]. However, these approaches are too computationally expensive to be applied in real-time to each image in a heating time series. A secondary problem is that these methods assume a fixed frequency difference between water and fat and therefore produce increasingly erroneous separations as water is heated (Figure 2.2). Therefore, alternative methods have been explored to perform thermometry in adipose tissue. Spectroscopic and fat-referenced methods use fat as a standard by which to correct PRFS errors in mixed water and fat tissues, while relaxation-based methods directly measure the temperature of the fat.

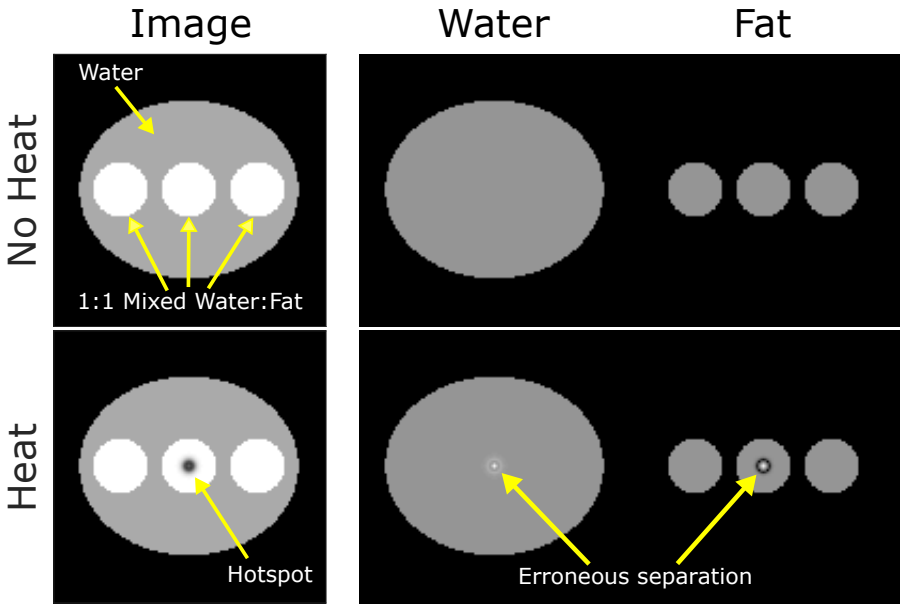

Figure 2.2: Conventional water/fat separation algorithms can fail in the presence of heating. In a simulated phantom, iterative separation (Ref. [32]) accurately separates the water and fat without any heating present. When a hotspot is placed in the mixed voxels, the separation fails since the assumed frequency difference between water and fat has changed.

2.1.4.1 Spectroscopic Methods

Phase-mapping thermometry techniques are fast but provide only relative thermometry measures. Absolute thermometry can be obtained by examining the spectra of each voxel's

signal. Spectroscopic approaches have been used in thermometry previously to measure the chemical shift of the water resonance [33]. These methods are inherently robust to tissue motion and susceptibility changes but require the acquisition of many echoes. They also require fat to be present in every voxel which would not be the case in heterogeneous tissues such as the breast [34]. Additionally, sprectroscoptic thermometry implementations suffer from low spatial resolution and long scan times [35]. In adipose tissues where the PRFS is known to fail, the limitations of spectroscopic techniques could be outweighed by their inherent sensitivity to fat. Since the fat resonance peak is insensitive to temeprature, spectroscopic methods use the water frequency shift to calculate temperature and frequency shifts that occur to both the water and fat to account for B_0 field fluctuations [36]. Techniques have been proposed to increase the temporal and spatial resolution of these methods, including echo planar imaging [37, 38] and moving average filters with Fourier-based computation of the temperature maps [39]. With such modifications, spectra can be acquired with as few as 16 echoes in 5 s per image [39]. Computation time is on the order of 11 ms per image voxel, which may not be feasible for online implementation but could be useful for imaging scenarios not requiring real-time therapy guidance [40]. Novel spectroscopic methods are being explored for applications such as brown adipose tissue monitoring [41] and in bone where low SNR for PRFS prevents monitoring [42].

2.1.4.2 Fat-referenced Methods

Fat-referenced approaches [43, 44, 45] are most closely related to Chapter 3 since they comprise an explicit water/fat separation step and can operate with a small number of echoes (as few as three). IDEAL-based fat-referenced methods work by applying IDEAL water/fat separation [46] to a baseline image to obtain water and fat phase images along with an off-resonance map. The baseline off-resonance map is held fixed and used to separate water and fat signals during heating. Temperature is measured from the phase difference between the baseline and heating water images. The phase differences between the baseline

and heating fat images are used to measure dynamic off-resonance changes and subtract them from the water phase difference. Hofstetter et. al [44] further extrapolated the fat phase shifts to voxels without fat so that fat signal need not be present in every voxel to apply an off-resonance correction. However, motion-robust versions of these IDEAL-based methods have not been developed, and the fat phase difference extrapolation can introduce errors if fat is not uniformly distributed over the imaged volume. A secondary problem is that, like anatomic water/fat separations, these IDEAL-based methods assume a fixed frequency difference between water and fat, meaning they can produce increasingly erroneous separations with increasing temperature. This effect is mitigated somewhat by keeping the baseline B_0 and R_2^* maps constant but, as is shown in this dissertation, errors can persist in areas of large frequency changes.

2.1.4.3 Relaxation-based Methods

Longitudinal (T_1) and transverse (T_2) relaxation are both sensitive to temperature changes. The first report exploiting this relationship in 1983 derived a relation such that an increase in temperature caused a proportional increase in T_1 [7]. However, subsequent studies have observed non-linearity in the relationship of T_1 and temperature near the tissue coagulation threshold. Upon cooling, there is a hysteresis of the temperature relationship due to tissue changes and the relationship between T_1 and temperature must be calibrated for each tissue type. These trends hold true in adipose tissues, where the relation between T_1 and temperature is highly dependent on the chemical makeup of the fat being imaged [47]. T_1 and temperature in fat have a linear relationship below 40 °C of heating. Above that, irreversible tissue changes cause non-linearity and hysteresis. This change to nonlinearity could potentially be used as an indication of treatment efficacy and tissue coagulation [12]. In order to perform T_1-based thermometry in adipose tissue, the T_1 must be quantified accurately. Inversion recovery sequences traditionally used for T_1 mapping are too slow for real-time applications. A variable flip angle approach is feasible as long as differences in

steady state are accounted for [48]. Alternatively, T_1-weighted images can be used directly to correlate changes in signal intensity [49]. In both cases, calibration of the relationship between observed change and actual temperature is required for each tissue type.

T_2 also exhibits an increase with temperature, but has been disregarded in aqueous tissues since the dependence is usually masked by stronger factors. In adipose tissue, the effect is stronger than that in water and changes approximately 5 ms per °C [50, 51]. There is a linear relationship between T_2 and temperature so long as the water signal is fully suppressed and the temperature remains below 45 °C of heating. T_2 changes in adipose tissues exhibit little hysteresis due to the reversible phase transition of triglycerides [47]. However, the change in T_2 must be calibrated for each tissue type being imaged. The calibration is repeatable between samples of the same type, as has been shown in breast tissue [52]. The effective T_2 (T_2^* in practice) can be measured from the signal decay in multiple gradient echo sequences already used for PRFS temperature mapping [50].

2.1.4.4 Fat Susceptibility

A final confounding factor when performing MR thermometry in mixed fatty tissues is the change in magnetic susceptibility of fat with heating. Fat exhibits a susceptibilty change of approximately 0.008 ppm/°C [20]. While this effect is small, at large temperature changes this term can become a significant confound in PRFS thermometry [53, 54]. The field caused by this susceptibility difference extends outside the fat in a manner dependent upon its orientation within the magnetic field [55], making its effect difficult to predict and correct in MR thermometry [56]. A method has been proposed that corrects these errors using T_1 changes in fat to measure heating and predict the subsequent PRFS errors [57]. Dependending on the application, tissue geometry, and heating level these effects may be negligible and are ignored by most thermometry implementations.

2.1.5 Dual-contrast sequences

Both fat and water contain potentially useful information for guidance of thermal therapy and no one MR parameter universally provides information about both tissues. As such, there is a focus on creating dual-contrast sequences that are sensitive to both the PRFS and changes in T_1 with temperature, for use in water and fat respectively. Typically these sequences build off a gradient echo sequence to generate PRFS contrast and alternate the flip angle every other image to generate T_1 sensitivity [48, 58]. The long TE and short repetition time (TR) required by PRFS is at odds with the short TE and long TR needed by the T_1 calculation. Parameters such as flip angle, TR, and TE must be optimized to obtain high temperature SNR for both mechanisms. To address this issue multiple echoes can be used to provide sensitivity to both [59]. Recently a 3D undersampled multi-echo sequence was proposed with volumetric sensitivity to changes in the PRFS, T_2^*, and initial signal magnitude [45]. This method is a promising approach for whole-volume thermometry of both tissue types with less than 2 seconds acquisiton time, but has increasing error during respiration and in voxels containing mixed tissue types. Dual-contrast thermometry has the potential to combine the advantages of PRFS thermometry with fat monitoring, enabling MR guidance of thermal therapies in many organs.

2.1.6 Temperature mapping near metallic objects

The accuracy and precision of PRFS thermometry is highly dependent on image SNR [22]. The devices used for ablation are made from materials that have a different magnetic susceptibility than tissue, creating local B_0 inhomogeneities due to susceptibility mismatch. These local inhomogeneities cause in-plane and through-slice distortion [60]. Spin echo imaging suffers distortions but has less signal loss near metal than gradient echo sequences since the dephasing caused by the probe is inherently refocused. Techniques such as slice encoding [61], multispectral imaging [60], and view angle titling [62, 63] have been developed

that reduce these image distortions. T_1-based thermometry methods have been proposed for imaging near metallic implants [64, 65] that employ multispectral imaging techniques [66, 67] to correct for the induced susceptibility artifact. While they outperform conventional PRFS MR thermometry near the metallic object, with image acquisition times ranging from 15 seconds to tens of minutes, their temporal resolution is too slow for real-time monitoring. Additionally, the T_1-mapping technique demonstrated in Ref. [65] saw an unwanted reduction in temperature precision far away from the metal artifact. This method was also used to reduce artifacts near biopsy needles, without heating, for improved localization [68]. A recent update to the multispectral thermometry method incorporated image undersampling to accelerate the acquisition during a focused ultrasound monitoring [69]. However, these methods require calibration of the relationship between T_1 and temperature to perform relaxation-based thermometry, which can be a non-trivial task in the face of mixed tissue types and field inhomogeneities. Furthermore, these methods were developed for artifact correction near large metallic implants that produce much greater distortion than is seen near high-gauge ablation probes and may be overkill for this application.

When a gradient echo sequence is applied, the field inhomogeneities cause dephasing of the magnetiziation near the device, resulting in complete signal loss near the device [70, 71, 72]. For ablation probes, this artifact can extend over a centimeter from the probe, occurring exactly where the area of maximal heating occurs. This leads to unreliable PRFS temperature data and prevents treatment guidance in the region [73]. This is particularly a concern for applications in the brain where precise targeting of the desired region and the safety of nearby delicate structures must be ensured. For example, monitoring is critical during hippocampal ablation for the treatment of epilepsy [74] or RF safety evaluation of heating near implanted electrodes [75]. Even a 2.5 mm diameter nitinol needle for hippocampal ablation [74] can cause areas of signal loss larger than the 2 cm diameter of the hippocampus (Figure 2.3). The size and location of signal loss is highly dependent on the slice and probe orientation within the magnetic field, making universal signal recovery challenging. This

signal loss must be corrected to allow monitoring of thermal therapies near these devices.

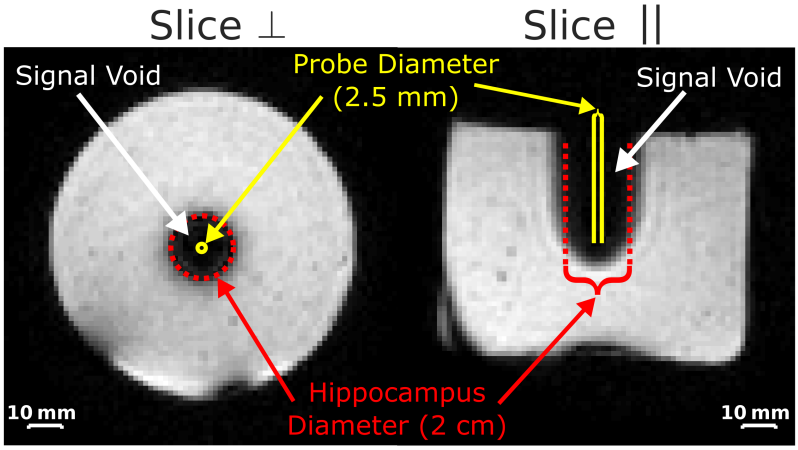

Figure 2.3: Metal ablation probes cause signal loss in gradient echo images. The representative phantom images at the single long TE used for conventional MR thermometry show a signal void exceeding the diameter of the hippocampus near the nitinol ablation probe. The shape of this signal loss depends on slice and probe orientation within the magnetic field.

In-plane distortions caused by metallic objects can be mitigated by a high read-out bandwidth but compensating for through-plane distortions, a main source of signal loss, is still an issue. Methods exist to correct for through-plane dephasing present in gradient echo sequences, which could enable PRFS thermometry near metal [76, 77]. However, these have not been adapted for thermometry in a manner that is directly translatable to clinic. Z-shimming is a technique previously employed in functional MRI studies to account for through-plane signal loss near air sinuses [78, 79]. This technique partially refocuses the image in the slice direction to selectively refocus areas of the image that were off-resonant, effectively recovering the lost signal . Z-shimming has been applied in the interventional setting by to passively track paramagnetic markers attached to catheters for improved localization [76]. This method was extended by Campbell-Washburn et. al to simultaneously acquire a marker image overlaid on an anatomical image in real time [77]. Recently, we adapted this method for thermometry purposes with a dual-echo approach [80], which acquires images both near the probe and far from the probe for whole-image thermometry. While the dual-echo approach recovers temperature precision near the probe without com-

promising precision elsewhere, its use is limited by the need to perform orientation-specific manual calibration (Figure 2.4A and B), where the Z-shim value depends on the orientation of the ablation probe and imaging slice within the magnetic field. Additionally, the dual-echo method is constrained to one Z-shimmed echo, limiting its ability to fully refocus the range of through-plane off-resonance gradients caused by the probe in one acquisition. An example of this limitation can be seen in Figure 2.4C where the spin echo image shows a smaller signal void than the combined z-shim image. There is a need for a thermometry method that is orientation-independent and fully recovers signal near the probe.

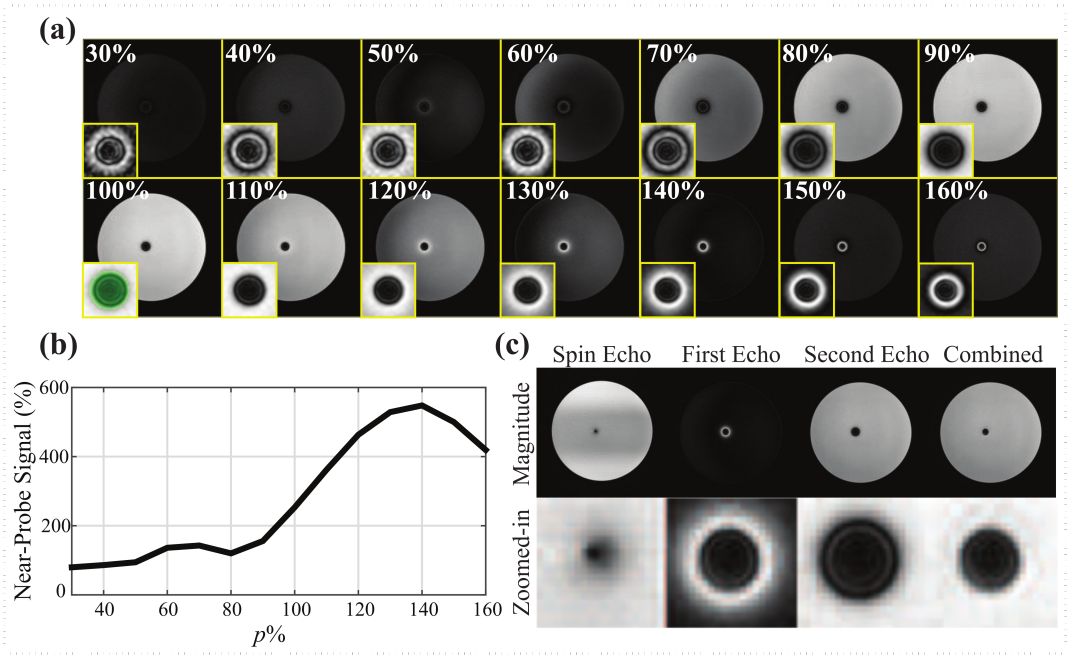

Figure 2.4: Dual-echo z-shimming calibration for one probe and slice orientation from Ref. [80]. (a) Signal recovery near the probe (middle) depends on applied z-shim strength. (b) Optimal recovery is at 140% of the full refocusing gradient. (c) Some near-probe signal is still un-recovered when compared to true probe diameter (spin echo).

2.1.7 Summary of MRI temperature mapping

MRI temperature mapping provides excellent sensitivity and accuracy in many treatment scenarios. Inherently non-invasive and spatially resolved, MR thermometry offers a practical alternative to invasive, single-point thermocouple measurements. Multiple MRI parameters

such as T_1, T_2, ADC, and PRFS are sensitive to temperature. PRFS has been shown the be a reliable measure in aqueous tissues due to its linearity and can straightforward acquisiton with gradient echo images. Errors in MR thermometry do arise in adipose tissue due to fat's smaller frequenyc shift with temperature. Many methods have been proposed to make MRI thermometry robust to these errors including spectroscopic and fat-referenced methods, direct measure of the underlying fatty tissue with relaxation-based measures, and dual-contrast sequences. However, challenges remain to make these methods robust to motion and off-resonance, and suitable for use with few echoes. PRFS thermometry near metal ablators is currently limited due to large dephasing and signal loss that occurs near the probes. Current solutions focus on using other sources of temperature measurement, such as T_1 relaxation, or Z-shimming, which requires tuning, to mitigate this problem. T_1-based solutions are inherently slower than gradient echo methods and require calibration of the T_1 change with temperature before use. The challenge of sequence calibration must be addressed before MR thermometry can be used in treatment scenarios near metal probes, and is an area that this dissertation addresses.

2.2 MR-guided Ablation Modalities

There are a variety of devices that have been employed to ablate lesions within the body [81]. The concept of killing tumor cells through ablation has been around since the 1850s when iced saline was was directly injected into breast and uterine tumors to reduce inflammation and was found to destory cells and slow disease progression [82]. It wasn't until the mid 1900s that cryotherapy was used as a surgical technique with dedicated applicator for ablation [83]. Around this time, the development of electrosurgical devices to cauterize and resect malignancies were invented [84] and the idea of ablation with heat was born. This area has evolved into radiofrequency and microwave ablation applied percutaneously. Focused ultrasound ablation was also being developed with the first ever successful tissue lesion in 1942 and dedicated focal system in 1955[85]. Laser ablation became feasible in the

1970s, first for eye and skin applications but was hindered by a lack of understanding of laser-tissue interactions, a topic of research since the 1990s [86]. It wasn't until the early 2000s that laser ablation began to be applied for oncologic applications [87, 88]. The most commonly used modality of ablation in the clinic today is radiofrequency ablation along with microwave and cryoablation, depending on the application [89]. With the advent of image guidance and MRI, using these technologies in a minimally invasive manner, as opposed to an aid during open surgery, has become more widespread [90]. For many of these therapies, the size of the target relative to the achievable ablation size is a limiting factor, as covering the tumor and its margins in their entirety can be challenging with a single applicator. Additionally, heat sink effects near large blood vessels and fine control of the extent of tissue damage can have a large influence on treatment success. Spatially-resolved temperature maps are critical in managing these scenarios, and MR thermometry is increasingly filling this need [91]. Non-thermal mechanisms such as ethanol injection and elecroporation can also be used to induce targeted cell death. However, these modalities do not use a thermal mechanism and are thus not a focus of this dissertation. This dissertation deals primarily with enabling MR thermometry guidance for ablative treatments, specifically radiofrequency and focused ultrasound. In light of this, the next two sections will focus on these two forms of thermal therapy.

2.2.1 Radiofrequency Ablation

Radiofrequency ablation (RFA) is one of the most ubiquitous ablation modalities used in the clinic due to its accessibility, low cost, and efficacy for a variety of applications [92]. Particularly in the management of liver disease, RFA has been shown to be effective at treating early stage tumors measuring 3 cm or less in diameter [93]. To perform an ablation, alternating current with a frequency around 500 kHz is channeled into an applicator inserted into the body. A grounding pad placed on the other side of the body is used to close the circuit, creating an electrical field within the body. This field contains enough energy to

cause frictional heating between molecules. Due to the antenna geometry of the applicator, the current density is most concentrated near the ablation device, inducing local heating and tissue coagulative necrosis within a small area around the applicator, depending on geometry [94]. The most common applicator is a monopolar antenna which generates one lesion. Multiple electrodes can be placed to increase the volume coverage or shape the treatment area to avoid tissues of interest and combat heat sink effects from blood vessels. Further probe development has resulted in expandable electrode arrays, with multiple tines extending from the tip of the device to increase surface contact with the tissue [92]. Many systems also incorporate a thermocouple along the shaft of the ablator to provide single-point temperature feedback.

RFA is a well-established technique for ablation. However integration with MRI is not without its challenges. The frequency of electromagnetic energy used for RFA is near that used for MRI, leading to potential image artifacts when RF energy is delivered during imaging. This can be mitigated with generator noise reduction techniques, triggering, and by limiting the generator output power [95]. RFA devices are commonly made from metallic materials that are incompatible with MRI. Special MR-compatible electrodes must be purchased that are made from non-magnetic materials such as nitinol, but signal loss can still occur around the probe due to large susceptibility mismatch between the ablator and tissue. This signal loss occurs directly in the area of maximal heating and can cause problems with MR thermomtery monitoring. As discussed in Section 2.1.6, the correction of these artifacts for thermometry is challenging and an active area of research that this dissertation addresses (Chapter 4).

2.2.2 Focused Ultrasound

Focused ultrasound (FUS) is a promising non-invasive surgical modality with the ability to thermally and mechanically affect target tissue while sparing intervening tissues. It has seen development for many applications including tumor ablation and hyperthermia [96],

immunotherapy [97, 98], neuromodulation [99, 100], blood brain barrier opening [101], drug delivery [102], blood vessel clearing [103], and mechanical tissue digestion [104] (Figure 2.5). Though FUS was first explored for non-invasive surgery as far back as the 1950s [85], it was hindered by a lack of imaging guidance, which has been overcome with the development of magnetic resonance imaging (MRI) and its integration with FUS. MRI provides excellent soft tissue contrast and is sensitive to changes in tissue resulting from FUS treatment. Commercial clinical MR-guided FUS (MRgFUS) systems use MRI for treatment planning, treatment monitoring via real-time temperature imaging [12], and treatment assessment.

FUS relies on the propagation of sound waves where, analogous to sunlight through a magnifying glass, the waves are focused to a point. This can be achieved using a spherically focused transducer that generates sound waves through the vibration of piezoelectrics. Phased arrays can also be used to control parts of the transducer individually in order to steer the beam and focus at points away from the geometric focus of the transducer. The waves generated by the transducer are often at a lower frequency than those used by medical ultrasound but at much higher energy (up to 10,000 W/cm^2)[106]. The acoustic focus of the ultrasound beam can induce heating and mechanical disruption, with multiple potential bioeffects as a result. Due to their focal nature, these effects are seen primarily at the focus with little to no effect in intervening tissues. Similar to the ablation modalities discussed above, FUS can be used to induce tissue necrosis via heating. However, no insertion of a probe into the body is required, making FUS a good candidate for non-invasive surgery. The transducer can be coupled to the skin or inserted into the body orfices for closer access to a target. In order to be compatible with MRI, FUS transducers are made from non-magnetic materials. While there may be some susceptibility mismatch of materials, because the transducer is outside the body this does not cause artifacts at the area of heating.

In spite of its promise, the availability of preclinical MRgFUS systems for research remains limited due to the high cost and often application-specific nature of commercial systems. Construction of custom MRgFUS systems is labor-intensive, requires trial and error,

Figure 2.5: Overview of FUS development and application areas. Figure from the Focused Ultrasound Foundation [105].

and systems must be validated for their application. For example, in the case of thermal therapy the *in vivo* response has been shown to be dose dependent [107, 5], particularly in the case of hyperthermia where avoiding the cell death threshold is key. Therapy requires a precise thermal dosage, robust, fine control over the sonication, and accurate thermal monitoring. Developing and debugging a system with these capabilities takes time and expertise which could be a roadblock to researchers who aim to develop new MRgFUS techniques and

applications. Work addressing this barrier is presented in Chapter 5 of this dissertation.

2.2.3 Summary of Modalities

Minimally-invasive ablation can be an effective alternative to traditional surgical resection. Treatment can be performed percutaneously under image guidance to target the diseased tissue while minimizing damage to normal healthy tissue. The field is growing in both types of ablation and disease targets. Ablation of liver and kidney cancers has been well explored [108, 109] as well as more recent applications in the spine [110] and brain [2]. MRgFUS has the potential to perform incision-less ablations but more research is needed to explore the areas of application. The use of these ablation modalities in clinic can reduce costs and improve patient outcomes, but would benefit from robust imaging guidance and temperature feedback during treatment.

Chapter 3

MULTI-ECHO FAT-SUPPRESSED MR THERMOMETRY USING ITERATIVE SEPARATION OF BASELINE WATER AND FAT IMAGES

3.1 Introduction

Magnetic resonance (MR) temperature mapping enables real-time guidance of minimally-invasive and non-invasive thermal therapies. As previously discussed, the proton resonant frequency - shift (PRFS) with temperature is the most widely used mechanism due to its simplicity and sensitivity. However, the presence of fat in heated voxels can cause erroneous PRF measures since fat experiences a much smaller PRFS with temperature than water [20]. This is particularly a problem when monitoring therapies such as focused ultrasound ablation of breast tumors, which are highly embedded in adipose tissue [21]. This chapter describes a multi-echo water/fat separated temperature mapping method that is robust to motion, estimates dynamic off-resonance frequency changes from both water and fat signals, and can estimate temperature from a single echo during heating. It incorporates state-of-the-art, iterative water/fat separation without requiring computationally-intensive separations to be computed during heating. The method works by collecting a baseline library of pre-treatment images over a range of motion states, performing water/fat separation on those images, and then incorporating the separated baseline water and fat images into a heating image model. That model is fit to heating images to estimate fat-suppressed, dynamic off-resonance- and motion-corrected temperature maps, without performing explicit water/fat separation on the heating images. Simulations were performed to evaluate the method across a range of temperatures, fat fractions, motion, and off-resonance field shift amplitudes and spatial orders. Experiments were performed in tissue phantoms with heating to verify temperature accuracy and in healthy human subjects without heating to verify temperature precision in the presence of dynamic off-resonance field changes and motion.

3.2 Theory

3.2.1 Multi-Echo Heating Image Model

The proposed algorithm is based on a multi-echo signal model for images with heating that combines the hybrid multibaseline and referenceless image model [15] with a water/fat separated multi-echo image model [111]. The hybrid model has previously been shown to be robust to tissue motion and spatiotemporally varying off-resonance caused by scanner off-resonance shift, cardiac motion, and respiration. For a single echo image with heating, the model comprises a localized heating-induced frequency or phase shift applied to a weighted combination of pre-heating baseline images, and is given by:

$$y_j = \left[\sum_{l=1}^{N_l} b_{j,l} x_l\right] e^{\imath(\{\boldsymbol{A}\boldsymbol{c}\}_j + u\Delta T_j)TE}, \tag{3.1}$$

where y_j is the complex-valued MR signal in image voxel j, N_l is the number of complex-valued baseline library images $\boldsymbol{b}_l$, the x_l are the baseline weights, $\imath = \sqrt{-1}$, $\boldsymbol{A}$ is a polynomial basis function matrix multiplied by the coefficient vector $\boldsymbol{c}$, whose product models dynamic off-resonance frequency changes that are not related to heating, $u = \gamma\alpha B_0$ where γ is the gyromagnetic ratio, $\alpha = -0.01$ ppm/°C, B_0 is the scanner field strength in Tesla, ΔT_j is the temperature shift in degrees Celsius due to heating, and TE is the echo time in seconds.

To model multi-echo signals with water and fat components, the above image model is combined with the following water/fat separated signal model for voxel j at echo time TE:

$$y_j = \left(W_j + F_j \sum_{m=1}^{M} \alpha_m e^{\imath\omega_m TE}\right) e^{(\imath\Delta\omega_j - R^*_{2,j})TE}, \tag{3.2}$$

where W_j and F_j are the baseline water and fat images at voxel j, M is the number of fat spectral peaks, the α_m are the fat peak relative amplitudes, the ω_m are the offsets between the fat and water peak frequencies, TE is the echo time, $R^*_{2,j}$ is the effective transverse relaxation rate, and $\Delta\omega_j$ is the baseline off-resonance field map. This signal equation applies

to baseline images acquired prior to heating and is combined with the hybrid model in Equation 3.1 to obtain a multi-echo water/fat separated image model during heating.

Combining Eqs. 3.1 and 3.2, we obtain a water/fat separated multi-echo hybrid thermometry signal model at voxel j and echo time TE:

$$y_j = \left(\left[\sum_{l=1}^{N_l} W_{j,l} x_l \right] e^{\imath u \Delta T_j} + \left[\sum_{l=1}^{N_l} F_{j,l} x_l \right] \sum_{m=1}^{M} \alpha_m e^{\imath \omega_m TE} \right) e^{(\imath(\Delta\omega_j + \{\boldsymbol{Ac}\}_j) - R^*_{2,j})TE}, \qquad (3.3)$$

where $W_{j,l}$ and $F_{j,l}$ are the baseline water and fat images. The field off-resonance map $\Delta\omega$, the transverse relaxation (R_2^*), and the dynamic polynomial off-resonance frequency shift $\boldsymbol{Ac}$ apply to both water and fat components, while the PRFS only applies to the water component (ΔT_j). During heating, this model is fit jointly to a set of multi-echo images using the algorithm described next. Note that similarly to Ref. [15], this work uses a referenceless heating image model to account for dynamic changes in off-resonance, but models it as a frequency shift rather than a phase shift to generalize to multiple echoes.

3.2.2 Model-Based Temperature Reconstruction Algorithm

The model-based water/fat separated temperature reconstruction algorithm is illustrated in Figure 4.2 and fits the multi-echo signal model of Equation 3.3 as follows.

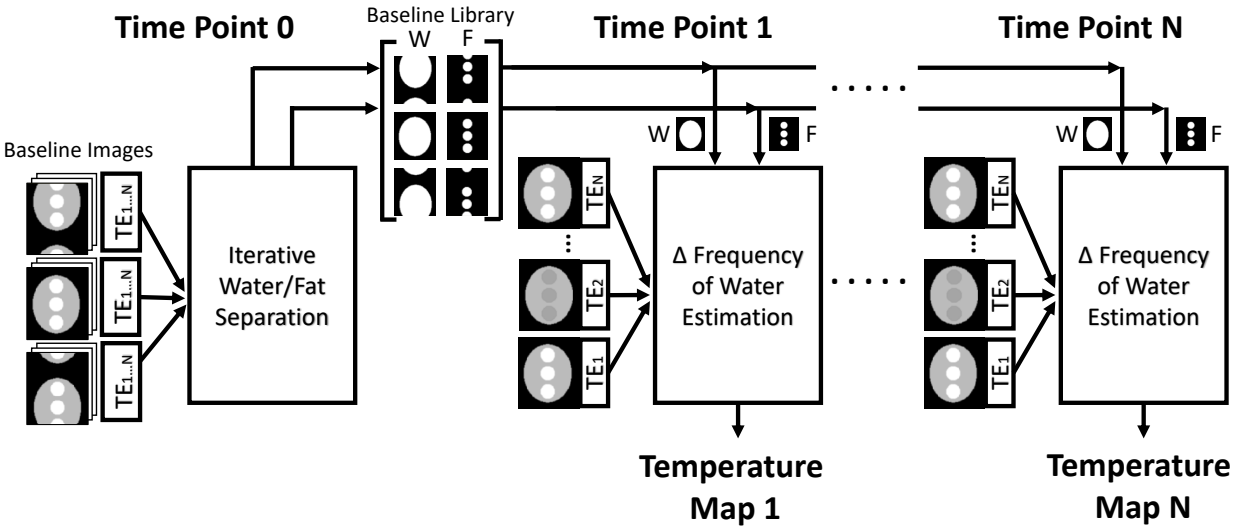

Figure 3.1: Model-based water/fat separated thermometry algorithm flow chart. The multi-echo baseline images are processed to obtain a library of water/fat separated images, which are subsequently used to estimate temperature during dynamic imaging. In this way, an accurate fat-suppressed temperature map can be reconstructed for each heating time point, without repeatedly performing computationally expensive water/fat separation.

First, the multi-echo baseline library images are separated into their water and fat signal components, generating a library of water and fat images for each motion state. Since the images are measured prior to heating, water/fat separation can be performed using state-of-the-art, iterative water/fat separation methods. These separations are robust to field inhomogeneities and yield off-resonance and R_2^* maps [30, 31, 32], but they are applied only to the baseline images due to their long compute times. Given the separated baseline water and fat images, Equation 3.3 is jointly fit to the multi-echo images during heating by minimizing the cost function

$$\Psi(\boldsymbol{\Delta T}, \boldsymbol{c}, \boldsymbol{x}) = \sum_{j=1}^{N_s} \sum_{k=1}^{N_e} \left| \tilde{y}_{j,k} - y_j(\Delta T_j, \boldsymbol{c}, \boldsymbol{x}; TE_k) \right|^2 + \lambda \sum_{n=1}^{N_s} |\Delta T_n| \,. \tag{3.4}$$

The first term of Equation 3.4 is proportional to the negative log-likelihood of the data and measures the errors between the acquired complex-valued data $\tilde{y}_{j,k}$ at voxel j and echo k, and the model described by Equation 3.3. N_s and N_e are the number of voxels and number of echoes, respectively. The second term is the ℓ_1 norm of the temperature change map

ΔT_n, and λ is a regularization parameter that is tuned to control the map's sparsity. This sparsity regularization reflects the expectation that for localized therapies such as focused ultrasound ablation, heating will occur in a minority of image voxels. An iterative algorithm extended from Ref. [15] is used to minimize this cost function, which alternates between updating $\boldsymbol{\Delta T}$, $\boldsymbol{c}$, and $\boldsymbol{x}$, minimizing one while the other two are held constant. $\boldsymbol{\Delta T}$ and $\boldsymbol{x}$ are initialized to zero and $\boldsymbol{\Delta T}$ is constrained to be non-negative since temperature is expected to rise during heating. To avoid local minima in the presence of large off-resonance changes, the zeroth-order entry in $\boldsymbol{c}$ is initialized with 0 and $\pm\pi/TE_{mean}$ radians/second in the first iteration. The rest of the fit proceeds using the initial value of $\boldsymbol{c}$ that resulted in the lowest cost. At each iteration, $\boldsymbol{\Delta T}$ and $\boldsymbol{c}$ are updated using gradient descent and $\boldsymbol{x}$ is updated by solving a quadratic program, subject to a non-negativity constraint and the requirement that its entries sum to one. Once the algorithm converges, it is repeated with $\lambda = 0$ and $\boldsymbol{\Delta T}$ is updated only in voxels with significant heat as determined by thresholding, to eliminate downward temperature bias due to the ℓ_1 regularization. Note that unlike previous water/fat separated thermometry methods, the off-resonance frequency shift coefficients $\boldsymbol{c}$ are determined from both the fat and water signals. In this way, the fat signal serves as a heating-insensitive off-resonance frequency shift reference same as previous methods but does not require extrapolation of the shifts to water-only voxels. The baseline weights $\boldsymbol{x}$ are also determined from both signals. Note that no explicit water/fat separation of the heating images is used in this temperature reconstruction.

3.3 Methods

The model-based algorithm was evaluated in simulations, a porcine focused ultrasound heating experiment, and *in vivo* breast and liver imaging experiments in free-breathing volunteers without heating. All reconstructions and analyses were performed in MATLAB (Mathworks Inc., Natick, Massachusetts, USA) on a 3.4 GHz 8 core desktop computer running Ubuntu 16.04 with 32 GB RAM. Baseline multi-echo images were separated into their water

and fat components using the Mixed-Magnitude method [111] initialized with the Graph Cut method [30] from the ISMRM Fat-Water Toolbox [32]. The first echo image of acquired data was discarded for the water/fat separation to avoid a known first echo signal instability on our scanner that results in inaccurate water/fat separations. The data was normalized by the median value of the heating images and the number of echoes prior to temperature map reconstruction. The model-based method was compared to the fat-referenced method described by Hofstetter et al. [44]. Using the same water/fat separated baselines as the model-based method, the fat-referenced method accounted for off-resonance using a least squares fit of the same order as the model-based method, weighted by the fat image at each time point and extrapolated across all voxels. All model-based temperature maps were computed with a significant heat threshold of 0.5 °C, sparsity regularization parameter of $\lambda = 10^{-4}$, and 5 iterations for each update of the temperature change ($\boldsymbol{\Delta T}$) and off-resonance shift coefficients ($\boldsymbol{c}$). The algorithm stopped when the relative change in the cost function was less than 10^{-4} between consecutive iterations with a maximum limit of 10 iterations. Algorithm code is available at https://github.com/poormanme/waterFatSeparated_MRThermometry

3.3.1 Simulations

Simulations were performed to evaluate reconstructed temperature accuracy versus peak temperature, off-resonance field shift amplitude and spatial order, fat fraction, motion, and the number of heating echoes used for reconstruction. A numerical phantom was defined at 1.5 Tesla according to the six spectral peak fat model [112] and Equation 3.2 on a 128×128 voxel grid with a Gaussian hotspot with $\sigma^2 = 10$ voxels. Multi-echo images were generated at five echo times (TE = [12.7, 13.8, 15, 16.2, 17.3] ms) with an additional zeroth-order off-resonance field shift of 5 Hz in the heating images (Figure 3.2A). Complex-valued Gaussian noise was added to one copy of the dataset to obtain an SNR of 40.

In the first simulation, the hotspot was applied over a range of peak temperature changes (0 to 40 Δ°C, step size of 4°C) in the center of the phantom, placed completely within the

mixed voxels (50% fat fraction). Root-mean-square error (RMSE) and maximum temperature errors were evaluated for both thermometry methods with and without noise. In the second simulation, the zeroth-order off-resonance field shift was varied between 0 and 100 Hz in steps of 10 Hz with the peak temperature change held fixed at 20°C. Then, the polynomial order was increased from zeroth to sixth while maintaining a spatial mean amplitude of 5 Hz. In the third simulation, the phantom's fat fraction was varied between 0 and 100% in steps of 10%, and the peak temperature change was held fixed at Δ 20°C. In the fourth simulation, the 50% fat fraction phantom was translated in one dimension to simulate bulk phantom motion, producing a baseline library of images at 65 different locations (Figure 3.5A). That baseline library was then uniformly decimated by factors of two, three, and four to generate four libraries with different motion resolutions. Two heating image sets were generated at every location by applying a peak temperature change of 20°C either fixed in place or tracked with the motion to each image. In the fifth simulation, one, three, and five echoes were used for model-based reconstruction, with a peak temperature change of 0 and 40°C. The one-echo reconstruction used a TE of 17.3 ms, and the three-echo reconstruction used TEs of 15, 16.2, and 17.3 ms.

3.3.2 *Ex vivo* porcine sonication

An *ex vivo* porcine muscle sample and bacon slab with fat layers was placed in a dedicated breast MR-guided high intensity focused ultrasound (MRgFUS) system [21] (Philips Healthcare, Vantaa, Finland). The system's breast cup was filled with doped water (manganese (II) chloride tetrahydrate 160 mg/L) for acoustic coupling (Figure 3.7A) and a fiber optic thermal probe (Luxtron m3300, LumaSense, Santa Clara, California, USA) was sandwiched between the muscle and bacon fat layer 4 cm from either edge of the phantom for concurrent monitoring. The probe tip was localized with test sonications and T_1-weighted images (1.5 Tesla Philips Achieva, Best, Netherlands) prior to heating at the probe tip using a 4.5×4.5×6 mm^3 focal cell sonication at the sample's water/fat interface. The temperature imaging slice

was positioned coronally at the water/fat interface to yield images with a mixture of water and fat (Figure 3.7A). Five multi-echo image sets were acquired prior to sonication (TR = 25 ms, TE = 1.3 to 10.6 ms, 6 echoes, voxel size = 2.15×2.15×4 mm^3, 2 averages, BW = 70kHz) and averaged to form a single, high SNR, baseline image that was used for both the fat-referenced and model-based methods. Averaging improved temperature SNR of both methods by reducing baseline phase noise. The focus was heated from room temperature (26°C) at 30 acoustic Watts for 60 seconds and allowed to cool while imaging with the same sequence (6.4 seconds per time point). The baseline images were separated into their water and fat components, and temperature maps were computed with a first-order off-resonance shift. The focal temperature for each temperature reconstruction was compared to the fiber optic probe reading to assess accuracy. The model-based reconstructions were repeated with one to five echoes, where in each case the last N echoes was used for reconstruction, i.e., the $N = 5$-echo case used echoes 2 to 6 while the $N = 3$-echo case used echoes 4 to 6.

3.3.3 *In vivo* breast

Informed consent was obtained from a healthy female volunteer in accordance with the ethics committee of the University Medical Center Utrecht. The volunteer was scanned on the breast MRgFUS system with no applied heating during free-breathing (Figures 3.9A and 3.10A). Multi-echo images were acquired at two slice orientations for 5 minutes (TR = 25 ms, TE = 1.2 to 10.6 ms, 6 echoes, voxel size = 2.15×2.15×6 mm^3, BW = 70kHz). The first five time points were discarded due to irregular breathing, the next five time points were averaged to form a high-SNR baseline image, and water/fat separation was applied to the baseline. Temperature maps were reconstructed from the remaining time points using second- and first-order fits for off-resonance in the sagittal and coronal orientations, respectively. To evaluate temperature precision in the absence of heating, the model-based algorithm was modified to first solve for the off-resonance shift while the temperature estimate was fixed at zero, then hold the polynomial fit fixed while the algorithm solved for a temperature map

with no sparsity regularization ($\lambda = 0$) and no non-negativity constraint. In this way, the final temperature map contained all residual errors after fitting the polynomial and baseline images to the data.

3.3.4 *In vivo* Liver

Informed consent was obtained from a healthy female volunteer in accordance with the Vanderbilt University Institutional Review Board policies. To experimentally characterize the method's robustness to motion, a 16 channel torso coil was used to image the subject's liver at 3 Tesla (Philips Achieva, Philips Healthcare, Best, Netherlands) for 3.4 minutes in three orientations during free breathing (TR = 25 ms, TE = 0.9 to 11.7 ms, 10 echoes, 3×3×4 mm^3 voxel size, bandwidth = 176 kHz). The first five time points were discarded to avoid irregular breathing, the subsequent 10 images formed the baseline library, and water/fat separation was applied to each baseline. The model-based algorithm was modified to evaluate precision in the absence of heating as described above. Temperature maps were reconstructed from the remaining images with a sixth order polynomial off-resonance frequency shift. For the fat-referenced method, the third baseline was used as the baseline reference, which captured the liver at the middle of the respiratory cycle.

3.4 Results

3.4.1 Simulations

Figure 3.2b displays representative temperature maps reconstructed by the fat-referenced and model-based methods. Figure 3.2c plots RMSE and maximum temperature errors versus peak temperature for both SNR = ∞ and SNR = 40. The fat-referenced reconstruction maintained an average RMSE of 0.12 °C for SNR = ∞ and 0.13°C for SNR = 40, and error increased with peak heat. The model-based reconstruction errors are flat across peak temperature, with an average RMSE of 0.002°C for SNR = ∞ and 0.08°C for SNR = 40.

The baseline water/fat separation took 24 s or 37 s to compute and the model-based fitting took 1.1 s and 1.4 s per heating timepoint, respectively, for SNR = ∞ and SNR = 40. In the 0°C peak heat case, the model-based method's sparsity regularization suppressed the noise, resulting in RMS errors of 0°C.

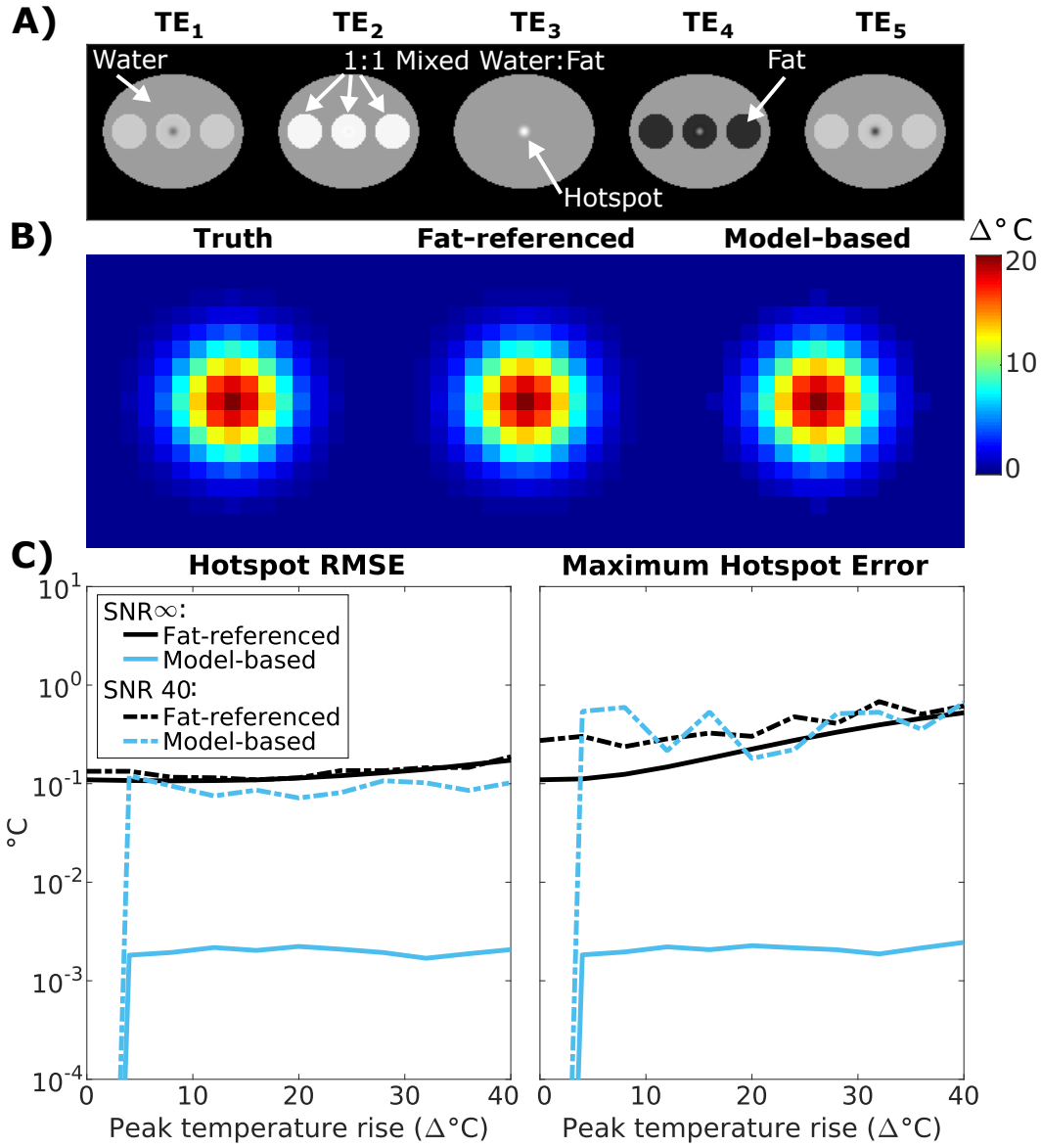

Figure 3.2: Simulated temperature error versus peak temperature rise. A) Magnitude images of the simulated water-fat phantom, which were generated at multiple echo times and peak heating levels. B) Representative temperature maps (zoomed to hotspot) reconstructed with each algorithm, at 20 Δ°C peak heat. C) RMS and maximum error in the reconstructed hotspot for each algorithm with SNR = ∞ and SNR = 40.

Figure 3.3A displays temperature maps reconstructed by each method with zeroth-order, 50 Hz off-resonance and third-order, 5 Hz (spatial-average) off-resonance. The fat-referenced maps have errors up to -20°C in voxels with no fat, while the model-based method is accurate regardless of fat distribution. Figure 3.3B shows whole image RMS error for both methods at varied off-resonance shifts and orders. The fat-referenced method's error increased with both amplitude and order, with an average RMSE of 10.9°C over the range of off-resonance shifts tested and both noise levels. The spikes in fat-referenced error occur when the heating and residual shift phase combine to cause phase wrapping. Across off-resonance orders, the fat-referenced method had an average RMSE of 6.0°C for the SNR = ∞ case and 1.2°C for the SNR = 40 case. The model-based maps were unaffected by changes in off-resonance shift strength and order, maintaining an average RMSE of 0.03°C in all cases. Since the fat-referenced method relies solely on fat voxels to estimate a shift, it is unable to extrapolate account for inhomoneous shifts that occur outside the fatty regions and extrapolate them to the water-based voxels. This extrapolation error in the fat-referenced method is compounded by the increasingly erroneous water/fat separation with heating that causes an erroneous off-resonance estimation in the fat-containing voxels, even when the baseline B_0 and R_2^* maps are held constant. The model-based method is able to avoid these errors by using the baseline water and fat images and directly estimating off-resonance from both water and fat.

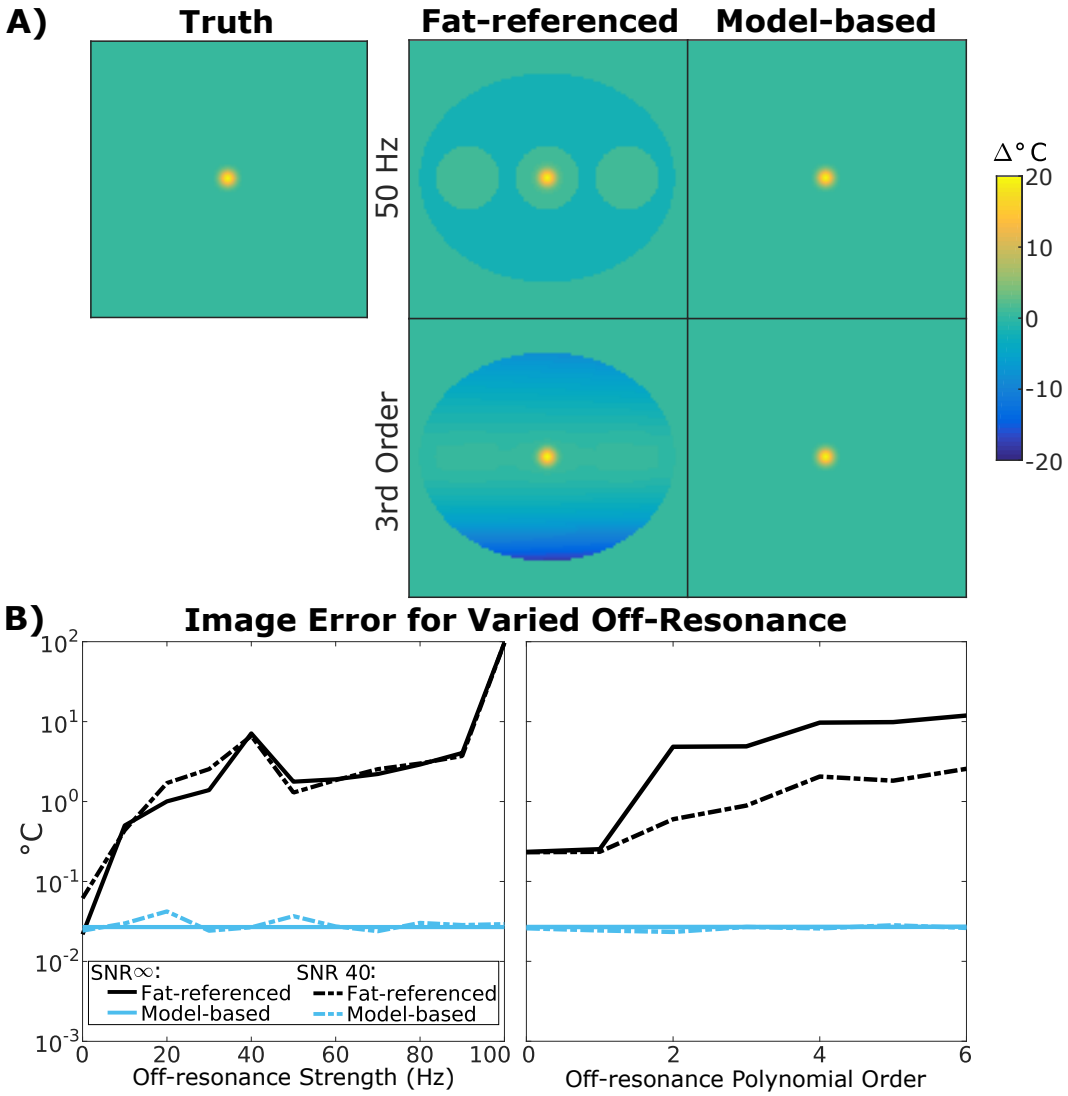

Figure 3.3: Simulated temperature error over a range of off-resonance shift amplitudes and orders. A) Temperature maps reconstructed with a zeroth-order, 50 Hz shift (top) and third-order, 5 Hz shift (bottom). B) (left) Image RMS error vs zeroth-order off-resonance shift strength. (right) Image RMS error at different orders of off-resonance with an average strength of 5 Hz. The fat-referenced error increases with increasing shift strength and order while the model-based error remains flat.

Figure 3.4 plots RMS temperature error in the hotspot as a function of fat fraction for the fat-referenced and model-based methods. For fat contents between 10% and 90%, the fat-referenced maps have an average RMSE of 1.16°C and 0.74°C for the SNR = ∞ and SNR = 40 cases respectively. The method fails at 0% fat with RMS errors of 19.01 °C (SNR = ∞) and 5.80 °(SNR = 40). The model-based maps accurately reconstruct the hotspot with

up to 90% fat with an average RMSE of 0.001°C and 0.12°C for SNR = ∞ and SNR = 40, respectively. Both methods fail in 100% fat with RMS errors greater than 8°C since adipose tissue does not exhibit a PRF shift.

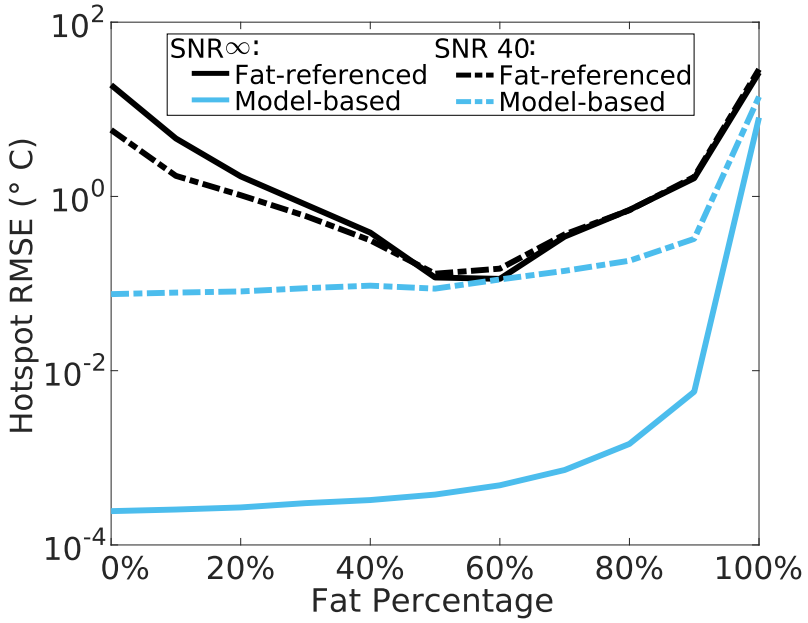

Figure 3.4: Simulated reconstructed temperature error versus fat fraction, for 20°C peak heat.

Figure 3.5B plots whole image temperature errors across phantom locations for each baseline library/image position decimation ratio. When there was a baseline image to match every position, the error was consistently 0.03°C, regardless of motion state. This indicates that the algorithm successfully identified the correct baseline in each case. When the library was uniformly decimated, the error increased up to 0.04°C for the positions that did not have a directly matching baseline. Figure 3.5C shows temperature error maps at the highest decimation factor, at a position where the error was lowest and at a position where the error was highest. In the minimum error image, discrepancies appeared at the edges of the hotspot due to the significant heat threshold applied. In the maximum error image, the phantom was located midway between two baseline locations and interpolation errors occurred at the interface of the pure water and mixed regions. The maximum error remained less than 0.52

°C.

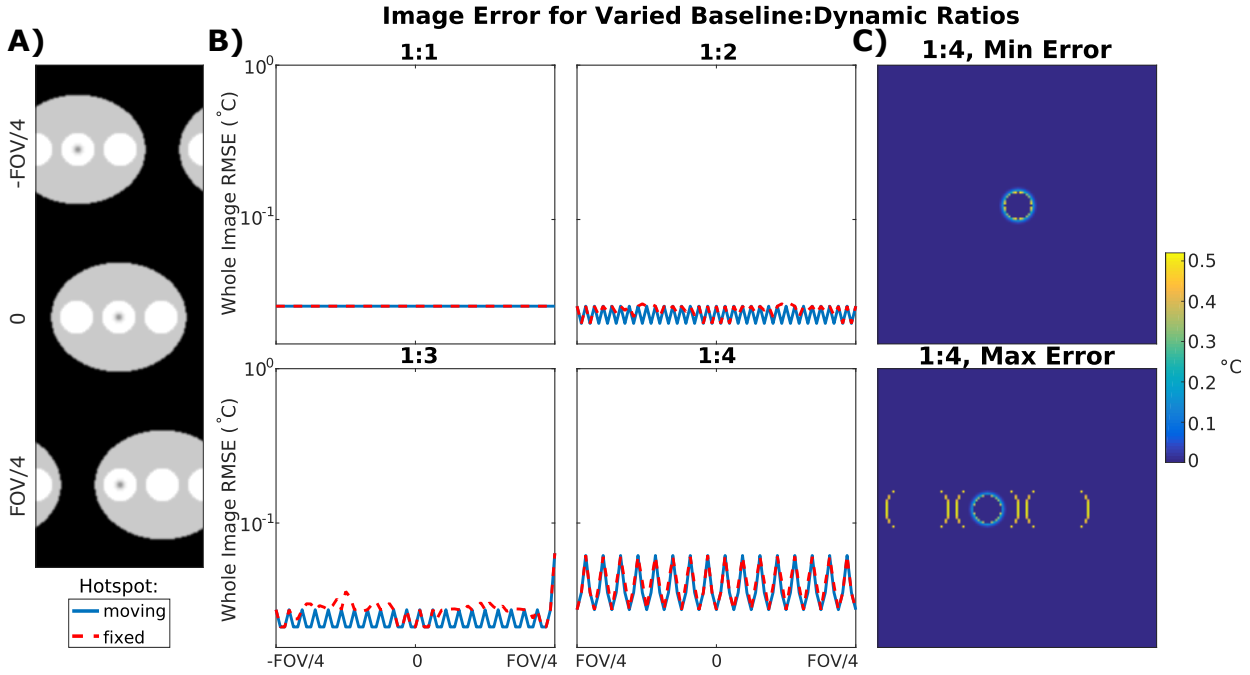

Figure 3.5: Motion simulation results. A) Magnitude images of the simulated phantom, translated across the field of view. B) Whole-image temperature error for each baseline position to heating image position ratio. C) Temperature maps with a 1:4 baseline:heating image ratio at positions where the error is lowest and highest.

Figure 3.6A shows temperature maps reconstructed using 1, 3, and 5 echoes, zoomed to the hotspot. For SNR = ∞, the algorithm achieved an average hotspot RMSE of 0.002°C, 0.001°C, and 0.002°C for the 1, 3, and all-5-echo cases, computed in 0.26 s, 0.59 s, and 1.10 s per temperature map, respectively. For SNR = 40, the average hotspot RMSE was 0.14 °C, 0.11 °C, and 0.08 °C for the 1, 3, and all-5-echo cases, computed in 0.42 s, 0.86 s, and 1.40 s per temperature map, respectively. Errors were unaffected by the peak temperature but increased as the number of echoes decreased in the noisy case due to reduced signal averaging across echoes.

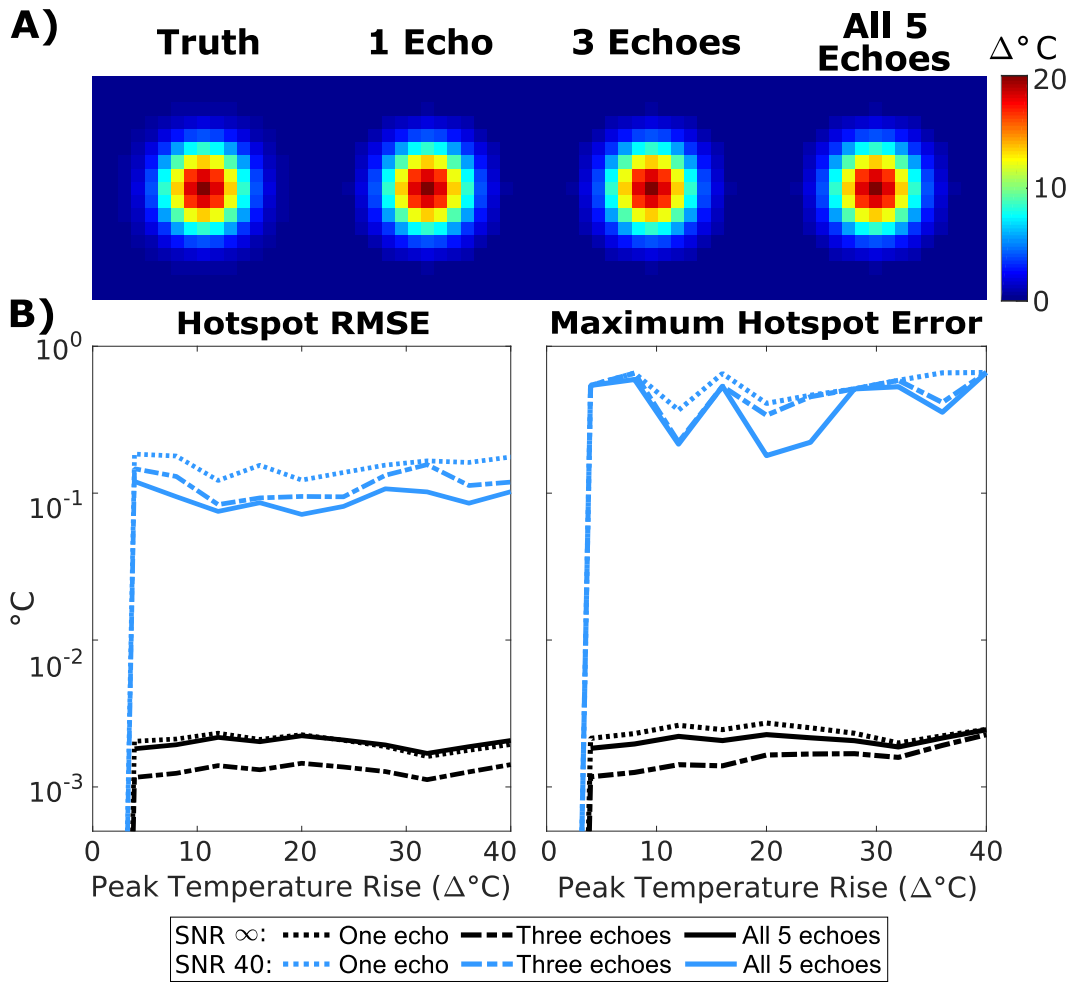

Figure 3.6: Simulated temperature error with a small number of echoes. A) Temperature maps (zoomed to hotspot) reconstructed with the model-based method using different numbers of echoes, at 20°C peak heat. B) RMS and maximum error in the hotspot for each case.

3.4.2 *Ex vivo* porcine sonication

Figure 3.7B shows the fat fraction map computed from baseline images at the slice plane indicated, which had a two minute computation time. The ROI containing the fiber optic probe tip was used to compute the mean hotspot temperature and is indicated by the blue circle (mean fat fraction of 25%). The red and green circles represent ROIs used to examine temperature at points containing more and less fat than the acoustic focus, 61% and 9% respectively. Figure 3.7C shows temperature maps reconstructed from the fat-referenced

and model-based methods immediately after sonication, and the fat-referenced map has lower heat. Temperature curves at each of the ROIs are plotted in Figure 3.7D along with the fiber optic probe measurements. During heating, the fiber optic probe temperature (black line) was influenced by mechanical perturbation and heating of the probe itself. The mean focal temperature reconstructed with the model-based method is accurate with respect to the fiber optic probe during the cooling period with an average RMSE of 0.66°C and had an absolute error of 0.33 °C at peak heat. The fat-referenced method produced an average RMSE of 0.96°C during cooling and an absolute error of 2.21°C at peak heat. Further differences between the two methods can be seen in the ROIs containing 61% fat (red) and 9% fat (green). The model-based algorithm reconstruction took 0.47 s to compute each temperature map.

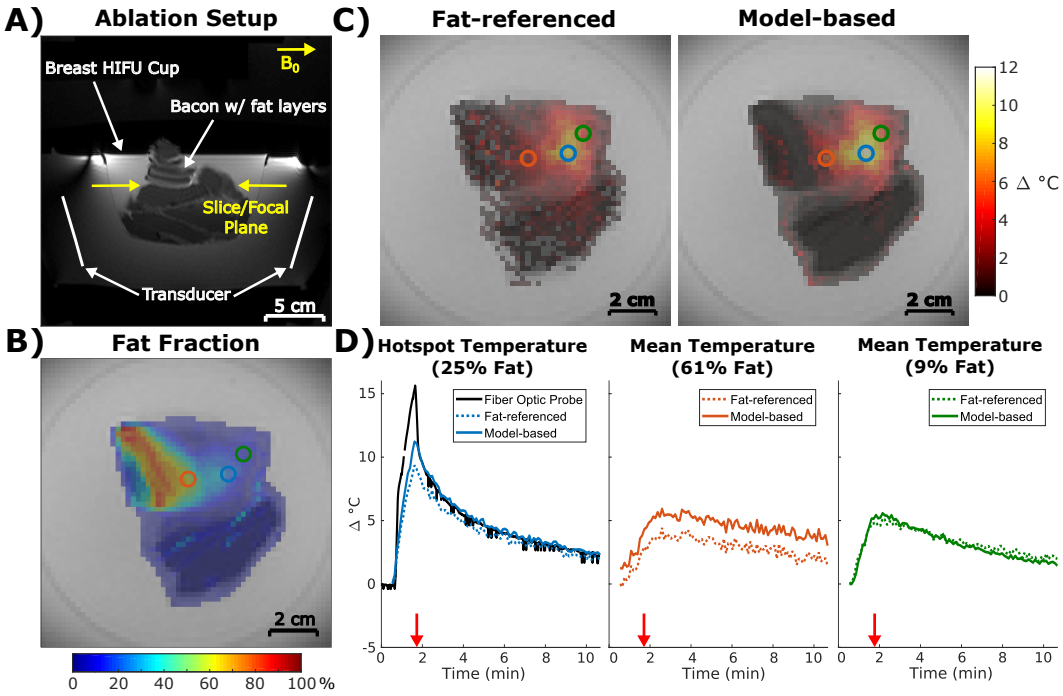

Figure 3.7: Ex vivo pork sonication with simultaneous fiber optic temperature monitoring. A) Survey image showing experimental setup. B) Computed fraction map with circles indicating ROIs used for temperature analysis. C) Reconstructed temperature maps immediately after sonication (red arrows in (D)). Voxels with temperature values equal to 0 were set to transparent. D) Temperature plots for each method at the locations indicated by the corresponding ROIs in (B). Fiber optic probe readings during sonication (0.5 to 1.75 minutes) can be disregarded due to perturbation by the focused ultrasound beam.

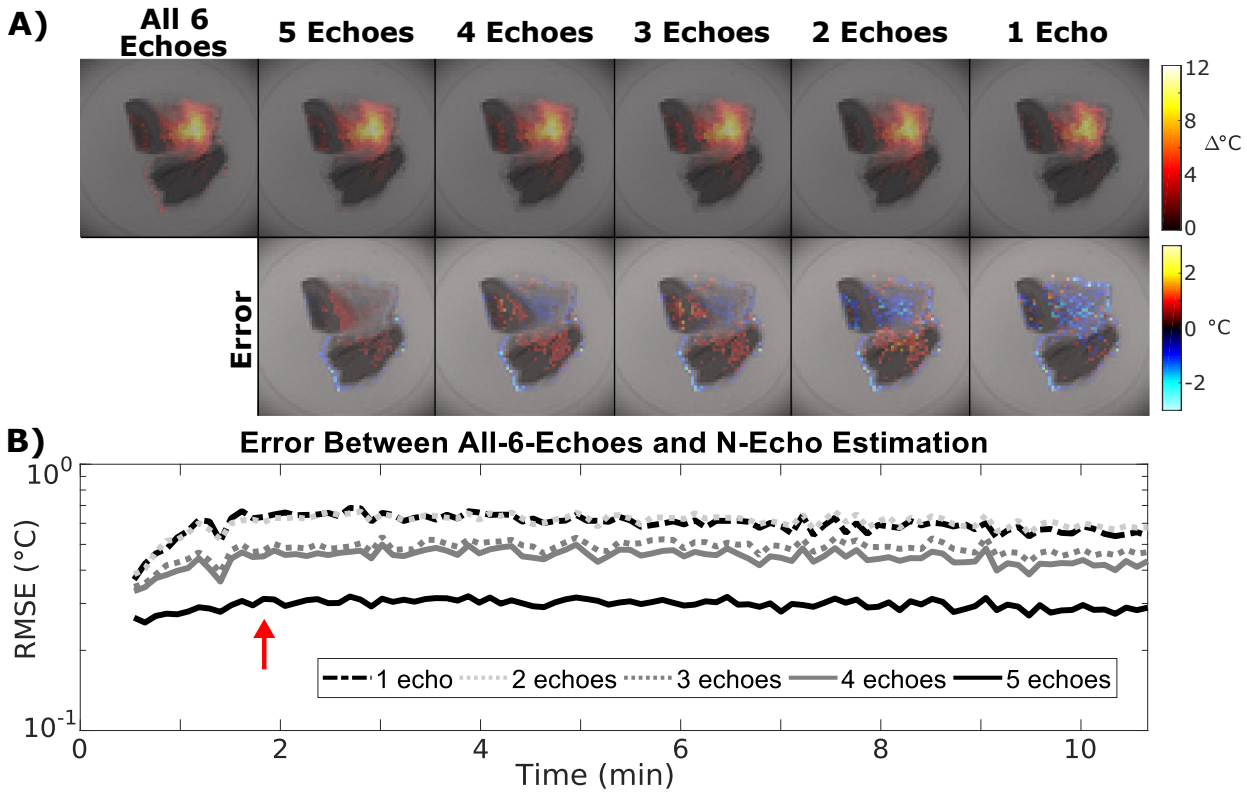

Figure 3.8: Ex vivo pork sonication temperature maps reconstructed with a smaller number of echoes. A) Temperature maps acquired immediately after sonication (red arrow) reconstructed using the model-based method using 1 to all 6 echoes. Voxels with temperature values equal to 0 were set to transparent. B) RMSE between the 6-echo and reduced-echo maps.

Figure 3.8A shows temperature maps reconstructed with one to all six echoes immediately after sonication. Reducing the number of echoes qualitatively increased noise in the temperature maps due to reduced averaging, but did not change the shape or amplitude of the hotspot. The through-time error plot in Figure 3.8B further supports this interpretation, since the error increased as the number of echoes decreased but did not strongly correlate to peak temperature. Computation time per temperature map decreased as the number of echoes decreased, with the one, three, and all-six-echo maps requiring 0.10 s, 0.20 s, and 0.47 s respectively.

3.4.3 *In vivo* breast

Figure 3.9A shows the fat fraction map computed from the multi-echo images taken at the slice plane indicated, which required 60 seconds of computation per slice direction. Through-time average temperature and temperature standard deviation maps of both the fat-referenced and model-based reconstructions are shown in Figure 3.9B. Voxels containing less than 90% fat exhibited an average temperature of -1.8°C in the fat-referenced maps, and -0.12°C in the model-based maps. The mean fat-referenced temperature map contains a large temperature gradient (white arrow) due to inhomogeneous off-resonance shifts cause by lung motion. This gradient is corrected by the referenceless component of the model-based method. Voxels containing greater than 90% fat have temperature errors greater than ±10°C in both methods due to the much smaller PRF shift of fat than that of water. Through-time standard deviations were less than 1°C for both temperature reconstructions, demonstrating precision and stability over the entire time course. The coronal fat-referenced and model-based maps (Figure 3.10) had average temperatures of -1.0°C and 0.07°C respectively, with less than 1°C standard deviation over time. Individual temperature maps for each slice orientation and time point are shown in Figure 3.11, and do not contain appreciable oscillations over time due to respiration or cardiac motion.

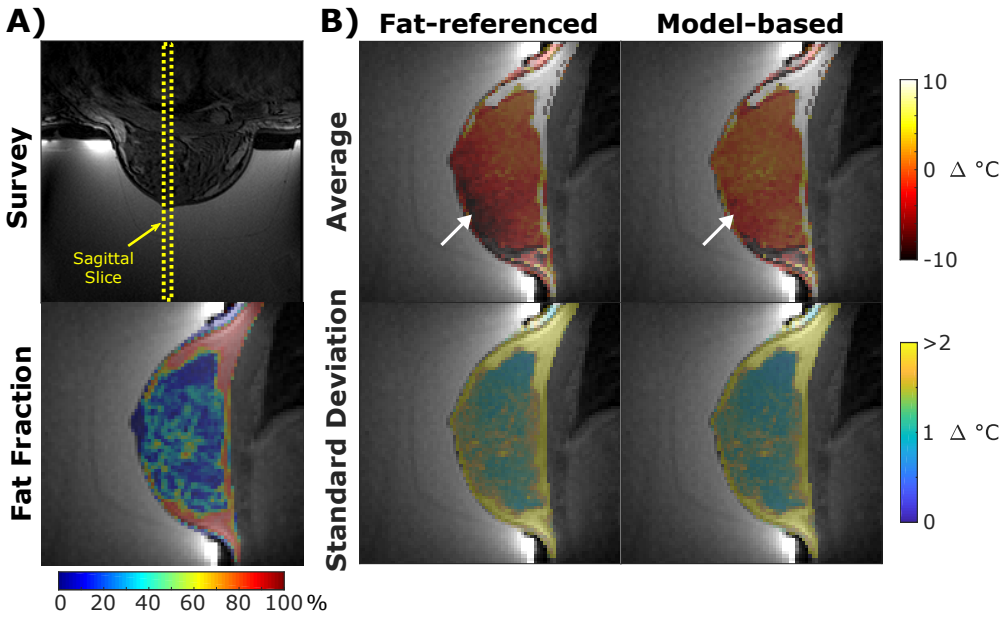

Figure 3.9: In vivo sagittal human breast temperature mapping without heating. A) (top) Survey image and (bottom) fat fraction map of a sagittal slice through breast. B) Through-time mean temperature and standard deviation maps reconstructed with the fat-referenced and model-based methods. The white arrow indicates an area of error due to inhomogenous off-resonance that is corrected by the model-based method. Voxels outside of the breast were set to transparent.

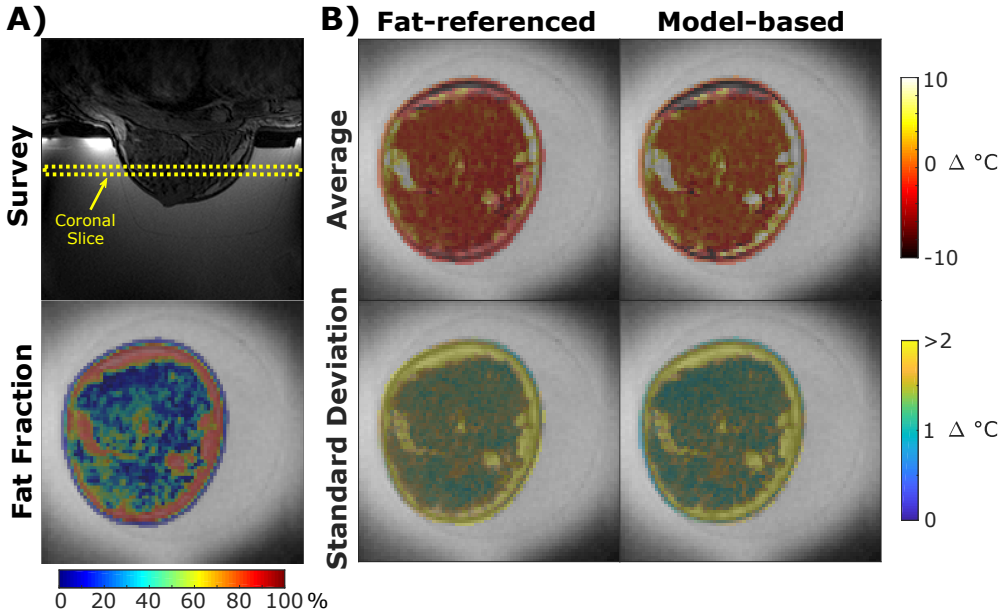

Figure 3.10: In vivo coronal human breast temperature mapping without heating. A) (top) Survey image and (bottom) fat fraction map of a coronal slice through breast. B) Through-time mean temperature and standard deviation maps reconstructed with the fat-referenced and model-based methods.

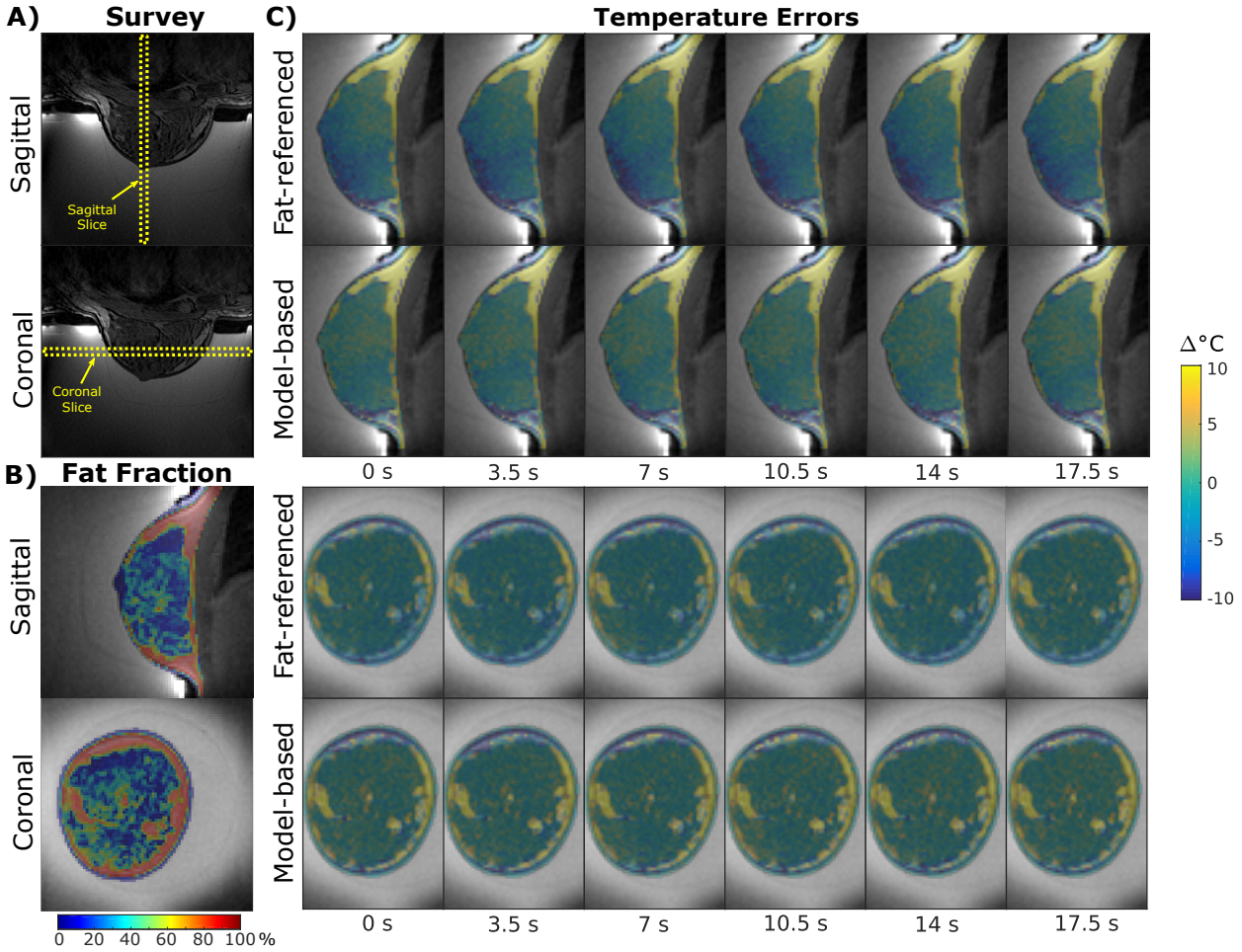

Figure 3.11: Through-time temperature error comparison in the breast at both orientations. A) Survey images showing slice orientations. B) Fat fraction maps at both slice orientations. C) Temperature maps at subsequent time points in the sagittal (top) and coronal (bottom) orientations. There is no appreciable oscillation in temperature due to respiration or cardiac cycle for either method.

3.4.4 *In vivo* Liver

Figure 3.12 shows temperature maps of the unheated liver during free breathing computed with the fat-referenced and model-based methods. The fat-referenced reconstruction did not compensate for motion, and had errors greater than ±10°C dependent on how closely the time point's motion state matched the single baseline. In comparison, the model-based maps had an average temperature error of 0.27°C throughout the time course. The same trend holds true regardless of the slice orientation, where the model-based maps have low

temperature error regardless of in-plane or through-plane motion.

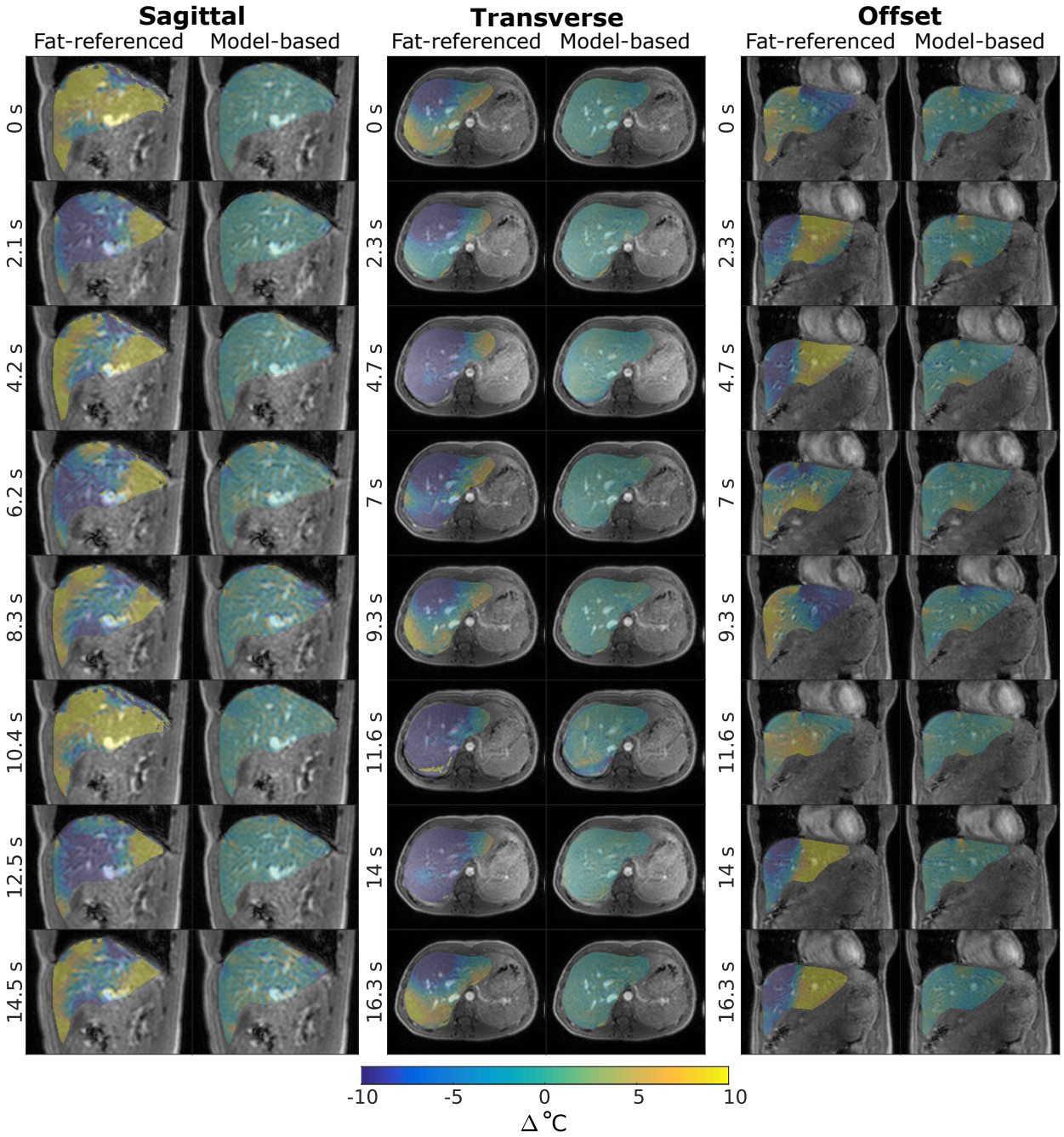

Figure 3.12: Comparison of temperature errors in multple slice orientations in the liver of a free-breathing volunteer. The fat-referenced method is unable to account for motion in any orientation, with temperature errors greater than 10°C. In all cases,model-based temperature maps have low error throughout the liver, with larger errors near intestinal walls due to unpredictable motion.

3.5 Discussion

3.5.1 Summary of results

We described and validated a new signal model and temperature reconstruction for PRF-shift hybrid multibaseline referenceless MR thermometry in aqueous and mixed water/fat tissues. The signal model combines state-of-the-art, iterative water/fat separation with a motion- and off-resonance shift-robust penalized-likelihood temperature reconstruction to achieve accurate and precise water/fat-separated thermometry with short compute times. The algorithm achieved lower temperature error in mixed fatty tissues compared to conventional methods, particularly in cases where dynamic off-resonance shifts were large or rapidly varying across the image. The algorithm's multibaseline functionality was able to account for cyclical respiratory motion using a library of baseline water and fat images. The algorithm performed accurately up to 90% fat, even in tissue where no fat was present. Its ability to incorporate water voxels in both the heating and off-resonance shift fitting makes the approach widely useful compared to the fat-referenced algorithm, which estimates off-resonance shifts from fat only and must extrapolate shits to voxels without fat. Simulations on a numerical water/fat phantom showed low temperature errors across temperature levels and fat fractions, and demonstrated robustness to large or high order off-resonance shifts and motion, scenarios where the fat-referenced method fails. This accuracy was confirmed in a porcine MRgFUS ablation experiment where the model-based method computed temperature maps in 0.47 s per time point with an RMS error of 0.66°C. The algorithm was precise *in vivo* in a free-breathing volunteer and capable of correcting non-uniform off-resonance shifts due to the presence of lung motion. Motion-compensation was confirmed in a free-breathing liver, achieving negligible error where the fat-referenced method contained errors of 10°C or more. These results are consisted with Ref. [15], which demonstrated liver errors smaller than 1°C with the hybrid referenceless multibaseline method.

3.5.2 Fat-suppressed thermometry with few echoes

Multiple gradient echo images are required to obtain accurate water/fat separations of baseline images, but subsequent heating images theoretically only require a single echo to fit the model and estimate temperature while maintaining fat suppression. In practice, the noise of the resulting temperature map increased as the number of echoes used decreases, but results from the simulations and MRgFUS heating experiment showed that accuracy remained comparable to that of the full echo case. Reducing the number of echoes acquired during heating presents an opportunity to use the freed-up sequence time for various applications. One possibility is to add gradient pulses between the excitation and echo time to enable acoustic radiation force measurements [113] simultaneously with fat-suppressed thermometry. Sequence time could also be used for scan acceleration using PRESTO echo shifting [114, 115] or echo planar readouts [116]. Using less echoes also reduces the computation time required for the algorithm to generate temperature maps, making this implementation compatible with accelerated imaging methods.

3.5.3 Limitations and Future Work

One recognized limitation of the method is the potential for changes in fat susceptibility with heating [53] to introduce localized off-resonance that may not be accurately modeled by a low order polynomial. This is a problem common to most PRF thermometry methods, and the magnitude of the effect depends on the heating geometry and intensity, and slice orientation. Depending on the application and orientation the apparent temperature error due to susceptibility could be negligible, such as during feedback controlled hyperthermia. For ablative applications where the expected temperature rise is greater than 20°C, the expected error due to susceptibility could be a confound depending on target size, however in these applications the main goal is tissue necrosis rather than sustaining an exact temperature rise.

In the original hybrid method (Ref. [15]) the ℓ_1 norm was the only feature that prevented the phase shift due to heating from being misinterpreted as a change in off-resonance due to scanner drift or respiration. When the area of heating was no longer sparse with respect to the image size, such as during near-field heating and hyperthermic therapies, the ℓ_1 sparsity regularization could no longer separate these two effects, leading to erroneous temperature maps and a sensitivity to the choice of sparsity regularization parameter λ. In the model-based method discussed here, the fat serves as an additional reference and aids the sparsity regularization in separating the frequency shift due to heating from that of off-resonance, even when the hotspot becomes large with respect to image size (Figure 3.13). The model-based method is insensitive to the choice of λ as long as $\lambda < 10^{-2}$, a value that is achievable for a variety of imaged geometries with proper normalization of the data, as shown in this work. Below this threshold tuning of λ would likely not be required in a live treatment scenario but could be performed prior to treatment in simulation, as suggested in Ref. [15].

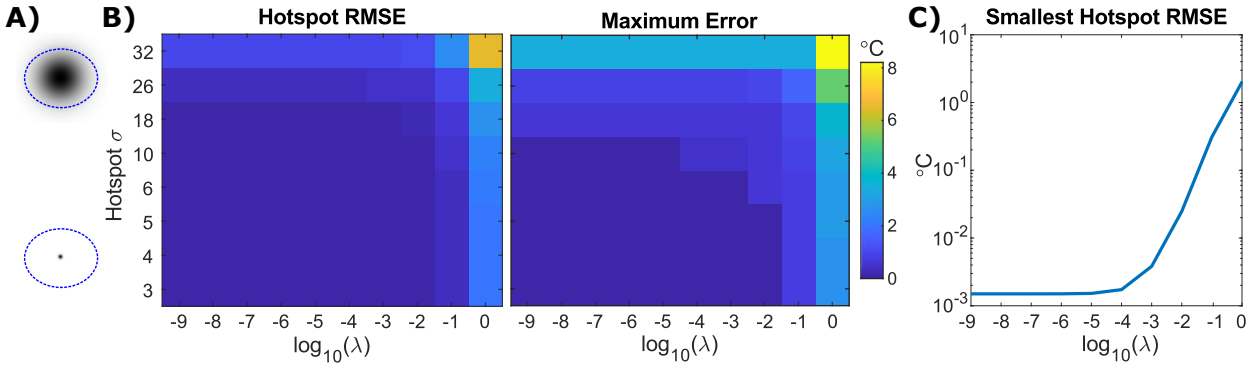

Figure 3.13: Sensitivity to sparsity regularization and hotspot size simulation. A) Range of hotspot sizes explored (black Gaussian) referenced to size of the phantom (blue dotted line). B) Hotspot RMS and maximum error for each hotspot size over a range of regularization values (λ). The algorithm is insensitive to values of $\lambda \leq 10^{-3}$ and hotspot size, until $\sigma \geq 26$. C) RMSE versus λ for the smallest hotspot shows an optimal choice of to be $10^{-4} \leq \lambda \leq 10^{-3}$.

Since the algorithm relies on an underlying water PRF-shift, voxels containing greater than 90% fat will contain erroneous temperature information. For most therapeutic cancer applications, the tumor has a strong water signal and the algorithm would perform adequately even when the tumor is mixed with surrounding fatty tissues. Erroneous voxels

are straightforward to mask out with the computed fat fraction maps, but doing so would prevent near-field monitoring of intervening fat tissues. The few-echo embodiment of the algorithm could allow for added pulses and readouts for fat temperature-sensitive contrast mechanisms [48].

Finally, the algorithm does not account for changes in R_2^* with temperature. Addition of this effect could enable joint PRF-R_2^* temperature mapping, given a characterization of R_2^*'s dependence on temperature for a specific tissue, and is a topic for future work.

3.6 Conclusions

We demonstrated a model-based multi-echo fat-suppressed approach for PRF-shift temperature mapping in fatty tissues. The algorithm leverages hybrid multibaseline referenceless thermometry approaches and state-of-the-art, iterative water/fat separation techniques in a penalized likelihood optimization scheme to account for the fat signal in mixed tissues. The method was proven accurate and precise with online-compatible compute times, irrespective of fat content up to 90% fat, tissue motion, large and spatially-varying off-resonance shift, or number of echoes. It was validated in simulations, phantom heating experiments, and *in vivo* breast and liver experiments and could be critically useful in monitoring ablative therapies in fatty tissues such as breast or liver.

3.7 Availability of data and materials

The code needed to implement the thermometry algorithm outlined in this article is available in the waterFatSeparatedMRThermometry repository, https://github.com/poormanme/waterFatSeparated_MRThermometry.

3.8 Acknowledgments

The authors would like to thank Charles Mougenot, Clemens Bos, and Roel Deckers for their experimental support. This work was supported by DoD W81XWH-13-1-0230, NIH T32EB021937, a Vanderbilt University Central Discovery Grant, and a Whitaker International Program Summer Grant.

Chapter 4

ORIENTATION-INDEPENDENT Z-SHIMMED TEMPERATURE MAPPING NEAR ABLATION PROBES

4.1 Introduction

One area where minimally invasive thermal therapies have shown promise is in hippocampal ablation for the treatment of localized epilepsy. Despite the high numbers of drug refractory epilepsy cases, surgical approaches are underutilized 90% of the time in the United States [2] in part due to physician hesitance to operate on delicate brain structures given the associated risks [117]. Minimally-invasive thermal ablation is a viable alternative to traditional resection approaches. However, current percutaneous ablative therapies for epilepsy, such as laser ablation, require a surgical craniotomy and the probe must pass through a significant stretch of viable and delicate brain tissue to reach the target region [2]. Recently, an alternative approach was proposed by collaborators using robotic steering and helical metallic needles to access the hippocampus through the foramen ovale [74]. This 4 mm by 2 mm window in the base of the skull provides therapeutic access to the brain without needing to open the skull. Magnetic resonance guidance can be employed in these procedures to obtain real-time, spatially-resolved temperature maps of the target region [1] using the proton resonant frequency - shift (PRFS) [10, 12]. However, due to magnetic susceptibility mismatching between the RF ablation probes used by the robot and brain tissue, large MR signal loss can occur in the near-probe region [60]. This signal loss obscures the target anatomy and makes temperature measurements imprecise or impossible. There is a need for a real-time thermometry method that recovers the signal loss and temperature precision near the probe.

Previously, we developed a dual-echo Z-shimmed sequence that recovered signal near the probe for more precise temperature mapping [80]. However, this method required extensive

manual tuning of the Z-shim for each probe and slice orientation, which is infeasible for real-time implementation. To overcome this limitation, this chapter develops a multiple-echo Z-shim sequence and automated calibration method to optimize the sequence in simulation. Multiple echoes allows multiple Z-shim strengths to be applied at once to fill in the signal loss across all probe and slice orientations. A simulated automatic calibration tool was developed to optimize the multi-echo Z-shim for any probe or slice orientation, allowing the sequence to be optimized prior to acquisition of images at the scanner, where time is more critical. The optimized multiple echo Z-shimmed sequence robustly recovers MR temperature precision near an RF ablation probe without the need for manual tuning of refocusing gradients for different probe angles and slice orientations.

4.2 Methods

4.2.1 Pulse Sequence

Figure 4.1 shows the proposed multiple echo Z-shimmed sequence. Each echo is shimmed individually by p% of the full refocusing gradient area in the slice (Z) direction. This partial refocusing of each echo image compensates through-slice phase accrual caused by off resonance and yields signal only in specific bands of the image, depending on the off-resonance experienced by that area. Estimating temperature from all echoes provides high precision in all parts of the image. Because the near-probe off-resonance changes depending on probe orientation and imaging parameters, the refocusing gradients applied must be optimized to fully recover all lost signal. For this application, gradient areas were allows to vary between 0% and 200% of the full refocusing gradient area.

4.2.2 Susceptibility Simulator

While previous dual-echo work relied on scanner-side tuning of gradient strengths, this is not feasible for the multiple echo approach due to the larger number of echoes. To this end

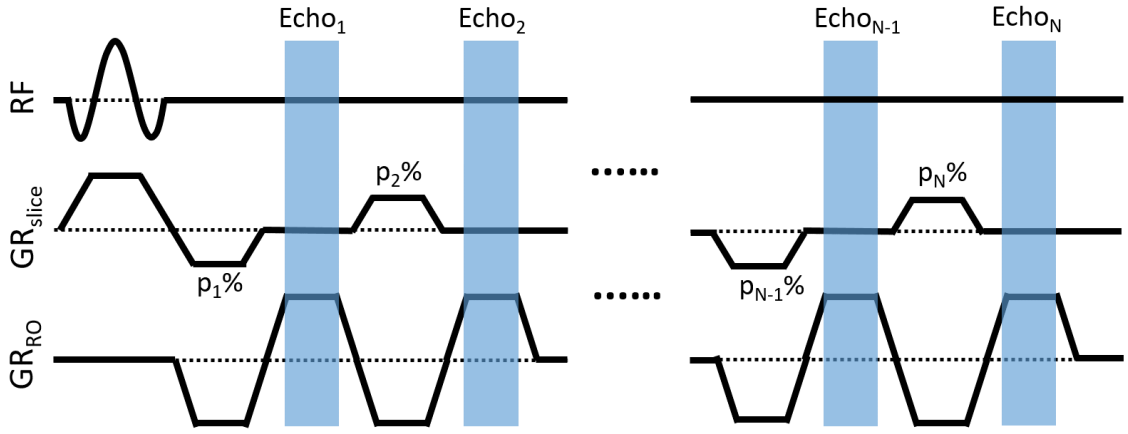

Figure 4.1: Each echo was shimmed separately in the slice dimension by a percentage, $p\%$, of the full refocusing gradient area.

an MR image simulator was designed to take a given probe geometry and material, compute the off-resonance caused by that probe in an aqueous volume, and generate images from the volume given a scan geometry. Z-shimming can be applied to these images in simulation and used to evaluate the temperature SNR (tSNR) recovered by a particular Z-shim gradient refocusing sceheme. To generate the off-resonance maps, a fast Fourier transform method was used to compute the local magnetic field changes caused by the magnetic susceptibility of the probe [118, 119, 120]. These methods rely on first-order approximations of Maxwell's electromagnetic equations that allow for fast computation of susceptibility-induced dipole fields based entirely on a known distribution of material susceptibilities within a volume. This method has shown acceptable accuracy within a volume for *in vivo* applications [121]. The susceptibility mismatch of the probe and tissue causes two effects on the local magnetic field, a direct effect from a given molecule in the object and the summation of effects from molecules elsewhere in the object. The molecule being examined is assumed to lie within a sphere of Lorentz [122], allowing the magnetic field experienced by a nucleus to be defined as:

$$B_{nuc}(\overrightarrow{r}) \approx H_0 \left(1 - \frac{1}{3}\chi(\overrightarrow{r})\right) + h_{in,z} \tag{4.1}$$

where B_{nuc} is the magnetic field experienced by a nucleus, H_0 is uniform main magnetic field, χ is the magnetic susceptibility at position $\overrightarrow{r}$, and $h_{in,z}$ is the perturbing magnetic field in the z direction. Using magnetostatic equations as outlined in Ref. [118], the perturbation field can be computed with a Fourier transform by:

$$h_{in,z}(k) = -H_0 \left(\frac{1}{3} - \frac{k_z^2}{k_x^2 + k_y^2 + k_z^2}\right) FT[\chi(k)] \tag{4.2}$$

where k is the three dimensional Fourier coordinate. Combining these two equations yields Equation 4.3, which allows the off-resonance volume ω_{nuc} at position $\overrightarrow{r}$ to be computed based on fast Fourier transforms of the susceptibility distribution, scaled by the gyromagnetic ratio, γ, and the field strength B_0.

$$\omega_{nuc}(\overrightarrow{r}) = B_0 \gamma FT^{-1}\left[\left(\frac{1}{3} - \frac{k_z^2}{k_x^2 + k_y^2 + k_z^2}\right) FT[\chi(k)]\right] \tag{4.3}$$

To this 3D volume of off-resonance, a slice-selective RF gradient is added such that the frequency ramp applied is $\Delta F = \gamma G \Delta z$, where G is the full refocusing gradient strength and Δz is the slice thickness. A sinc RF pulse is simulated and applied to excite frequencies within the appropriate band. As on the scanner, the expected rectangular slice selection profile will be distorted in areas near the probe due to the underlying off-resonance. The phase accrual (Φ_{nuc}) at the nth echo time due to the magnetic susceptibility of the probe is calculated such that $\Phi_{nuc,n}(\overrightarrow{r}) = TE_n \omega_{nuc}(\overrightarrow{r})$. After slice selection, Z-shimming can be applied to each echo n such that the phase accrual is $\Phi_{zshim,n}(\overrightarrow{r}) = \gamma \frac{p_n - 100}{100} Gz(\overrightarrow{r})$ where p_n is the Z-shim percentage for echo n and $p_n = 100$ is a fully refocused image. G is the fully refocused gradient area in $\frac{mT \cdot s}{m}$, and $z(\overrightarrow{r})$ is the slice thickness. The effective phase due to off-resonance and Z-shimming can be described as $\Delta\Phi_n(\overrightarrow{r}) = \Phi_{nuc,n}(\overrightarrow{r}) - \Phi_{zshim,n}(\overrightarrow{r})$. The computed phase is integrated over the volume and downsampled to the imaging resolution

by convolving with a rect function. This convolution integrates the phases within each voxel to account for intravoxel dephasing. The resulting off-resoance map is converted to tSNR for each voxel position $\overrightarrow{r}$ according to Equation 4.4.

$$tSNR_n(\overrightarrow{r}) = TE_n e^{TE_n/T_2^*} \left| \int e^{-i\Delta\Phi_n(\overrightarrow{r})} dV \right|. \tag{4.4}$$

This equation reflects the knowledge that in areas of no off-resonance, tSNR is maximized when the echo time $TE \approx T_2^*$ [22], and thus excludes terms independent of TE. When off-resonance is present, the volume integral will decay with TE, suggesting that the largest Z-shimming gradients should be applied at the shorter echo times to acquire areas of highest off-resonance.

4.2.3 Sequence Optimization

The sequence was optimized using an exhaustive search method outlined in Figure 4.2. This method relied on the simulator to test the recovery of all possible refocusing schemes and select the scheme that maximized the number of voxels with recovered tSNR near the probe.

Six feasible echo times were selected (TE = 1.5, 3.5, 5.5, 7.5, 9.5, 11.5 ms) that could be implemented on the scanner with read-out bandwidth of 1085 Hz and 1.5 X 1.5 mm voxels. A 1 mm diameter cylindrical nitinol probe ($\chi = 245 \times 10^{-6}$ppm) was simulated within a 120 x 120 x 120 mm aqueous volume ($\chi = -9 \times 10^{-6}$ppm) [123]. The probe was positioned with the tip at the center of the volume and off-resonance maps were generated on a 0.25 x 0.25 x 0.25 grid with the probe orientated 0°,45°, and 90° with respect to B_0. A slice-selective RF pulse with 4 mm thick excitation profile was applied to the volume either parallel or perpendicular to the probe to generate images which requires a gradient area of 25.6 $\frac{mT \cdot s}{m}$ to obtain a conventional, fully refocused image (100% refocused). The probe and slice orientations simulated can be seen in Figure 4.3.

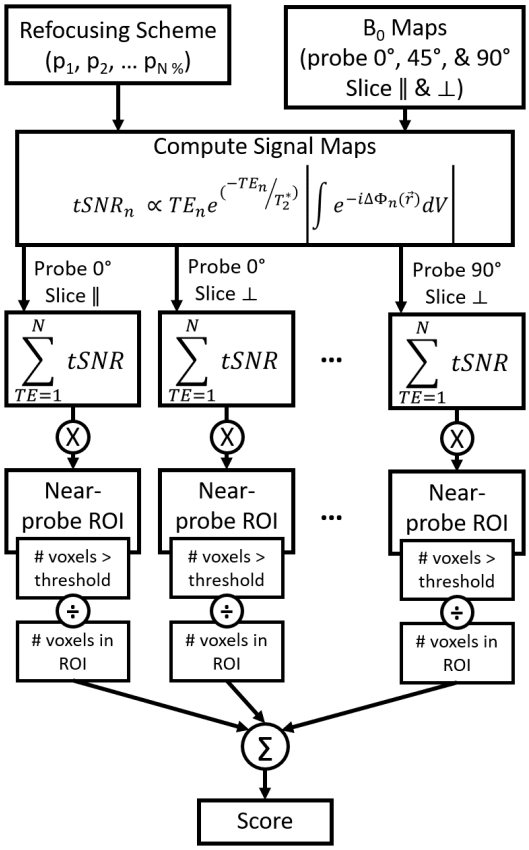

Figure 4.2: Simulation scheme for finding the refocusing gradient scheme that recovered the most near-probe signal across all orientations. Simulated B_0 maps were used to characterize the through-slice gradient amplitude at each point around the probe. An exhaustive search was performed to obtain the optimal refocusing scheme.

For each orientation, the simulator was used to first generate single echo images without any Z-shimming (1.5 x 1.5 x 4 mm voxels, TE = 11.5 ms). The full width half max of the signal loss of each orientation was used to create an orientation-specific near-probe ROI that was used to evaluate signal recovery. Next, all possible refocusing schemes of 6 echoes with a fully-refocused last echo were generated. The simulated refocusing gradient areas were restricted to have values of p_n = 0 to 200% of the full refocusing area (0 to 51.2 $\frac{mT \cdot s}{m}$). This range is based on prior knowledge [124] that the absolute off-resonance expected from the probe will not exceed 1000 Hz (phase between -π and π radians) and thus can be compensated by these gradient areas. Since tSNR in areas of high off-resonance will be maximized at shorter echo times, schemes that did not descend in shim gradient strength

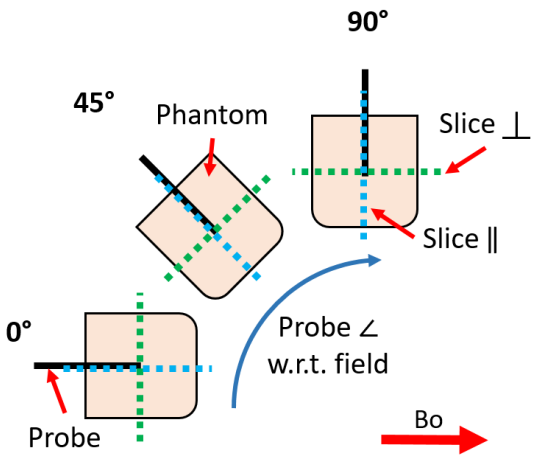

Figure 4.3: Schematic of probe and slice orientations considered in the optimization. Field distortions near the probe cause through-slice and in-plane gradients that are orientation-dependent.

were eliminated. Each Z-shim refocusing scheme was applied in turn for each probe angle and slice orientation, and the simulator generated a tSNR map based on the off-resonance map and applied Z-shimming. The root sum squared (RSS) tSNR value was computed across all echoes and the fraction of voxels with RSS tSNR greater than a threshold within each orientation's ROI was recorded as a score. The threshold was set to one third of the maximum tSNR value, which occurs at the last echo according to $threshold = \frac{1}{3} TE_6 e^{TE_6/T_2^*}$. The scheme receiving the highest score per probe and slice orientation was recorded in a look-up table (LUT) to yield schemes optimized to a given scenario. The scores were then summed across all orientations and the scheme yielding the highest score was selected as a master, or best average, refocusing scheme that could be applied regardless of probe angle and slice orientation. The gradient strengths applied on the scanner, $\tilde{p}_n$ were computed according to Equation 4.5, which accounts for phase accrual over the sequence time.

$$\tilde{p}_n = \begin{cases} p_n & , n = 1 \\ p_n - p_{n-1} & , n \geq 2 \end{cases} \tag{4.5}$$

4.2.4 Temperature Estimation

Temperature was estimated from acquired images using the multi-echo hybrid reference-less multibaseline method [15], modified to estimate temperature from all echoes jointly. In this method, images during heating are modeled as:

$$y_j = x_j e^{\imath 2\pi(\{\boldsymbol{A}\boldsymbol{c}\}_j + f_j)TE} + \epsilon_j, \tag{4.6}$$

where y_j is the complex-valued heating image signal and x_j is the complex-valued baseline image at voxel j. The polynomial basis function matrix $\boldsymbol{A}$ is multiplied by the coefficient vector $\boldsymbol{c}$ to model dynamic off-resonance changes unrelated to heating. f_j is the frequency shift due to heating, TE is the echo time, and ϵ_j is complex-valued Gaussian noise. To solve for the unknowns $\boldsymbol{c}$ and $\boldsymbol{f}$, Equation 4.6 is fit to acquired multiple echo images, $\boldsymbol{y}_1$ to $\boldsymbol{y}_n$ where n is the number of echoes, by minimizing an ℓ_1 penalized likelihood least squares cost function (Equation 4.7) with a descent algorithm.

$$\Psi(f, \boldsymbol{c}) = \sum_{n=1}^{N_e} \left[\sum_{j=1}^{N_s} \frac{1}{2} \left| \tilde{y}_{n,j} - y_{n,j}(f_{n,j}, \boldsymbol{c}) \right|^2 \right] + \lambda ||\boldsymbol{f}||_1 \tag{4.7}$$

In this equation, $\tilde{y}_{n,j}$ is the acquired image of echo n and voxel j, $y_{n,j}(f_{n,j}, \boldsymbol{c})$ is the model, N_e is the number of echoes, N_s is the number of voxels, and λ is the ℓ_1 sparsity regularization parameter, which reflects the prior knowledge that heating will be localized to a minority of image voxels. Similarly to Ref. [15], $\boldsymbol{f}$ and $\boldsymbol{c}$ are updated iteratively, minimizing one while the other is held constant. The frequency shift due to heating, $\boldsymbol{f}$, is restricted to negative values since a temperature increase causes a negative frequency shift. After the initial minimization, the process is repeated without the sparsity constraint ($\lambda = 0$) in voxels containing greater than 0.5°C to prevent downward temperature bias from the ℓ_1 regularization. The solved heating can be converted from frequency to degrees Celsius by:

$$\Delta T_j = \frac{2\pi f_j}{\alpha \gamma B_0} \tag{4.8}$$

where $\alpha = -0.01 ppm/^{\circ}C$. The code used to implement this temperature mapping method can be found in Ref. [80]. All reconstructions were performed in MATLAB on a 2.8 GHz dual 6-core Xeon desktop computer running Ubuntu 16.04 with 128 GB RAM.

4.2.5 Experiments

4.2.5.1 Simulation Validation

To validate the susceptibility simulation two agar phantoms (1% w/v) were created with either a spherical air void (40 mm diameter, $\chi = 0.36 \times 10^{-6}$ppm) or nitinol RF ablation probe (1 mm diameter, $\chi = 245 \times 10^{-6}$ppm) embedded in them. Each phantom was placed individually in a 32 channel head coil and off-resonance maps were acquired at 3T (Philips Achieva, Best, Netherlands) using the built in B_0 mapping tool with a gradient echo sequence (ΔTE = 1 ms, 1.5 x 1.5 x 1.5 mm voxels). The nitinol probe phantom was imaged with the probe in two orientations, etiher 0° or 90° with respect to the main magnetic field. The acquired B_0 maps were compared to simulated off-resonance maps of the same geometries generated with the simulation tool.

4.2.5.2 Optimal Scheme Selection

The tSNR recovery for each probe and slice orientation was examined in simulation to compare the master refocusing scheme and LUT schemes. The simulation tool and sequence optimization were performed for two different probe sizes, a 1 mm diameter nitinol RF ablation probe used for robotic hippocampal ablation [125] and a 2.5 mm diameter nitinol wire. A set of possible refocusing schemes were generated using values $p_n = 0$ to 200% in 20% steps. For each size of needle, the temperature SNR recovery with all possible refocusing schemes was computed and scored at each probe angle and slice orientation. For

each case, the look-up table and master schemes were selected and the simulated RSS tSNR was compared between the LUT and master schemes for each probe size.

4.2.5.3 Signal Recovery

Based on the simulated RSS tSNR results, the master refocusing scheme was chosen for implementation on the scanner. The 1 mm diameter nitinol ablation probe was embedded in a block of tofu and placed in the 32 channel head coil at 3T. A grounding wire was placed underneath the tofu block to enable RF heating. To measure near-probe signal recovery, four sets of images were acquired with the probe oriented 0° and 90° with respect to B_0 and a 4mm thick slice either parallel or perpendicular to the probe. Perpendicular slices were placed at the end of the probe tip and parallel slices were centered on the probe in the same plane. Z-shimmed gradient echo images were acquired at each probe and slice location with parameters matched to the simulated optimization (TE = 1.5 to 11.5 ms, 6 echoes, TR = 45, 1085 Hz bandwidth, 1.5 x 1.5 mm voxels, and 4 mm slice thickness). A high read-out bandwidth (1085 Hz) was used to minimize in-plane distortions. The RSS image was computed across all echoes and near-probe RSS signal was compared to that of the last echo alone (TE = 11.5ms), which was fully refocused as in a conventional gradient echo sequence.

4.2.5.4 Temperature Mapping

To measure precision, the same sequence as above was used to acquire four sets of 100 images of the tofu phantom at the same probe and slice orientations. Z-shimmed temperature maps were estimated from all echoes and compared to those computed with the conventional, fully-refocused, last echo. Temperature mapping was performed with a 3rd order polynomial off-resonance fit to account for inhomogenous field drift due to the grounding wire. After acquiring images without heating an RF generator was used to apply heating with the 1 mm diameter probe (45 W for 2.5 minutes) at each probe and slice orientation. The same

sequence used to measure temperature precision was acquired immediately post-ablation to monitor cooling. Temperature maps were computed relative to the last image set at the completely-cooled state and compared between the Z-shimmed and conventional images.

4.2.5.5 Step Size Effects

Based on temperature mapping results with the 20% step size schemes, simulated recovery was assessed using refocusing schemes generated with a 10% step size. The 1 mm diameter and 2.5 mm diameter wires were simulated within an aqueous volume as described in Section 4.2.5.2 and refocusing schemes were generated using values $p_n = 0$ to 200% in 10% steps. For each size of needle, the temperature SNR recovery with all possible refocusing schemes was computed and scored at each probe angle and slice orientation.

4.3 Results

4.3.1 Simulation Validation

Figure 4.4 compares off-resonance maps computed with the simulation tool and those acquired at the scanner. No geometric image distortions were observed, allowing direct comparison to be made. The simulated off-resonance maps are well correlated with the acquired maps, with orientation-dependent high-order shifts occurring near the embedded object. A dipole pattern appears around the spherical air void (Figure 4.4 top) that is also seen in the acquired off-resonance map. The magnitude of off-resonance is in agreement between the simulations and acquired data, confirming the susceptibility value of air used ($\chi = 0.36 \times 10^{-6}$ppm). The edges of the agar phantom are visible in the acquired B_0 map where small areas of off-resonance can be seen due to susceptibility mismatch at the air-phantom boundary. This pattern is not visible in the simulations as the spherical void was placed within an infinite water volume. For the 1 mm nitinol probe oriented parallel and perpendicular to the field, good agreement is seen between the off-resonance pattern,

dependent on orientation. The highest areas of off-resonance are seen nearest the probe in a dipole pattern and lessen in magnitude as distance from the probe increases. In the simulated case, the needle location can be seen as containing no off-resonance since no MR signal can be acquired from the needle itself. The needle location is obscured in the acquired off-resonance maps due to partial volume effects with the scan resolution used (1.5 mm isotropic voxels). The low scan resolution when compared to simulated resolution (1.5 mm vs 0.25 mm isotropic voxels respectively) also contributed to the off-resonance magnitude discrepancies seen near-probe. In the 90° probe location, the sharp increase in frequency seen in the middle of the image is due to low image signal immediately next to the needle and can be disregarded. Good agreement in off-resonance magnitude is seen a few millimeters away from the probe, confirming the susceptibility value used for nitinol ($\chi = 245 \times 10^{-6}$ppm).

Figure 4.5 shows a comparison between simulated and acquired images, without applied Z-shimming. Signal voids up to 1 cm in diameter can be seen near the ablation probe that change shape depending on probe and slice orientation within the magnetic field. The signal void shapes correlates well between images generated with the simulation tool and those acquired at the scanner. The largest signal loss artifact is seen when the probe is oriented 90° with respect to B_0, as the off-resonance becomes more dipole-like.

4.3.2 Optimal Scheme Selection

A comparison between RSS tSNR images simulated of the 1 mm probe with and without Z-shimming for both the master and LUT schemes can be seen in Figure 4.6. Qualitatively, both the master and LUT schemes adequately fill in the region of signal loss. Table 4.1(top) reports the fraction of near-probe voxels recovered near the 1 mm probe at each angle and slice orientation, including the 45° probe angle. A recovery score of 100 % means every voxel in the near-probe ROI was recovered above the threshold. Based on the TE and T_2^* estimates used in this work, the maximum achievable tSNR value was 0.079. On average across all probe angles and slice orientations, the master scheme had a recovery score of 92% and an

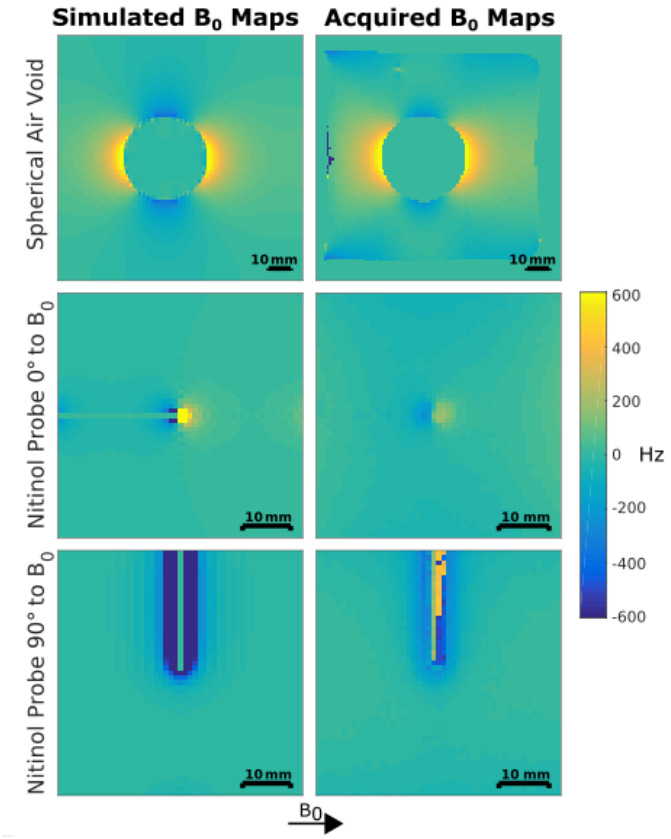

Figure 4.4: (left) Field maps simulated using the developed tool for a spherical air void and nitinol ablation probe at two orientations within the magnetic field. (right) Acquired field maps of the objects. High order field variations can be seen near the objects with good correlation between the simulated and acquired maps.

average near-probe tSNR of 0.045. The LUT had an average recovery score and near-probe tSNR of 97% and 0.047 respectively. For the no Z-shim case, the average near-probe tSNR was 0.006. While the fraction of near-probe voxels recovered increased when using the LUT over the master scheme, the improvement in mean near-probe tSNR between the master scheme and LUT schemes was negligible. The minimum recovery scores for the master and LUT schemes were 86% and 87% respectively. With both schemes, over half of the near-probe voxels showed recovery above the threshold in all orientations suggesting that there is little advantage to using the LUT approach for this probe size.

Figure 4.7 displays a comparison between RSS tSNR images simulated of the 2.5 mm wire with and without Z-shimming, with the master and LUT schemes. Both the master

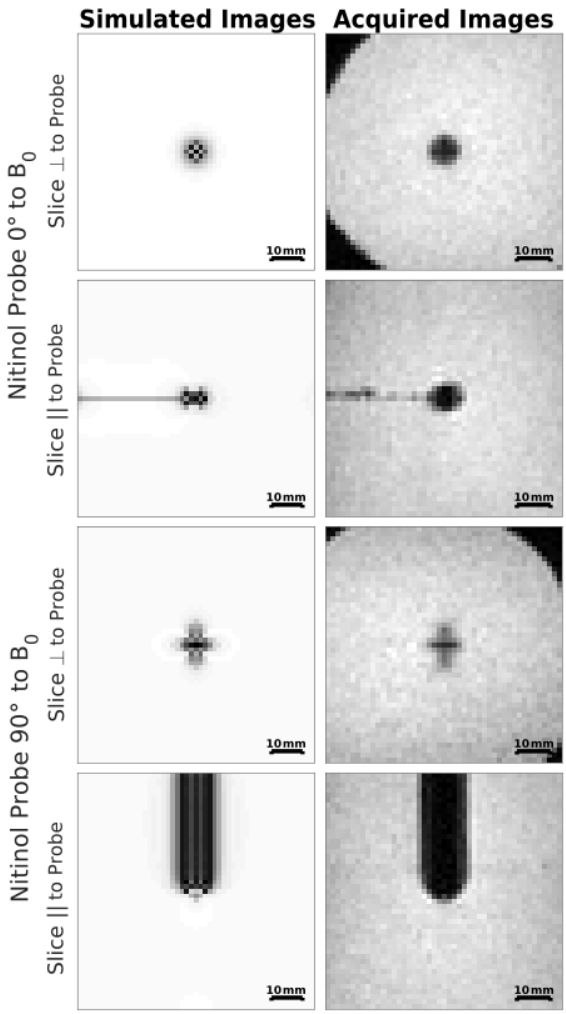

Figure 4.5: Validation of simulated gradient echo images. (Left) Images simulated of a nitinol ablation probe using the developed tool with no applied Z-shimming. (Right) Gradient echo acquired images of the ablation probe oriented within a 3T scanner. Good correlation in near-probe signal loss shape can be seen between the simulated and acquired images.

and LUT schemes recover near-probe signal, however the recovery is non-uniform across the area of signal loss. Orientation-specific information about recovery is shown in the bottom of Table 4.1. On average across all probe angles and slice orientations, the master scheme had a recovery score of 80% and an average near-probe tSNR of 0.042. The LUT had average an average recovery score and near-probe tSNR of 87% and 0.042 respectively. For the no Z-shim case, the average near-probe tSNR was 0.003. The minimum recovery score for the master and LUT were 61% and 73% respectively. With the 2.5 mm wire, the LUT recovered

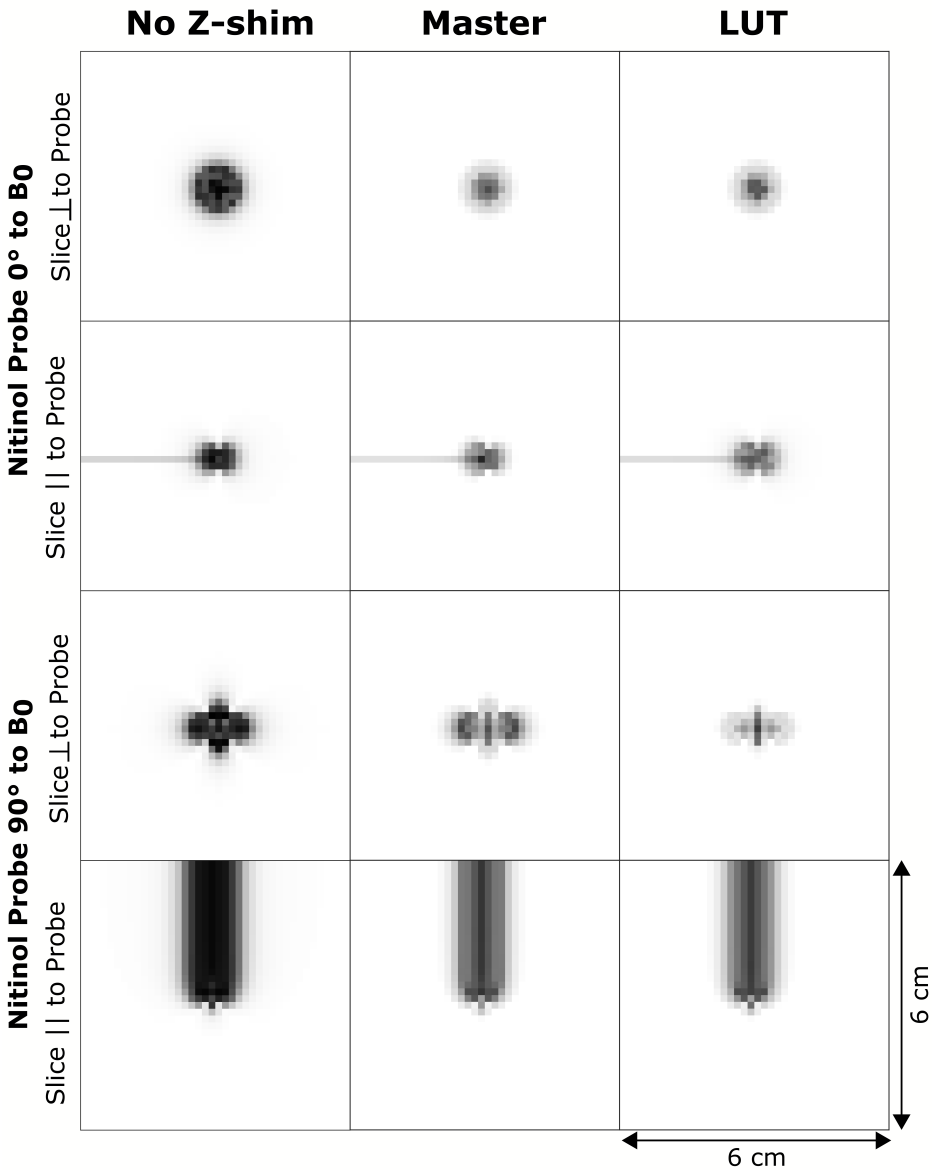

Figure 4.6: Scheme optimization comparison between the master and LUT for 1 mm probe with 20% step size. (left) tSNR with a conventional, single-echo scan with no Z-shimming. (middle) RSS tSNR recovered with the master scheme. (right) RSS tSNR recovered with the LUT schemes. With the 1 mm probe, the master and LUT schemes perform similarly and recover the lost signal regardless of probe angle and slice orientation.

a larger number of voxels near the probe than the master scheme but the average tSNR remained the same. In both cases the minimum recovery achieved was over half but less than three quarters of the near-probe voxels. This, combined with the non-uniformity of recovery, suggests that a finer step size when generating refocusing schemes might be needed

Table 4.1: Near-probe recovery for both nitinol probes with each scheme optimization technique of 20% step size. A recovery percentage of 100% means every voxel in the ROI was recovered above the threshold. The maximum average tSNR achievable was 0.079.

Probe Size	Angle w.r.t. B_0	Slice Direction	Master		LUT	
			Recovery	Avg. tSNR	Recovery	Avg. tSNR
1 mm	0°	$\perp$	97%	0.055	100%	0.055
		$\parallel$	94%	0.041	100%	0.039
	45°	$\perp$	100%	0.049	100%	0.051
		$\parallel$	86%	0.040	98%	0.040
	90°	$\perp$	88%	0.045	98%	0.061
		$\parallel$	87%	0.038	87%	0.040
2.5 mm	0°	$\perp$	96%	0.050	97%	0.047
		$\parallel$	83%	0.042	88%	0.033
	45°	$\perp$	81%	0.046	91%	0.048
		$\parallel$	72%	0.035	73%	0.033
	90°	$\perp$	88%	0.048	88%	0.054
		$\parallel$	61%	0.033	85%	0.035

when recovering signal around this diameter of probe.

For both the 1 mm and 2.5 mm sizes, each temperature SNR image took 1.75 seconds to compute per applied refocusing scheme. It took 13.8 minutes of computation time with 12 CPU cores running in parallel to test all refocusing schemes generated with the 20% step size for a single probe angle and slice orientation.

4.3.3 Signal Recovery

As highlighted by Figure 4.6, little signal recovery advantage is seen when using the master versus LUT schemes, for a 1 mm ablation probe. Due to ease of data acquisition, the master scheme was chosen for these experiments and had refocusing gradient scheme of $p_n =$ [200, 20, 180, 60, 140, 100]%, equivalent to a scanner scheme of $\tilde{p}_n =$ [200, -180, 160, -120, 80, -40]% or gradient areas of [51.20, -46.08, 40.96, -30.72, 20.48, -10.24] $\frac{mT \cdot s}{m}$. To illustrate how the Z-shimmed pulse sequence acquires data, Figure 4.8 shows a representative Z-shimmed

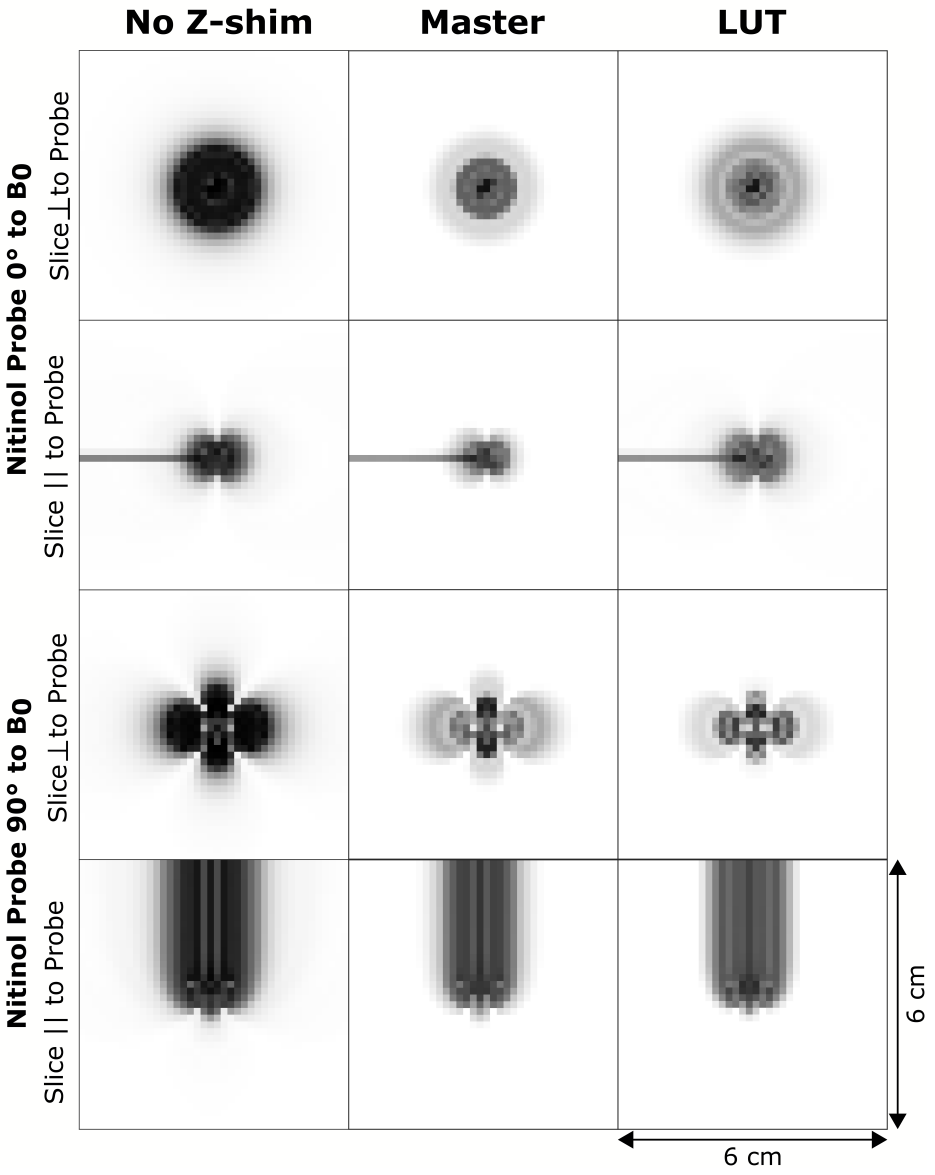

Figure 4.7: Scheme optimization comparison between the master and LUT for 2.5 mm wire with 20% step size. (left) tSNR with a conventional, single-echo scan with no Z-shimming. (middle) RSS tSNR recovered with the master scheme.. (right) RSS tSNR recovered with the LUT schemes.. With the 2.5 mm wire, the master and LUT schemes perform similarly and recover the lost signal regardless of probe angle and slice orientation. However, the recovery is non-uniform across the area of signal loss.

image set acquired on the scanner of the 1 mm nitinol probe at 90° with respect to B_0 and slice parallel to the probe. The first echo acquires signal closest to the probe while the last echo is a conventional, fully-refocused image with good signal far from the probe. Each echo

image contains a different band of signal recovery that, when combined, fill the area of lost signal visible in the final echo.

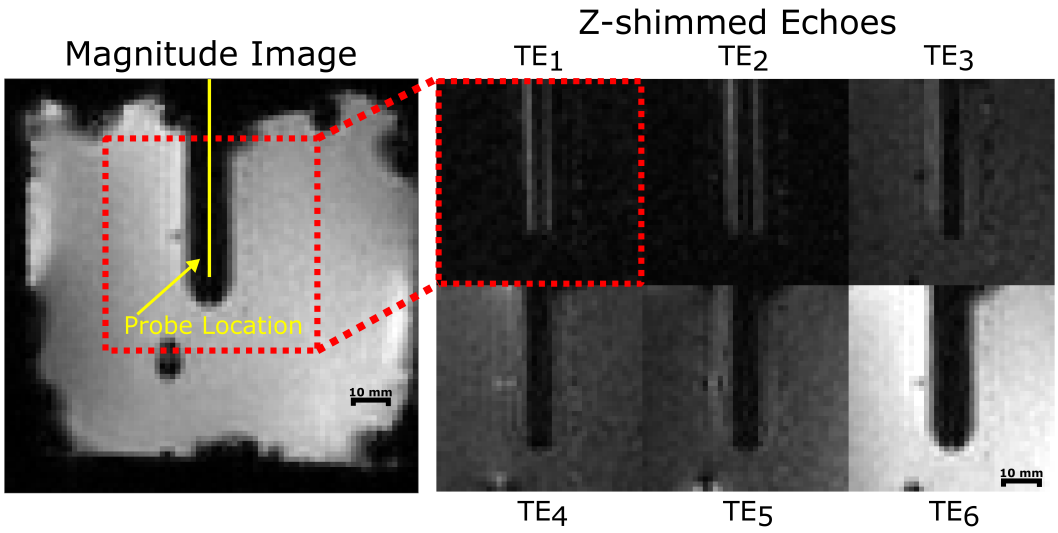

Figure 4.8: Representative echo images acquired with multiple echo Z-shimmed sequence. Each echo image has a different area of the image refocused, with the first echo containing signal nearest the probe and the last echo containing signal furthest from the probe.

Figure 4.9 shows the signal recovery of the optimized Z-shimmed sequence compared to the conventional, fully refocused echo. Signal was recovered in each case with the master optimized scheme, regardless of the probe angle or slice orientation. The 0° probe angle had 3.5 and 2.5 times increase in near-probe signal compared to the conventional sequence, in the perpendicular and parallel slices, respectively. The perpendicular slice recovered 100% of near-probe voxels and the parallel slice recovered 49%. The Z-shim sequence with the 90° probe angle recovered 5.2 and 4.1 times more signal than the conventional sequence in the perpendicular and parallel slices, corresponding to 70% and 52% of near-probe voxels recovered, respectively. The diameter of signal loss in the probe 90° orientation was 3 mm for the Z-shimmed sequence, compared to 13.5 mm for the conventional sequence.

4.3.4 Temperature Mapping

Figure 4.10 shows temperature standard deviation maps across probe angles and slice orientations. The mean near-probe temperature deviation and the number of voxels with a

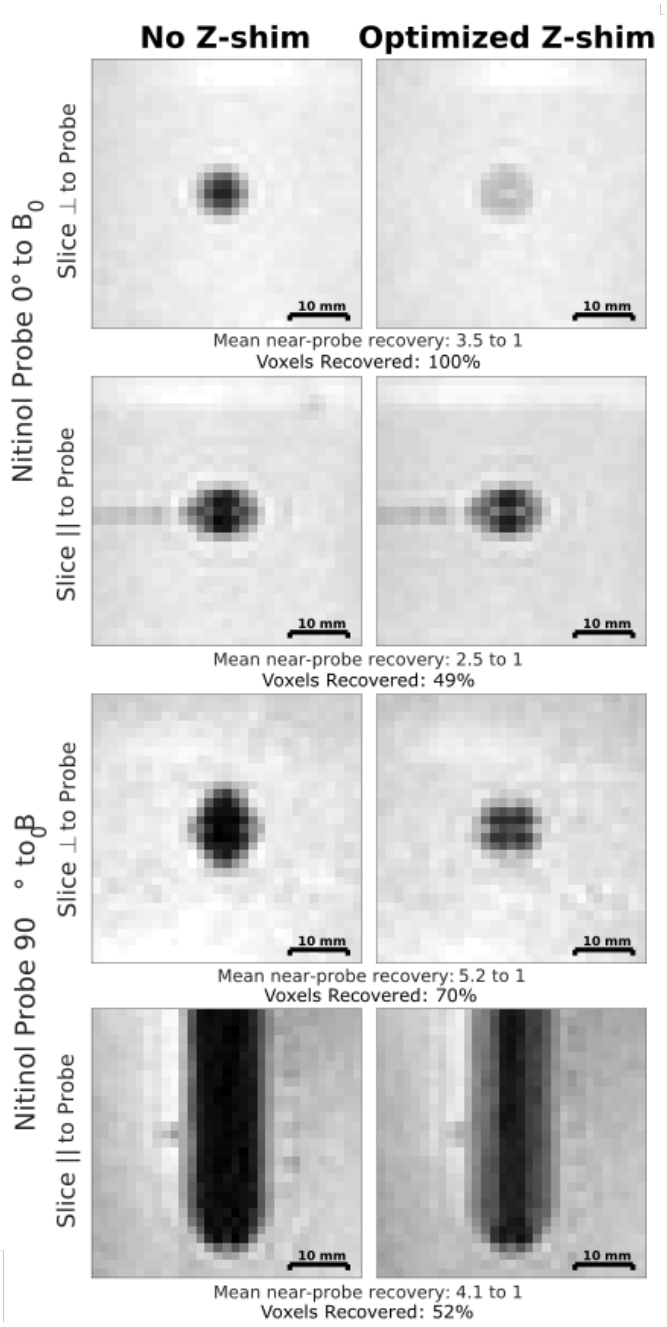

Figure 4.9: Signal recovery with master refocusing scheme. (Left) Conventional fully-refocused images at each probe and slice orientation computed with last, non Z-shimmed echo. (Right) Root sum squared signal of Z-shimmed sequence to visualize region of signal loss. Conventional images have an area of signal loss near the probe approximately 1 cm in diameter that is recovered by the optimized Z-shimmed sequence.

significant standard deviation (σ >1°C) are reported below each map. Regardless of probe and slice orientation, the Z-shimmed sequence with master refocusing scheme reduced near-

probe variation when compared to the conventional, single echo sequence. On average, the Z-shimmed scheme reduced the temperature error from 1.95°C to 0.93°C. The largest reduction was seen in the probe 90° and slice perpendicular case, with mean near-probe deviation decreasing from 3.22°C in the non Z-shimmed sequence to 0.88 °C with Z-shimming. The probe 0° slice parallel case saw the least improvement, which is consistent with the experimental signal recovery shown in Figure 4.9.

Figure 4.11 displays temperature maps taken immediately after RF ablation at each probe angle and slice orientation. The mean temperature in the near-probe ROI and number of voxels showing significant heat (σ >1°C) are reported for each orientation. Voxels that contained unreliable temperature measurements due to low image SNR were masked automatically by the temperature reconstruction algorithm. As a whole, the temperature maps obtained from the optimized Z-shim sequence are more complete than the single echo, no Z-shimmed case. The greatest improvement was seen in the probe 90° and slice parallel case, where the number of significant voxels increased from 48 to 218. In the no Z-shim case only the periphery of the hotspot could be reliably estimated and had a 10.5 mm gap in signal around the needle. Negligible improvement was seen between the two methods in the probe 0° and slice perpendicular case. This is likely due to the slice location, which was placed just after the tip of the probe. More improvement in this orientation would likely be seen as the slice was placed up the length of the probe further into the region of signal loss.

4.3.5 Step Size Effects

The results with the 2.5 mm wire and 20% step size in simulation (Figure 4.7) suggested that a finer step size might be needed for this larger diameter wire. Figure 4.12 shows the simulated recovery results using a 10% step size in refocusing scheme generation. Qualitatively the area of signal loss is more intensely filled with the smaller step size than when the larger step size was used. Table 4.2 shows the percent of recovered voxels and average tSNR in each orientation for each probe angle and slice orientation. On average the master scheme

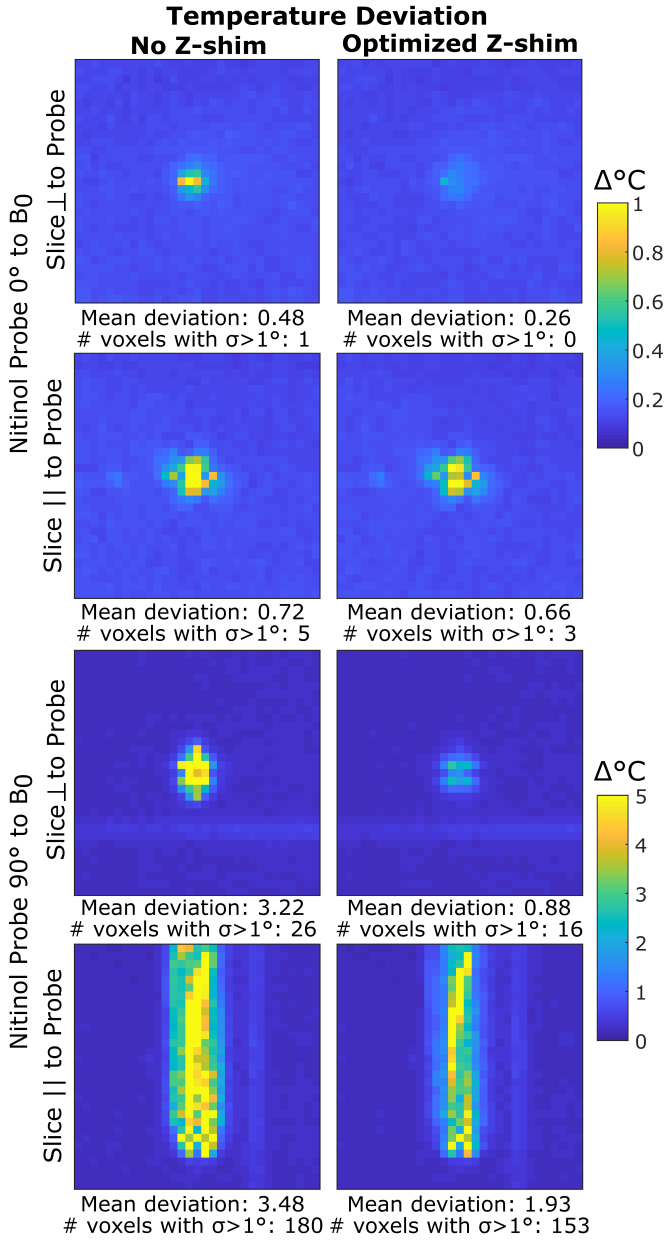

Figure 4.10: Temperature standard deviation maps with and without Z-shimming on 1 mm probe. Temperature standard deviation maps at room temperature computed from the last echo (conventional single gradient echo) without Z-shimming (left) and optimized Z-shim sequence (right). The optimized scheme reduces temperature variation near the probe across all orientations.

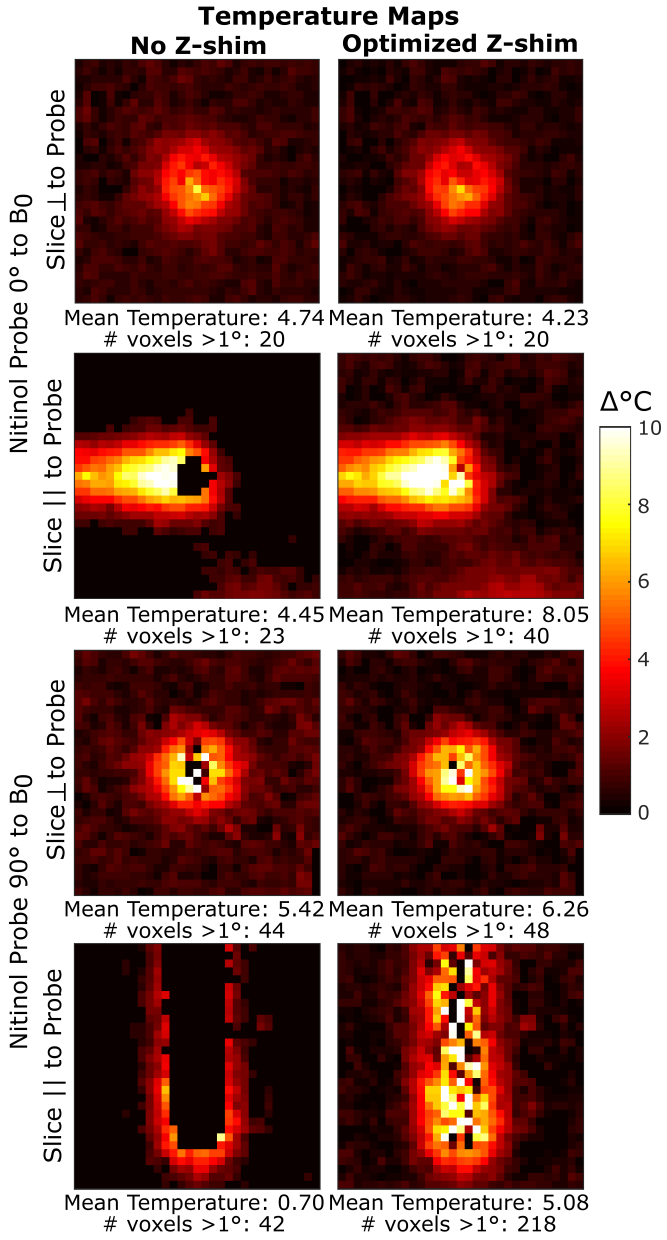

Figure 4.11: Temperature maps post- RF ablation with a 1 mm probe, with (multi-echo) and without (last echo) Z-shimming. The mean near-probe temperature and number of voxels with significant heat are displayed beneath each image. On average, the Z-shimmed temperature maps show a more complete hotspot with more voxels showing significant near-probe heating.

recovered 82% of near-probe voxels with a mean tSNR of 0.045 while the LUT recoverd 93% of voxels with a mean tSNR of 0.039. For the no Z-shim case, the average near-probe tSNR was 0.003. The minimum recovery score was 64% for the master scheme and 90% for the LUT schemes. Compared to the 20% step size for this diameter (Table 4.1) little change was seen in the percent of voxels recovered and mean tSNR with the master scheme. The LUT scheme with smaller step sized increased the number of voxels recovered but slightly decreased the mean tSNR compared to the larger step size case. Since the number of possible refocusing schemes increased when the step size was decreased, the time required to test all refocusing schemes also increased. For the 10% step size it took 3.89 hours of computation time with 12 CPU cores running in parallel to test all refocusing schemes for a single probe angle and slice orientation.

Table 4.2: Near-probe recovery for 2.5 mm nitinol needle with each scheme optimization technique of 10% step size. A recovery percentage of 100% means every voxel in the ROI was recovered above the threshold. The maximum average tSNR achievable was 0.079.

Probe Size	Angle w.r.t. B_0	Slice Direction	Master		LUT	
			Recovery	Avg. tSNR	Recovery	Avg. tSNR
2.5 mm	0°	$\perp$	95%	0.050	98%	0.046
		$\parallel$	88%	0.043	92%	0.040
	90°	$\perp$	80%	0.053	91%	0.041
		$\parallel$	64%	0.034	90%	0.030

4.4 Discussion

4.4.1 Summary of Results

This work developed and optimized a multiple echo Z-shim sequence to improve temperature mapping near metallic ablation probes. An MR image simulator was created and validated to allow the sequence to be optimized in simulation prior to acquisition on the scanner. The simulator takes an arbitrary 3D distribution of magnetic susceptibility values and computed the off-resonance map resulting from that distribution. Slice selection and

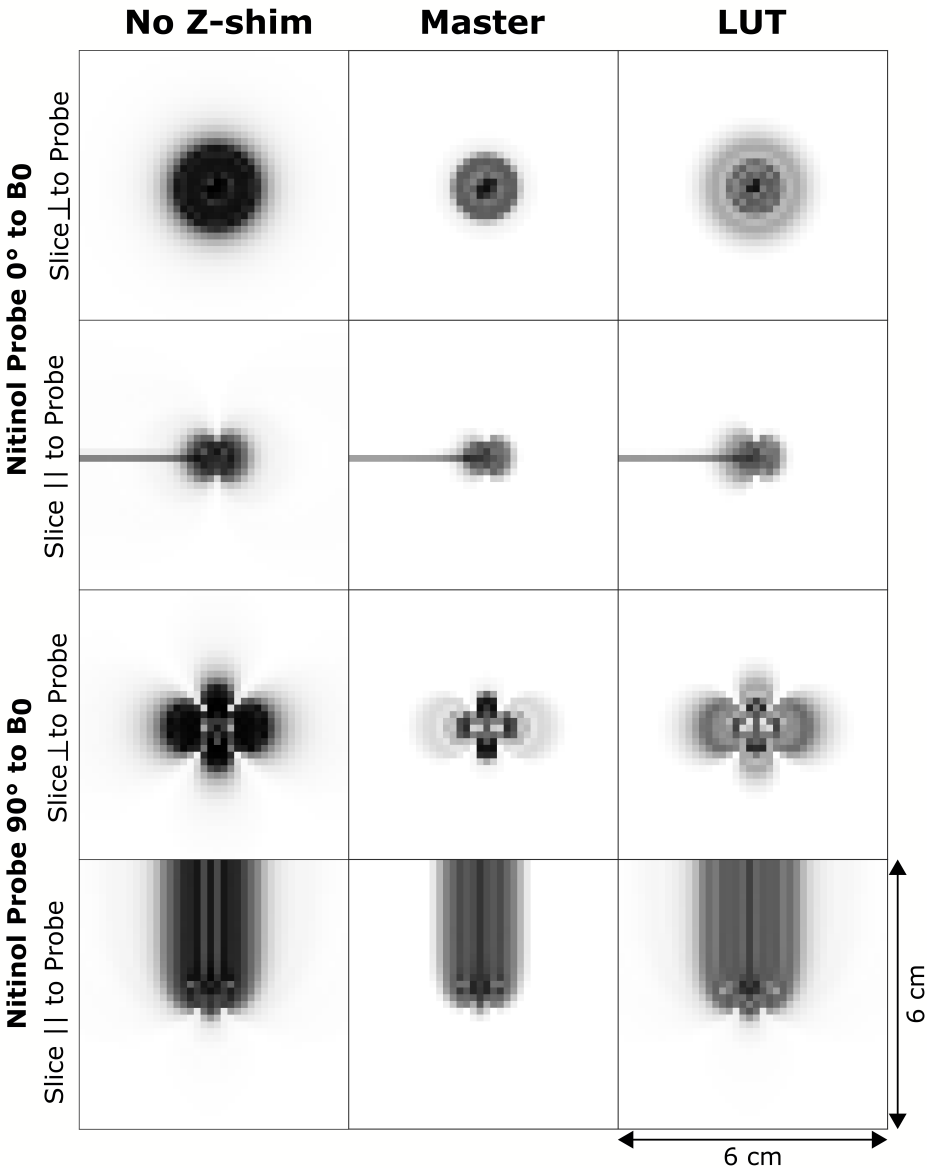

Figure 4.12: Scheme optimization comparison between the master and LUT for 2.5 mm wire with 10% step size. (left) tSNR with a conventional, single-echo scan with no Z-shimming. (middle) RSS tSNR recovered with the master scheme. (right) RSS tSNR recovered with the LUT schemes. With the 2.5 mm wire, the master and LUT schemes perform similarly and recover the lost signal regardless of probe angle and slice orientation. The non-uniform recovery seen in Figure 4.7 is corrected in this case.

refocusing is then applied to generate an image with or without Z-shimming. An exhaustive search algorithm was used to find the Z-shim refocusing scheme that best recovered near-probe temperature SNR, regardless of probe angle and slice orientation. The optimization

need be performed only once for a given ablation probe size. For a 1 mm nitinol RF ablation probe at 3T, the optimal refocusing scheme was found to be p_n = [200, 20, 180, 60, 140, 100]% (equivalent to gradient areas of [51.20, -46.08, 40.96, -30.72, 20.48, -10.24] $\frac{mT \cdot s}{m}$). The scheme increased near-probe tSNR signal when compared to a conventional, fully refocused single echo sequence. In a no-heat scenario this sequence reduced near-probe temperature deviation from 1.95°C to 0.93°C on average. During heating, the sequence increased the number of near-probe voxels containing reliable temperature measures by 225% on average.

4.4.2 Master vs LUT Scheme

Two methods were explored in this work for choosing the optimal refocusing scheme. The master scheme was an orientation-independent scheme designed to maximize near-probe signal recovery regardless of probe and slice orientation while the LUT was optimized for each probe and slice orientation individually. In simulation, the LUT increased the number of near-probe voxels recovered when compared to the master scheme but maintained the same average tSNR across the region of interest as the master scheme. In order to implement the LUT during a live treatment scenario a probe tracking algorithm would need to be implemented and the optimal scheme interpolated between LUT entries. Probe orientation could be derived from spin echo images or a proven tracking algorithm [126] but could add unwanted complexity to an ablation procedure. In practice, the tSNR maps created with both the master scheme and LUT were qualitatively similar, suggesting that the master scheme may be sufficient for a simplified treatment scenario. The use of a master refocusing scheme inherently allows the Z-shim sequence to be optimized only once and function adequately regardless of the orientation of the probe. This is particularly advantageous for applications where the ablation probe is non-linear, such as when tines are inserted in a starburst pattern from an RF ablation probe to increase ablation zone coverage. This could also be useful in guidance of novel transforamenal hippocampal ablation, where helical concentric tube needles are designed to match a patient's hippocampus shape and are inserted robotically. The

master scheme could provide an orientation-independent Z-shimmed sequence that recovers signal around the entire device and is not restricted to areas of the device lying in a certain plane.

4.4.3 Refocusing Step Size

For the 1 mm probe, a 20% step size in refocusing scheme generation was deemed sufficient. However, for the larger 2.5 mm wire, inhomogenities in recovery were seen with this step size. The smaller step size (10%) mitigated some of this inhomogeneity but did not substantially improve the number of voxels recovered with the master scheme. The LUT scheme with smaller step size did increase the number of voxels recovered at a small cost to average tSNR. This suggests that for a larger diameter probe, a 10% step size with LUT approach might be needed. This requirement of a finer sampling size increased the number of schemes that had to be tested in simulation. This increased computation time from 13.8 minutes for a 20% step size to 3.89 hours per probe angle and slice orientation for a 10% step size. Since this optimization is performed offline in simulation and need only be performed once per probe geometry, the increased computation is not prohibitive of using the 10% step size in practice. This trade-off suggests that probe size as well as computation constraints should be taken into account when performing optimization for this multi-echo Z-shimmed sequence. The exploration of the relationship between probe size, step size, and temperature precision is a topic for future work.

4.4.4 Alternative Scoring Metrics

The root sum of squares temperature SNR was used as an indicator of temperature precision in this work to score the performance of each refocusing scheme. Scores for each refocusing scheme were determined by maximizing the number of near-probe voxels that showed tSNR above a threshold. This method inherently scores gradient schemes that recover more voxels higher than schemes that recover less voxels, regardless of the trend in average

tSNR in the near-probe region. In order to maximize both the number of recovered voxels and tSNR value simultaneously, a Monte Carlo simulation method could be used to directly simulate heating on images simulated with each Z-shimmed sequence. This could provide a direct prediction of temperature precision to evaluate the performance of a given refocusing scheme, at the cost of substantially increased computation time.

4.4.5 Potential Limitations

The Z-shim gradients are inherently limited by the gradient characteristics of the scanner being used. Thus, an upper limit exists on the amount of refocusing that can be applied and strength of off-resonance that can be recovered. This limit was not reached in this work where the ablation probes were small and induced off-resonance on the order of 1 kHz or less. However, for larger metallic objects such as implants, off-resonance can be greater than 4 kHz [65]. Due to this limitation, the multi-echo Z-shim may be best suited to small metallic objects such as ablation probes, catheters [76], and biopsy needles [68]. Additionally, Z-shimming corrects through-plane dephasing but does not account for in-plane effects. In this work, a high read-out bandwidth was used to minimize in-plane dephasing and the effect was assumed to be negligible.

4.5 Conclusions

The proposed multi-echo optimized Z-shim sequence improved near-probe signal recovery and temperature precision over the conventional thermometry sequence. The validated simulation tool allowed the Z-shim to be optimized entirely prior to acquiring any images on the scanner and did not requiring tuning to each probe angle or slice orientation. This method could be useful for improving MR thermometry guidance of thermal therapies that use metallic ablators.

4.6 Availability of data and materials

Upon submission of the journal article detailing this work, the MR simulator and optimization code will be made available open-source at
https://github.com/poormanme/multiEchoZShim.

4.7 Acknowledgments

The author acknowledges Yue Chen, Robert Webster III, and Eric Barth for their experimental support. This work was supported by NIH Grants R21NS091735 and T32EB021937.

Chapter 5

OPEN-SOURCE, SMALL-ANIMAL MAGNETIC RESONANCE-GUIDED FOCUSED ULTRASOUND SYSTEM

5.1 Introduction

MR-guided focused ultrasound or high intensity focused ultrasound (MRgFUS/MRgHIFU) is a noninvasive therapeutic modality with many potential applications. However, the large financial costs involved in developing preclinical MRgFUS systems can be a barrier to research groups interested in developing new techniques and applications. This chapter details a validated, open-source preclinical MRgFUS system capable of delivering thermal and mechanical FUS in a quantifiable and repeatable manner under real-time MRI guidance. The goal is to enable early-stage MRgFUS researchers to build their own systems with minimal new design and software development effort. A hardware and software package was developed that includes closed-loop feedback controlled thermometry code and CAD drawings for a therapy table designed for a preclinical MRI scanner. For thermal treatments the modular software uses a proportional integral derivative controller to maintain a precise focal temperature rise in the target given input from MR phase images obtained concurrently. The delivery table holds the FUS transducer, a small animal and its monitoring equipment, and a transmit/receive RF coil. The transducer is driven by a waveform generator and amplifier controlled by real-time software in Matlab. The system was validated in tissue-mimicking phantoms and *in vivo* during murine tumor hyperthermia treatments. MR thermometry was validated with an optical temperature probe and focus visualization was achieved with acoustic radiation force imaging. The system provides a baseline functionality for performing MRgFUS treatments with inherent flexibility in a modular code structure and freely editable hardware design that can be refashioned for many applications. The disseminated package comprises hardware schematics and MR temperature mapping and FUS control

software with closed-loop feedback that enables real-time monitoring of the treatment with MR thermometry. Detailed start-up instructions and commented source code, along with access to sample data sets, make setting up the system straightforward while also leaving room for more sophisticated modifications in the future. The system's open-sourced nature will increase the availability of low-cost small-animal systems to interdisciplinary researchers seeking to develop new MRgFUS applications and technology.

5.2 Methods

5.2.1 System Overview

All schematics and code required to construct this system are available for download on GitHub [127]. Figure 5.1 gives a functional overview of the system. It comprises Matlab-based software (MathWorks Inc., Natick, MA) that runs on the MR scanner host PC and a custom thermotherapy delivery table, built to hold a commercially available FUS transducer within the magnet bore along with associated animal monitoring equipment. Treatment planning involves conventional MR imaging to localize the target tissue above the transducer and parametric analysis of tissue properties. During treatment an MR thermometry sequence is run continuously and images are read into Matlab in real-time from the scanner file system. MR image phase differences are used to calculate temperature maps within the target tissue and focal temperature is used as input to a proportional integral derivative (PID) controller. The controller computes the required transducer driving voltage to achieve a specified temperature rise in the target tissue based on the temperature evolution over time. The controller output is sent as a command over an Ethernet TCP/IP connection to a function generator and amplifier connected to the FUS transducer, enabling adjustment of sonication intensity in real-time. These components are detailed further in the following sections. The provided distribution includes all control software modules as well as Solidworks (Dassault Systèmes, Waltham, MA, USA) drawings of the delivery table and a parts

list of purchased commercial components.

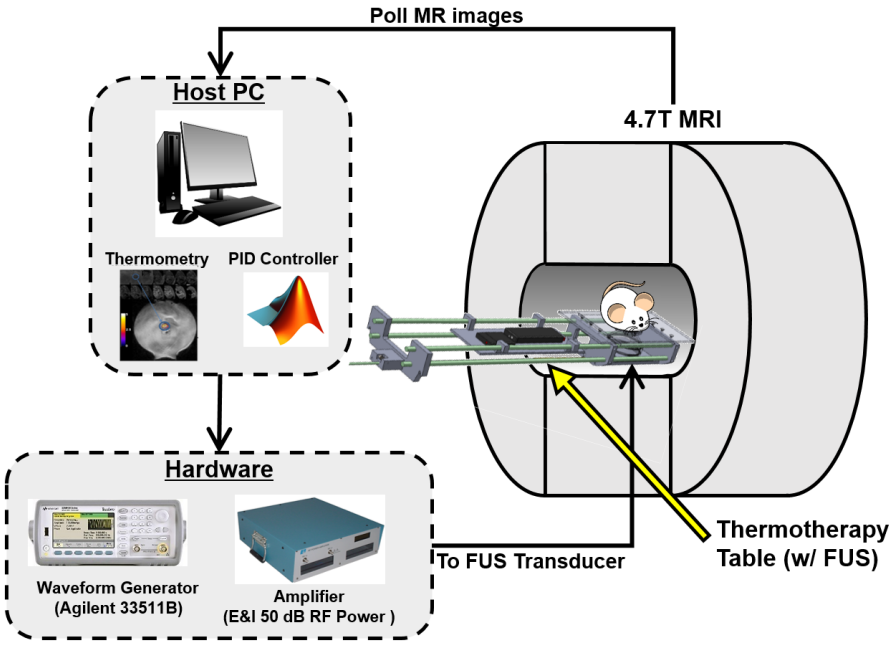

Figure 5.1: Open-source small-animal MRgFUS system overview. The delivery table holds the target and transducer at magnet isocenter while imaging is performed. Therapy control software for planning and closed-loop temperature control is implemented in Matlab on the MRI scanner's host PC, which collects the real-time MR images, computes the focal temperature, and modulates the ultrasound output accordingly.

5.2.2 Hardware

Thermotherapy delivery table: The therapy delivery table comprises an MR-compatible machined Plexiglas fixture with tray and handle that is designed to place the FUS transducer within isocenter for a 21 cm gradient set (Figure 5.2). The FUS transducer is secured in place within the head of the delivery table by placing it in a cylindrical slot sized to match its base. Once mounted within the table, the transducer is mechanically positioned using a series of gears. This allows for translation with two degrees of freedom (up to 3.5 cm axial to the magnet's bore with a rack and pinion and 2 cm in the B0 direction with a lead screw in 1 mm steps) without removing the setup from the magnet bore. Plastic shims can be inserted underneath the transducer to adjust the height of the transducer relative to the platform.

Different height coupling cones can be used to adjust the depth of focus. The cone of the transducer is positioned below a 4 cm × 2.5 cm delivery window opening in the platform above it, allowing it direct access to the sample. The delivery window insert can be swapped with windows of varying size and shape depending on the target geometry. An acoustically transparent membrane such as a polymer film can also be stretched over the opening in the platform provided that coupling to the transducer is maintained, though in this work an open window was found to provide the best coupling and freedom of movement of the transducer. The animal platform measures 15 cm × 28 cm which is large enough to hold a phantom or rodent, associated monitoring equipment, warming pad, anesthesia tube, and RF coil. An imaging RF coil of any configuration can be used and mounted to the platform so long as it does not lie in the path of the ultrasound beam. Holes for FUS power cable routing are integrated in the table and slots on the end plate are provided for securing the table handle to the front plate of the magnet. A movable tray is attached to the handle of the delivery table to hold any equipment that does not fit on the platform.

MR Equipment: The therapy table was validated in a Varian 4.7 T preclinical scanner (Agilent, Santa Clara, CA, USA) with 21 cm bore gradient set (305/210, magnet depth (cm) /inner diameter (mm), Agilent, Santa Clara, CA, USA). All software ran on the scanner's host PC (Red Hat R5.8, 2.4 GHz Intel Xeon CPU, 12GB RAM). An in house-built 5 cm diameter Tx/Rx surface coil was used for all imaging, and was typically placed flat on the delivery platform between the sample and transducer at the level of the phantom-water interface.

Ultrasound equipment: An MR-compatible single element spherically focused ultrasound transducer (Sonic Concepts H101MR, Ellipsoidal full width half max (FWHM): 1.4 mm × 1.4 mm × 10 mm @ 1.1 MHz and 0.4 mm × 0.4 mm × 3.2 mm @ 3.68 MHz, 400W, Sonic Concepts, Bothell, WA, USA) was used for all validation experiments. The transducer measures 64 mm in diameter with a focal depth of 51.74 mm and was encased in a plastic cone with an open tip for acoustic coupling. Before treatments, the cone was filled with

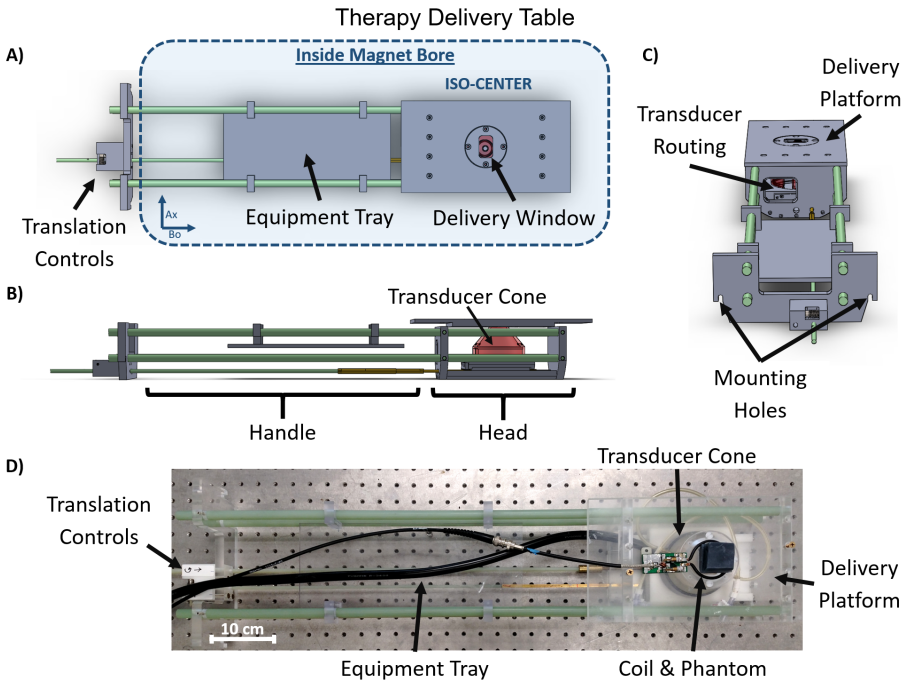

Figure 5.2: Detailed view of the delivery table. A) Top view showing placement inside magnet, positioning controls, and rectangular delivery window. B) Side view showing the housing of the FUS transducer and coupling cone. C) End view showing routing and mounting locations. D) Photo of the table to illustrate arrangement of coil and sample.

degassed water, the opening was covered with an acoustically transparent latex membrane, and ultrasound gel was applied to couple the cone tip to the sample. Compared to a water or oil-bath immersion approach, this configuration enables easier maintenance of animal core body temperature and the ability to visualize the top of the cone in the MR images for localizing the acoustic focus. The transducer cables extend outside the magnet bore and are connected to the matching network and subsequent amplifier via a BNC cable. The transducer is driven by an Agilent 33511B waveform generator (Agilent, Santa Clara, CA, USA) connected to an E&I RF power amplifier (E&I A150, 150 W, 55 dB, Electronics & Innovation, Ltd., Rochester, NY, USA). The waveform generator is connected via Ethernet to the same network as the MR scanner running the control software, to enable software control of the generator's output.

5.2.3 Software

The user interface and control software was implemented in Matlab and comprises two stages, 'Treatment Planning' and 'Real-time Temperature Monitoring and Control' (Figure 5.3). The code is modular so that elements can be tailored to a specific hardware setup and application while maintaining compatibility with the underlying architecture. These modules, including the function generator initialization, the PID controller, the thermal dose calculation, and data processing, are called from a master script that controls the entire sonication and reconstruction. An optional graphical user interface (GUI) is provided for straightforward treatment planning (Figure 5.4). The GUI allows for the user to draw focal and drift correction ROIs on a T_2-weighted anatomical image of the target as well as define a path to the acquisition file and function generator address, controller gains, set a thermal target, toggle drift correction and thermal dose calculations, and set a destination file for the computed temperature maps. These parameters can also be defined manually within the code without using the GUI. After initial setup, the user is prompted to start the thermometry sequence on the scanner and real-time temperature monitoring and control begins. During treatment, the focal temperature evolution and voltage output over time as well as the latest magnitude image and computed temperature map are displayed for online treatment monitoring.

Treatment Planning: A suite of MR scan protocols was developed for treatment planning, including anatomical T_1 and T_2 weighted scans, an MR acoustic radiation force imaging (MR-ARFI) scan for focus localization (detailed further below) [128], and a multiple gradient echo scan for water-fat separation (Table 5.1). An anatomic planning image (usually T_2-weighted) can be imported into the optional user interface to aid in thermometry ROI placement.

All scans except MR-ARFI were implemented as Varian protocols and did not require new sequence development. The MR-ARFI pulse sequence was implemented based on the Varian "gems" (gradient echo multislice) sequence to visualize the acoustic focus without

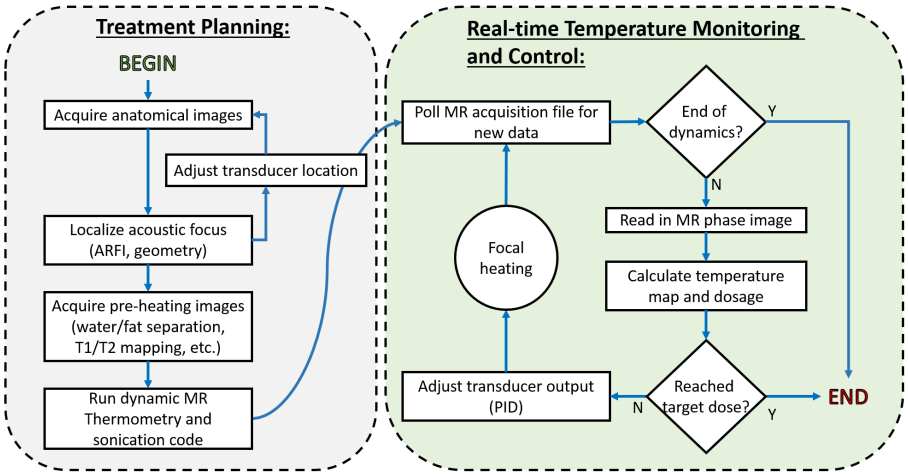

Figure 5.3: Software Flow Chart. The treatment protocol comprises a planning stage followed by real-time temperature monitoring and control. The software design allows anatomical and parametric imaging prior to sonication for treatment planning. The temperature monitoring control loop will adjust the FUS amplitude according to observed heating, automatically stopping treatment when a desired thermal dose is achieved.

inducing a significant thermal effect. The source code for the ARFI sequence is in the distributed package. A motion encoding gradient (MEG) was inserted into a gradient echo sequence immediately following the excitation pulse and prior to the encoding gradients [129]. The MEG parameters such as orientation, duration, shape, and strength are adjusted in the scanner interface to align with the specific geometry of the transducer and target; ARFI encoding is typically performed in the direction of acoustic propagation. The sequence generates a TTL pulse that triggers an ultrasound pulse during the second lobe of the bipolar MEG. Immediately following the MEG, a delay of 1 μs is inserted to prevent gradient overlap before continuing with the spatial encoding gradient waveform. The number of FUS cycles (and thus the length of the pulse) is set on the function generator such that FUS is applied for the duration of the gradient lobe. The sequence is run twice with opposite polarization of the MEG and the phases of the resulting two images are subtracted. The resulting difference is proportional to the tissue displacement caused by the ultrasound beam, according to:

$$\Delta x = \frac{\Delta\phi}{2\gamma G l} \tag{5.1}$$

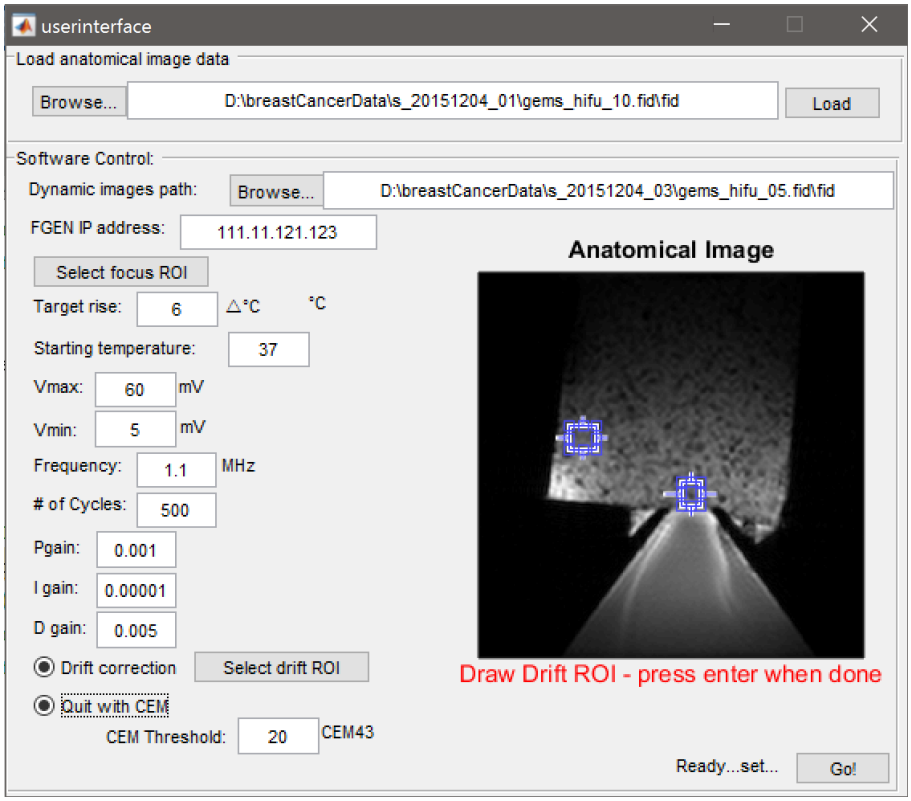

Figure 5.4: Optional GUI for setup of the control software. The user can draw ROIs on an anatomical image for the acoustic focus and drift control, set the ultrasound parameters, tune the control parameters, and define a thermal dose target.

where Δx is the displacement, $\Delta\phi$ is the phase difference between images with opposite gradients, γ is the gyromagnetic ratio, G is the MEG strength, and l is the length of the MEG. In this equation, the MEG was approximated by a rectangle since trapezoidal gradient pulses with sharp rises were used. The rise time of the MEG with the 21 cm bore 305/210 gradient set was 52 microseconds for the gradient characteristics used (Table 5.1), while a typical total MEG duration of 8 ms is used. Residual phase errors due to eddy currents were removed from the acquired ARFI images in post processing by subtracting the phase of two images acquired at each polarization with FUS on and off. Then the corrected images acquired with opposite polarization of the MEG were subtracted and scaled according to Equation 5.1 to obtain final displacement maps.

Table 5.1: MR imaging sequences and parameters

Sequence	Parameters	Purpose
gems	TE = 6-15 ms TR = 30 ms angle = 25 mat = 96x96 FOV = 60x60 mm	Gradient echo sequence for PRF-shift thermometry. All monitoring was conducted in a single slice in the MRI axial plane, parallel to the direction of acoustic propagation. 1-2 dummy scans were used to suppress steady state artifacts.
fsems	TE = 37 ms TR = 3000 ms ETL = 8 ESP = 9 ms angle = 20	Fast spin echo sequence for T_2-weighted anatomical imaging. Enables tumor localization and visualization of the surrounding environment.
mgems	TE = 2 ms ΔTE = 3ms TR = 30 ms angle = 25 mat = 96x96 FOV = 60x60 mm	Multi-echo gradient echo scan for water/fat separation in post-treatment analysis.
gems_meg	TE = 7.6 ms TR = 71 ms G_amp = 10 G/cm G_dur = 4 ms FUS = 1.1 MHz	Modified gradient echo sequence for ARFI. G_dur represents the duration a single lobe of the biopolar MEG. The direction of motion encoding was controlled within the scanner interface based on the slice orientation.

Real-time Temperature Monitoring and Control: Once all pre-treatment images are acquired and the treatment is planned, the real-time thermometry loop can be executed. This comprises the bulk of the software, informing the ultrasound output directly from images acquired simultaneously on the scanner. Single slice, baseline subtracted proton resonance frequency-shift thermometry was implemented using a gradient echo imaging sequence as described in Table 5.1 with a temporal resolution of 3 seconds. Scanner field drift correction is imperative for accurate MR thermometry, particularly during hyperthermia treatments where a long sonication time at low power is required [12, 130, 11, 131]. To address this, a drift correction routine was implemented using the phase shift in an ROI outside the heated

region as a reference. During *in vivo* sonications, ROI-based drift correction often required the addition of a small tube of water to the imaging plane to serve as a reference no-heat region in case the mouse anatomy was too small for a reliable ROI correction. Once the real-time monitoring loop is initialized, the software continuously polls the MR raw data file for new data. To prevent constant file opening and closing that could delay execution, the software only opens the file when the time-stamp has changed, meaning a new image has been acquired. One to two dummy scans are acquired prior to the first baseline to prevent steady state artifacts. Then, the first image acquired in the loop is used as a baseline and subsequent images are used to compute a temperature map relative to the baseline. A focal mean temperature is estimated from the current temperature map and stored. If desired, drift correction is applied at this step to account for scanner drift and thermal dose is computed in CEM43 units [5].

The corrected mean focal temperature along with the current function generator voltage V_{out} is then input to a PID controller function along with the desired temperature rise, the PID gain constants, the maximum voltage output limit, and the previous error up to the current dynamic. The function calculates the new V_{out} to achieve the desired temperature rise according to:

$$V_{out} = \min\Big\{K_p e(t) + K_i \int_0^t e(\tau)d\tau + K_d \frac{de}{dt}, V_{max}\Big\}, \tag{5.2}$$

where K_p, K_i, K_d are the proportional, integral, and derivative gain respectively, $e(\tau)$ is the error between the current temperature and desired temperature, and t is the time elapsed since starting sonication. The maximum voltage constraint V_{max} is set to maintain the acoustic pressure below the threshold for cavitation during *in vivo* experiments and minimize skin burns. It also prevents the transmitted power from damaging the transducer. A maximum voltage of 70 mV (prior to 55 dB amplification) was used for all *in vivo* experiments, corresponding to a peak negative pressure of approximately 1.5 MPa at 1.1 MHz as measured

by a ceramic needle hydrophone (HNC-0200, Onda, Sunnyvale, CA). PID gain values are critically important in controlling the behavior of the system and temperature rise at the focus. These gains were manually tuned in a graphite-agar phantom to prevent target temperature overshoot of greater than 1°C and a steady-state temperature variation of no more than 0.5°C. The resulting values were: $K_p = 10^{-3}$, $K_i = 10^{-5} s/repeat$, and $K_d = 5 \times 10^{-3} s$. Once calculated, V_{out} is returned to the real-time loop. The software then checks if the measured thermal dose is greater than the defined thermal dose threshold and sets the output to $V_{out} = 0$ if the threshold has been met, turning off the transducer output. The final V_{out} is then output to the function generator. If MR imaging is complete the loop exits and treatment is halted. Otherwise the loop repeats, modulating the transducer output to maintain a precise and accurate temperature rise within the target for the duration of scan time. In the event of a system failure, the code automatically exits and stops output from the function generator. All MR images were obtained with the parameters listed in Table 5.1.

5.2.4 Experiments

Fiber Optic Thermometry Validation: A graphite-agar phantom (1.5% agar, 4% graphite, weight per volume of water [132]) was used to mimic tissue acoustic properties. The phantom was set up on the system and coupled to the transducer cone with ultrasound gel. Prior to sonication, a fiber optic temperature probe (FISO Technologies Inc., Quebec, Canada) was inserted into the phantom just outside of the acoustic focus. The entire setup was placed in the magnet and closed-loop feedback sonication was performed for 20 minutes under thermal monitoring with a gradient echo thermometry sequence (Table 5.1). The imaging slice was 3 mm thick and oriented to avoid imaging artifacts due to the heating of the fiber optic probe tip. Probe placement relative to the focus and the location of the imaging slice are illustrated in Figure 5.5a. Given the uniformity of the phantom and radial symmetry of the acoustic focus, an ROI that was radially symmetric to the fiber optic probe tip's location

with respect to the focus was chosen within the imaging slice for the mean temperature calculation.

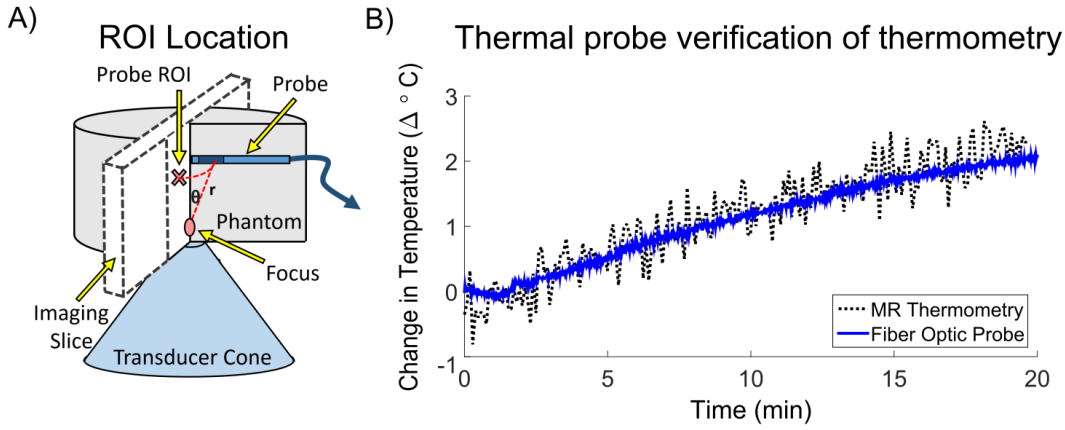

Figure 5.5: Fiber optic probe thermometry validation. A) Illustration of the experimental setup. To avoid artifacts and damage to the probe it was placed above the focus; B) plots probe temperature compared to MR temperature measurements in a 5.7 mm^2 ROI at a geometrically equivalent position within the slice.

Constant Temperature Control Validation: To validate the closed-loop control software, a graphite-agar phantom was again placed on the delivery platform, coupled to the transducer and placed within the magnet. Five sonications lasting 10 minutes each were conducted with the system at target temperature rises between 2°C and 10°C. A single 3 mm thick axial slice through the acoustic focus was used for thermal monitoring. The phantom was allowed to cool for 2 minutes between each sonication and PID gain values remained fixed throughout. For all closed-loop experiments, precision and accuracy measures of the temperature rise were calculated from the initial temperature rise, defined as the point at which the mean focal temperature first crossed the set temperature threshold.

Closed-loop Feedback at Two FUS Frequencies: Raw chicken and graphite-agar phantoms were used to validate the closed-loop feedback sonication at the transducer's two operating frequencies (1.1 MHz and 3.68 MHz). In each sonication, a single 3 mm thick axial slice through the acoustic focus was used for thermal monitoring and ROI-based drift correction was performed by placing an ROI in areas of the phantoms that would see negligible heating. The operating frequency was set using the control software and matching network connected

to the transducer.

In vivo Murine Tumor Treatment: The thermal monitoring and closed-loop feedback system was tested *in vivo* in a Polyoma PyVMT murine breast cancer tumor model [133] under an approved Institutional Animal Care and Use Committee protocol (M/13/010). This animal model spontaneously generates superficial tumors in the mammary fat pads with a progression comparable to human breast cancer. Tumors measuring ≤ 1 cm in diameter and located most distal to the lungs were chosen for targeting with FUS in order to minimize breathing artifacts. Fur in the treatment area was removed with depilatory cream prior to treatment for improved acoustic coupling. The animal breathing rate was maintained throughout around 60 breaths per minute with Isoflurane anesthesia ranging from 1.5% to 2.5%. The tumor was coupled to the transducer cone with ultrasound gel and core body temperature was maintained with a circulating hot water pad. Localized hyperthermia was applied with the control software under thermal monitoring in a 3mm thick axial slice through the focus at 1.1 MHz for 12 minutes. No drift correction was applied for this mouse although both a lookup table method, with precalculated drift compensation, and roi-based correction method have been used successfully with this system. The calculated focal temperature and PID controller output were observed to characterize the system behavior.

Transducer Translation Validation: The system was used to deliver four ablative sonications to a polyacrylamide gel phantom containing egg white [134]. The phantom was designed to be translucent except in areas of heating where the egg white would coagulate. Ablative treatments were manually applied for 2 minutes at a peak negative pressure of 3.9 MPa, without temperature feedback. Between sonications the transducer was translated in the slice plane using the translation controls outside of the magnet and positioning was confirmed with T_1-weighted images visualizing the water-filled transducer cone and the sample. After all sonications were completed, a T_2-weighted image was acquired and a photograph was taken of the coagulated egg-white lesions visible in the phantom. The distances between the lesions were calculated using both images and compared to assess relative position

accuracy.

Mechanical Displacement with ARFI: MR-ARFI measurements were made in a tofu phantom that was coupled to a short transducer cone to increase the penetration depth of the transducer and enable visualization of the near and far fields of the focus within the phantom. ARFI images were acquired in an axial and coronal slice centered around the acoustic focus at 1.1 MHz with a 2.5 MPa peak negative pressure (5.6% duty cycle). Optimal coronal slice placement was determined by acquiring ARFI images across the entire phantom and choosing the slice of most localized displacement, indicating a position at the focus. Axial placement was confirmed by centering the slice over the transducer water cone visible in the anatomical images. For each slice orientation, the motion encoding gradients were oriented in the direction of acoustic propagation.

5.3 Results

5.3.1 Fiber Optic Thermometry Validation

Figure 5.5b shows a comparison of the temperature measured during sonication with MR thermometry and the fiber optic probe. The mean temperature recorded with MR thermometry in the 5.7 mm^2 equivalent ROI was accurate relative to the thermal probe with an RMSE over time of 0.07°C and maximum error less than 1°C. The thermometry measurements were noisier than the probe measurements but had an acceptable level of precision with a standard error of 0.25°C.

5.3.2 System Behavior at Varied Target Temperatures

For all sonications, no lag in software execution was observed. The control software run on the scanner computer executed fully within the 3 second time frame of each image as detailed in Table 5.2. Figure 5.6 plots the mean focal temperature in a phantom subjected to multiple sonications at set points ranging from 2°C to 10°C. The focal ROI used to calculate

the mean temperature was 2.6 mm × 3.2 mm which encompasses the full width half max of the transducer's focus. In each case the temperature reached a steady state around the desired temperature within a few minutes, with an initial overshoot of less than 1°C except for the 10°C sonication which had an initial overshoot less than 1.5°C. After the initial temperature rise, the mean standard deviation of the temperature error was 0.28°C with a mean RMSE of 0.44°C.

Table 5.2: Execution speed of the real-time software

Action	**Mean Execution Time (ms)**	**Purpose**
Initialize Function Generator	1885 ms	Performed once before each temperature-controlled sonication, this action opens communication between the host PC and the ultrasound function generator, and configures the function generator with the desired output parameters for sonication.
Read in Image	42 ms	Time to open the raw MR data (.fid) file and reconstruct the magnitude and phase data into an image for thermometry.
Compute Temperature Map	39 ms	Time to construct a temperature map with baseline subtraction of image phases after new data has been read. This timing includes drift correction with subtraction of phase from a reference ROI.
Output Voltage to Function Generator	1 ms	Time to evaluate PID equation based on current focal temperature and system state, and send V_{out} to the function generator.

5.3.3 Closed-loop Feedback at Two FUS Frequencies

Figure 5.7 shows the sonication of two phantoms at 1.1 (A) and 3.68 (B) MHz FUS frequencies. The left side of the figure shows representative treatment temperature maps overlaid on a T_1-weighted image of the phantom (the baseline thermometry image). The right side plots the mean focal temperature over time as measured by MR thermometry and

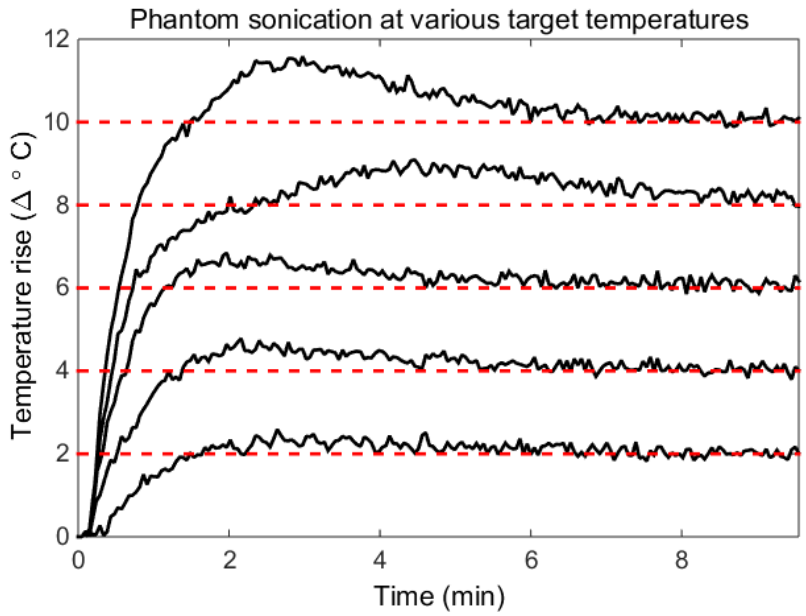

Figure 5.6: Sonications across temperature set points. After initial overshoots that did not exceed 1.5°C of the set points (dashed red lines), focal temperature was maintained for 10 minutes with a mean standard deviation of the temperature error of 0.28°C and a mean RMSE of 0.3°C.

the commanded function generator voltage V_{out}. Focal ROIs used for the mean temperature calculation were 2.6 mm × 3.2 mm at 1.1 MHz and 2.6 mm × 2.6 mm at 3.68 MHz. The ROIs used for drift correction are also displayed in the figure and were each 4.6 mm × 4.6 mm. Temperature overshoot in each case was less than 1°C with the standard deviations of the errors measured to be 0.21°C and 0.43°C at 1.1 and 3.68 MHz, respectively. After the initial overshoot, the RMSE of the mean temperature measured was 0.31°C for the 1.1 MHz sonication and 0.61°C for the 3.68 MHz sonication. A steady state was achieved within a few minutes, as noted by the leveling off in the voltage output over time.

5.3.4 *In vivo* Murine Tumor Treatment

Figure 5.8 shows an *in vivo* sonication of a murine mammary tumor treated at Δ 6°C for approximately 12 minutes. On the left, a representative temperature map during treatment is overlaid onto a T_2-weighted anatomical image of the mouse. The focal ROI size was 2.5

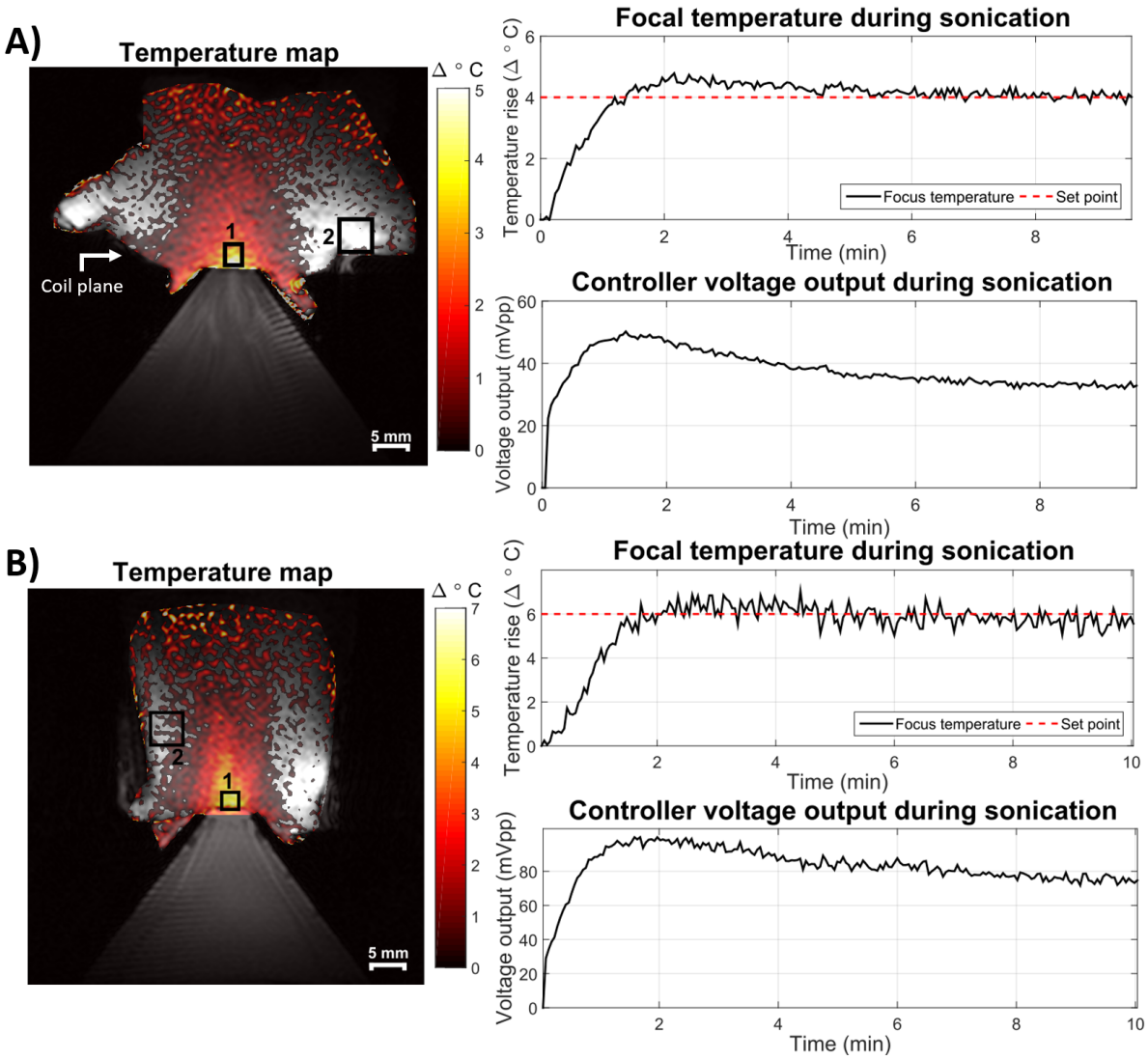

Figure 5.7: Sonications at 1.1 (A) and 3.68 (B) MHz FUS frequencies, targeting temperature set points in ROI 1 for ten minutes. Background phase drifts were corrected using an ROI outside of the area of heating (ROI 2). Controller voltage is also plotted for each case and also stabilizes after an initial rise and small overshoot. The white arrow indicates surface coil placement. Low temperature SNR at the top of the phantoms (and far from the surface coil which sat at the level of the water-phantom interface) contributed to the apparent elevated temperatures there but did not interfere with the focus measurements. Stripe artifacts in the water cone are likely due to Moire fringes caused by poor field homogeneity in the water bath near the transducer causing aliasing.

mm × 2.5 mm. The two curves on the right show the mean focal temperature evolution over time and the corresponding peak-to-peak voltage output from the PID controller to the transducer. After an initial overshoot of less than 1.5°C, the focal temperature reached

a steady state (noted again by the leveling off of the voltage output with time) with some variations. Three major dips in the mean temperature reading and subsequent bumps in the voltage output occur around 4, 7, and 10 minutes as noted by the red arrows in the figure. These perturbations corresponded with times when the mouse started breathing at a faster rate as observed by the monitoring equipment. The PID controller responded appropriately by increasing the voltage output when a sudden decrease in temperature was observed. The controller was able to compensate for the change in conditions and maintain the temperature at the set point with a 0.49°C standard deviation of the error and 0.53°C RMSE after the initial temperature rise.

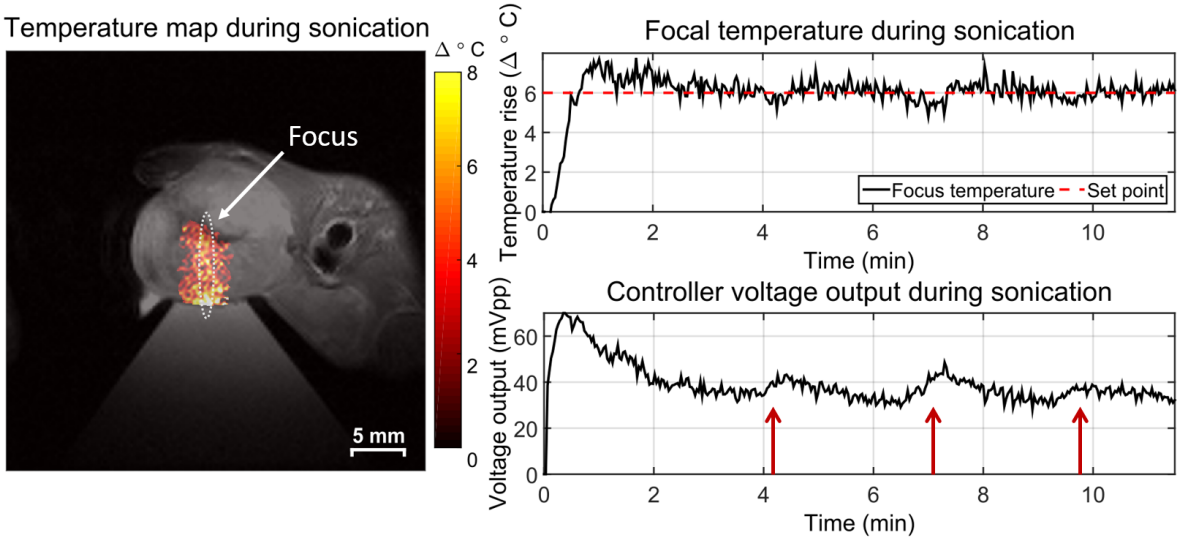

Figure 5.8: Sustained local hyperthermia in a murine mammary tumor for 12 minutes. Sustained, long-term sonication was achieved with minimal overshoot, a 0.49°C standard deviation of the error, and 0.56°C RMSE after the initial temperature rise. The PID controller responded to sudden changes in focal temperature as indicated by the red arrows. The 1.4 mm by 10 mm contour of the transducer focus is indicated by the white oval.

5.3.5 Transducer Translation

Figure 5.9 shows a T_2-weighted image and photograph after four ablative sonications were performed in an acrylamide-albumin phantom. No removal of the setup from the magnet was required to move the transducer. The ablated lesions are clearly visible on the T_2-weighted

image and qualitatively line up well with the coagulated egg white lesions visible in the photograph. The mean error in the distance between lesions in the two images was found to be 0.11 mm demonstrating good relative positioning accuracy.

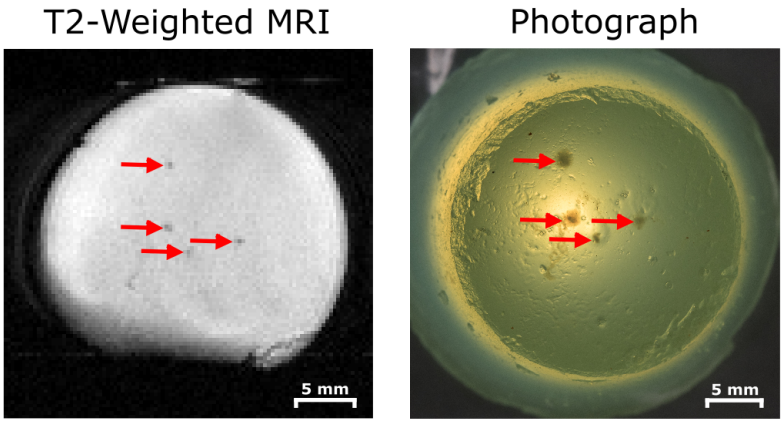

Figure 5.9: Demonstration of transducer translation capabilities via multiple egg-white phantom ablations. The transducer was moved using the controls outside of the magnet; no re-positioning of the phantom or removal of the platform was necessary. Lesions were visible on a T_2-weighted image (left) and on photographs taken outside the magnet (right), and matched geometrically.

5.3.6 Mechanical Displacement with ARFI

Figure 5.10 shows the axial and coronal displacement of the tofu phantom with applied FUS as imaged with the ARFI sequence. The displacement maps were overlaid on T_1-weighted magnitude images for visualization. The measured displacement was consistent between slice orientations, with maximum displacements of 1.0 μm (axial) and 1.2 μm (coronal). The FWHM for the axial and coronal maps were 3.0 mm and 2.93 mm respectively, which are comparable to the 1.4 mm FWHM intensity profile of the transducer, but may be broader in this measurement due to phantom mechanical properties and shear waves.

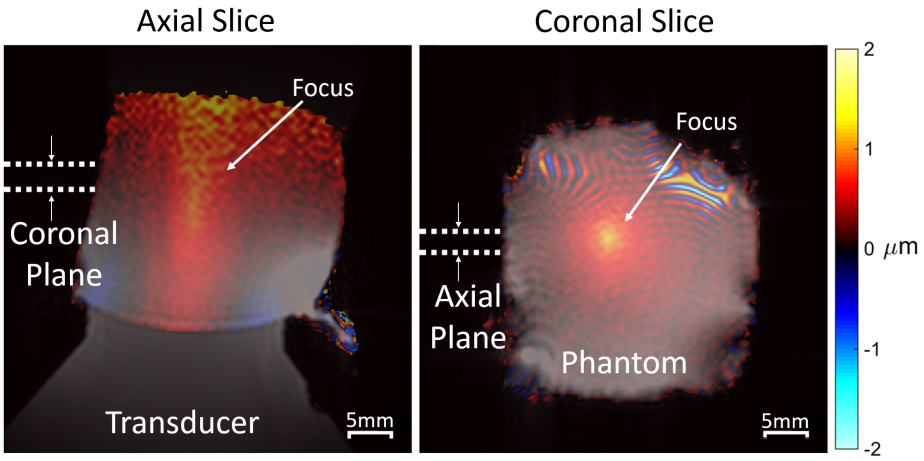

Figure 5.10: ARFI-measured displacement in the axial and coronal directions overlaid on T_1-weighted images of a tofu phantom. Localized displacements are apparent at the focus while while smoother displacements appear throughout which may correspond to shear waves. The focal displacement location and size correspond well to the expected geometry of the transducer. Acoustic reflections with the air boundary and lower SNR near the top of the phantom likely contribute to the diffuse rise in displacement there. Moire fringes are visible at the top of the coronal image, which are likely due to field inhomogeneity near the surface of the transducer causing some water bath signals to be excited and alias into the image.

5.4 Discussion

5.4.1 Summary of Results

We have successfully designed, constructed, and tested an open-source preclinical MRgFUS hardware and software package in phantoms and *in vivo*. The system was shown to be capable of robustly sustaining controlled temperature rises with MRgFUS in a preclinical setting. The platform is MRI compatible, allowing for unobstructed imaging and sonication of the target with two degrees of freedom in transducer motion and minimal removal of the hardware once placed. Treatment planning tools were implemented, comprising standard anatomical scans and an MR-ARFI sequence to image mechanical displacement due to FUS. The real-time temperature mapping and drift correction routine was shown to be accurate to within 0.07°C when compared to a fiber optic thermal probe reference and was able to complete computations online within one image frame. The use of a 3mm slice thickness

during thermometry, which was larger than the focus width and chosen to increase image SNR, could contribute to initial temperature underestimation within the focus [135]. However, with the long sonication duration and thermal diffusion in hyperthermia, we do not expect this to be a problem. For shorter treatments such as ablations, users should choose their slice thickness accordingly to prevent underestimation. A steady state was achieved for all sonications during which the PID control software responded appropriately to changing conditions *in vivo* and maintained the desired temperature rise for the entire duration of treatment. These characteristics make the described system viable for use in studies with MRgFUS on small animal models.

We expect minimal training to be necessary for new users. Two undergraduate researchers in our group learned to setup and run the system with 5 hours of training. The entire system was constructed for less than $20,000 USD of which approximately $600 USD was spent designing and constructing the delivery table. Many of the commercially purchased products, such as the amplifier, were intentionally purchased with specifications far exceeding those required for this system. Further reduction of cost could be achieved depending on the hardware specifications required by the application and preexisting availability of such equipment to the user.

5.4.2 Steady-State with PID Control

The implemented PID controller allowed the system to robustly maintain the focal temperature rise at a desired set point without any visible effect from the scanner's field drift or transducer frequency used. The controller was responsive to changes in perfusion during *in vivo* heating [136], as evidenced by upticks in the the output voltage in Figure 5.8, however proper tuning of the PID controller gains is important for controlling the response of the system in such situations. The PID controller performance has been shown previously to be robust to noise [137], however adjusting the integral gain of the controller might also improve noise stability [138]. For this study the PID parameters were tuned once manually in

a tissue-mimicking phantom and remained constant during all experiments described. This approach was sufficient for our purposes as the temperature set points and tissue properties did not vary significantly between experiments. This may also be the case for many hyperthermic applications where a set point of $\Delta 6$°C from baseline (or 43°C) is desired and does not vary significantly between experiments. Individual tuning may also be avoided for studies that target tissues with similar properties between subjects. These settings have been used successfully in 4 more mice with no observed disruption from the PID controller settings [139]. However, if a study were to involve more heterogeneous tissue or largely varied target temperature rises, the controller gains would likely need to be tuned for each specific tissue and set point. Controller gains would likely also be required for different applications, such as hyperthermia vs ablation where overshoot of the target could severely impact the experimental outcome. In these cases, the user could alter the PID controller's behavior by adjusting the PID gain values. For example, the early temperature overshoot we observed in some of our sonications could be reduced by increasing the derivative gain with a potential trade off of a slower start-up. These values can be freely adjusted by the user within the GUI or software code to tune the controller output. Tuning could be performed using previously-described algorithms [140, 141].

5.4.3 Temporal resolution

For real-time monitoring a fine temporal resolution is desirable to maintain tight control of heating and rapidly detect unintended heating [12]. In addition to MR acquisition time, another main factor that could limit the temporal resolution of this system is the execution speed of the real-time software. This is highly dependent on the computer specifications, however care was taken in the code development to minimize execution time. For example, memory is preallocated for large variables and the MR raw data file is opened only when the time stamp on the data has changed from the previous check. This prevents the file from being continually opened and closed extraneously, avoiding any associated lag time.

For the software run on the scanner computer, execution speeds were as detailed in Table 5.2. The software executed in less than a second after the inital setup which is shorter than the thermometry sequence's temporal resolution of 3 seconds with no observed delay in temperature mapping. In the case that a shorter temporal resolution were needed an accelerated image acquisition scheme such as EPI [116] or partial Fourier [142] could be implemented. The operation of the system should remain the same provided that the software execution time does not exceed the time required to acquire the next image.

5.4.4 Contemporary Systems

Other research groups have also developed systems to meet the challenge of treating small animal models with MRgFUS, yet there are underlying differences that make our system unique. One such system was recently described by Bing et al [143], which was also based on a constrained PID controller for fine control over the focal temperature rise *in vivo*. The Bing system was designed for a 3T human MRI scanner and based on a commercial clinical MRgFUS system (RK100, FUS Instruments, Toronto, Canada), which are of more limited availability and much higher cost than the described system. Our system was intended for use with small-animal MRI scanners more commonly used in preclinical research and has the flexibility with open-source CAD plans to be adapted to use with scanners of many configurations. Many of the current hardware components were machined by hand but could be 3D printed provided that the material used was strong enough to remain structurally sound with use. An interesting development in Ref. [143] was the use of acoustic lenses to diffuse the focus and deliver heat over a larger volume. For the mouse model used in our experiments the 1.4×10 mm focal size of our transducer at 1.1 MHz was sufficient, however other applications could benefit from larger focal sizes enabled by such lenses. In this case it would be possible to adapt the transducer cone used with our system to include an acoustic lens.

Another contemporary system was described by Fite et al. [140]. In their system, MRg-

FUS was also implemented on a preclinical MRI scanner, however commercial hardware was used to equip the magnet with FUS capabilities (Thermoguide, Image Guided Therapy, Pessac, France) leading to cost and design flexibility limitations similar to Bing et al. The Fite system used a PID controller tuning algorithm using the Pennes Bioheat Equation [144] that enabled exact control characteristics to be easily achieved. As mentioned previously, such tuning algorithms could be integrated with our system to avoid manual tuning of the PID controller. One feature of the Fite system is the integrated quadrature coil that provides high sensitivity throughout the target volume during treatment. Our system uses a surface coil which provides high sensitivity at the focus level but has less sensitivity further into the volume. This sensitivity gradient does not interfere with temperature visualization in our system, however image SNR could be further improved by adaptation of a quadrature coil similar to the Fite system. We found that our temperature measurements were accurate to within 0.07 °C, and precise with a standard error of 0.25 °C, which is comparable that of the commercial system used by Fite et. al. (Ref. [140], Figure 4) as well as clinical systems such as the Philips Sonalleve (Philips Healthcare, Best, Netherlands), for which an accuracy within ±1 °C is reported [145].

An additional system was described by Magnin et al. [146]. Like our system and the Fite system, the Magnin system was designed for a preclinical MRI scanner. However, the FUS control software used by Magnin was commercially purchased (Thermoguide, Image Guided Therapy, Pessac, France). The main feature that sets their implementation apart is the use of a motorized frame to adjust the transducer position. The Magnin system allows for translation in 3 dimensions as well as electronic steering with multiple transducer elements while ours has 2 degrees of freedom and uses a single element transducer. This freedom of motion works very well for their proposed application in transcranial FUS. It should be noted that the transducer used in the Magnin system was much smaller than the one implemented with our system. As such, the exact motorized framework used by Magnin may not be usable with our larger transducer size, although a similar motorized design could be adapted. For

the hyperthermic application explored in this paper, our system's translation and steering capabilities were sufficient.

Finally, while our system's most fundamental features such as treatment planning and monitoring software, real-time MR thermometry-based closed-loop temperature control, and an MR-compatible therapy table parallel the features of a clinical MRgFUS system, current clinical systems now include more sophisticated features such as active transducer cooling, active skin cooling, and electronic and mechanical beam steering. While our system does not currently have these features, the underlying framework is comparable and inherently allows for more flexibility of design and application-specific modification than a more regulated clinical system might provide.

5.4.5 Possible Extensions

The open-source nature of the system allows it to be adapted to the specific equipment requirements of the group using the system. The current delivery platform with flat top and modular delivery window provides inherent flexibility in target placement, however this can make experimental setup challenging. During experiments, positioning the coil for good SNR while not interfering with the acoustic coupling, the circulating water heating pad (Kent Scientific, Torrington, CT, USA), or the animal monitoring equipment required the use of tape and foam supports. These considerations led to relatively long setup times, particularly for *in vivo* experiments where it often took up to 25 minutes to position the mouse, tune and match the coil, and calibrate the MR scanner for imaging. Such challenges could be mitigated by the use of a mouse holder that screws into the platform, provides mechanical support, connects to anesthesia and monitoring equipment, and maintains body temperature. In addition, the current single-slice baseline subtracted thermometry routine was prone to susceptibility artifacts from gut motion, respiration, or the presence of fat depending on the imaging slice. This could be improved through the implementation of more motion-robust temperature reconstruction, which is an open area of research [147, 148, 149, 150, 14, 151, 13,

36, 152, 153, 15, 154]; given an effective approach to this problem, the associated processing could be incorporated in our modular processing framework. Additional modules could be added by the user to incorporate other feedback modes (ie: concurrent ARFI imaging, passive cavitation detection) as well as making the required MR pulse sequence or hardware changes. Hardware modifications can be made in the provided Solidworks designs prior to construction. For example, the delivery table could be modified to hold transducers of other geometries by changing the size or shape of the cylindrical slot within the head of the table that holds the transducer. The length, width, and height of the delivery table could be adjusted to accomodate MR scanners of different bore sizes provided that the ultrasound transducer still fits within the table. If the addition of plastic shims does not provide enough freedom of adjustment in the transducer height, a second rack and pinion system could be constructed to allow the transducer to be raised and lowered relatively to the platform from outside of the magnet. The open-source files and modular structure of the software is intended to make such adaptations straightforward for users to implement.

5.5 Conclusions

We have described and validated a preclinical closed-loop MRgFUS system. Defined completely in open-source Matlab and Solidworks files, we hope to lower the initial barrier to conducting small-animal MRgFUS studies. The described system represents a cost-effective solution that allows for flexibility in design and implementation to suit the needs of cross-disciplinary researchers in conducting preclinical studies with FUS.

5.6 Availability of data and materials

The datasets supporting the conclusions of this article are available in the smallAnimalMRgHIFU repository, DOI:10.5281/zenodo.51633,
https://github.com/poormanme/smallAnimalMRgHIFU.

5.7 Acknowledgments

The authors would like to acknowledge Dr. Fiona Yull, Whitney Barham, and Stephanie Dudzinski for their aid in maintaining the mouse colony and providing murine tumor models. Also Michael Siebold for the egg phantom photograph.

Chapter 6

CONTRIBUTIONS AND FUTURE WORK

6.1 Summary and Conclusions

This work seeks to further enable the use of MRI for guidance of thermal therapies and push the field of minimally invasive thermal therapies towards widespread clinical use. Minimally-invasive, interventional therapies are a viable alternative to more invasive surgical approaches, reducing damage to health tissue while locally targeting the area of interest. This selectivity can improve patient outcomes, reduce treatment recovery times, and reduce overhead costs. Imaging guidance is necessary to ensure a successful treatment and many modalities have been explored for this purpose. MRI can provide superior soft-tissue contrast and real-time feedback in the form of therapeutic temperature maps, but challenges remain before this technique can be applied in challenging cases such as adipose tissue and near metal. This dissertation tackled two of the main challenges - erroneous MR thermometry in fatty tissues and near metal probes, and the high cost and limited access to MRgFUS equipment for clinically-relevant studies. In Chapter 3 a model-based thermometry technique was developed that corrected temperature errors in mixed water and fat tissues. This method was shown to be robust to tissue motion, spatiotemporally-varying off-resonance shifts, and could enable more robust MR thermometry guidance in fatty tissues such as breast and liver. It uses state-of-the-art, iterative water/fat separation in a real-time compatible manner. By performing water/fat separation prior to heating and fitting subsequent images to a model-based solver, the method provides accurate PRFS thermometry in fatty tissues without requiring separations to be computed during heating. Chapter 4 developed a novel multi-echo Z-shimming sequence with MR imaging simulator for offline optimization. The sequence was proven capable of recovering signal and temperature precision near metal ablation probes without requiring tuning of the sequence to a given probe angle and slice geometry. This

work will enable temperature mapping near metallic needles and ablation probes for guidance of ablations. Finally, an open-source, low-cost, entry-level MRgFUS system was developed in Chapter 5. This modular system was validated extensively and can conduct sonications in small animals under closed-loop feedback. The system was provided open-source to the focused ultrasound community in hopes of lowering the barrier to performing pilot MRgFUS studies.

6.2 Impact and Innovation

This work provides enabling technologies that address the current limits of MR thermometry to push the bounds of minimally invasive therapies. Firstly, it promotes the use of multiple gradient echo sequences in PRFS-based thermometry. Multiple echo information is underutilized in monitoring of clinical MR-guided treatments, yet it can provide a plethora of additional information that can be used to improve temperature mapping. Previous work has shown that multiple echoes can be used to separate water and fat, eliminate phase wrapping errors, and reduce chemical shift distortions, all of which are much needed improvements to the current standard of care [18, 23, 111]. We further took advantage of multiple echo information to integrate a seamles hybrid referenceless multibaseline thermometry approach [15] with both water/fat separation and metal artifact correction. This integration mitigates two common sources of artifacts in MR thermometry and does so in an optimized, real-time-compatible manner. Secondly, it promotes the use of open-source science to push the field of MR-guided therapies forward. The majority of this work is based on underlying algorithms, whether it be optimization, model-fitting, or system control. By making this work freely available to the research community the research is not only straightforward to reproduce, but easier to implement and adapt for individual purposes.

The water fat thermometry algorithm bootstraps the estimation of field drift from both fat and water to enable spartsity-regularized thermometry to be used in areas of diffuse heating. This coupling of water and fat for estimation across multiple echoes also makes

the algorithm robust to a wide range of regularization parameter choices which could allow for straightforward integration of this method into the clinic without the need to tune for specific treatment scenarios. Finally, fat-separated thermometry with just a single echo has not been implemented previously to this work. This enhancement could make the method more broadly applicable in situations where temporal resolution is critical and the number of echoes that can be acquired is limited. This leaves room for the integration of fat contrast mechanisms into conventional PRFS thermometry in a manner that is robust to motion and scanner drift.

The multi-echo Z-shim presents a unique method for sequence optimization, building upon existing work in magnetic susceptibility characterization. Using a simulated optimization allows the sequence to be tuned a single time offline for a given device and magnetic field strength, which will help standardize imaging protocols during treatments using metallic ablators. This work builds off the widely-used gradient echo sequence with PRFS temperature contrast, avoiding time constraints that come with multi-spectral spin echo imaging and the need for calibration with T_1-based thermometry that other metal artifact correction methods use. This will make integration of the method into clinical thermometry protocols more straightforward to enable further development of novel, minimally invasive ablation techniques such as transforamenal hippocampal ablation [74].

The open-source MR-guided ultrasound system is the first of its kind to be distributed to the community. Purchasing a commercial system can be costly, especially when at the beginning stages of a research project. Many groups of researchers have implemented their own systems with a wide variety of features, some of which are encompassed in this system. However, doing so requires significant investment of time and expertise to validate and no systems have been provided open-source. The entry-level, do-it-yourself MRgFUS system that is described in this work is already validated for closed loop control, reducing start-up costs and lowering the barrier to exploration of the many clinically-relevant applications of FUS.

6.3 Future Work

6.3.1 Multi-contrast sequences

The water/fat separated thermometry method corrects PRFS temperature errors in fatty tissues and performs accurately for fat fractions from 0% to 90% fat but fails in 100% fat. A natural extension of this work would be to incorporate multiple contrast mechanisms to perform thermometry even in 100% fat. This has been attempted before through mixed T_1/PRFS techniques [48]. However these methods must avoid contamination of fat and water signals between the two mechanisms. Incorporation of the model-based technique described in Chapter 3 with the variable flip angle T_1 mapping of Ref. [48] could correct the PRFS signal without fat suppression and incorporate T_1 contrast mechanisms. The ℓ_1 regularization used in the proposed water/fat thermometry method could also be used to regularize apparent heating due to T_1 changes by building the T_1-induced magnitude change into the model as a function of heating, similarly to the joint PRFS/T_1 estimation proposed in Ref. [155]. Changes in T_2^* with temperature could also be incorporated using the signal decay across multiple echoes. Coupling of these mechanisms with PRFS could help enforce data consistency between temperature changes measured with each metric and enable thermometry over the whole range of fat fractions. MR fingerprinting offers another approach for acquiring multi-contrast data during heating. This technique has been shown to be sensitive to many MR tissue parameters including T_1, T_2, M_0, the apparent diffusion coefficient, and off-resonance, and can rapidly acquire maps of these parameters with a gradient echo sequence [156, 157]. The sensitivities of these parameters in both water and fat could be incorporated into the MR fingerprinting dictionary and acquired simultaneously.

6.3.2 Metal artifact correction for interventions

The orientation-independence of the optimized Z-shim thermometry sequence offers a unique opportunity for metal artifact correction around needles and devices of different ge-

ometries. Beyond thermal guidance for ablation, the metal artifact correction abilities of the Z-shim work could be useful in guidance of other interventional procedures involving susceptibility-mismatched materials such as biopsy and brachytherapy. Current MR-guided methods for biopsy rely on gradient echo images for real-time feedback about the probe insertion which are marked by signal loss and artifacts near the inserted needle. In order to confirm final needle placement spin echo images are used, which inherently correct the artifacts but require more time to acquire than gradient echo sequences. For applications near neurological and vascular structures where precise guidance is critical, spin echo images are used primarily which can slow down the rate of imaging feedback [158]. The multiple echo Z-shimmed technique could be used in these applications to recover the areas of lost signal without compromising on acquisition speed. In brachytherapy applications, where radioactive seeds are inserted into a target of interest, precise localization of the seeds is important for calculating the radioactive dose delivered to the patient but is made challenging by the susceptibility artifacts caused by the seeds. These oblong seeds are around 4.5 mm in length and can be distributed in any orientation with respect to the magnetic field [159]. Particularly with the orientation-independence of the proposed Z-shim master scheme, the optimized Z-shim could be useful in recovering this signal and localizing the brachytherapy seeds. The orientation-independence of the Z-shim method could also be useful in monitoring heating near ablation probes of non-linear geometries such as transforamenal hippocampal ablation [74], where helical nitinol needles are used to match the hippocampus shape. Extending this, applications such as deep brain stimulation electrode placement require precise electrode placement while avoiding heating due to induced current from the magnetic fields [75]. The optimized multiple echo Z-shim could be useful for not just localizing the electrode but ensuring safety by monitoring unintended heating of the electrode during insertion.

6.3.3 Low-field needle imager

Despite the advantages of good tissue contrast and real-time localization, MRI-based interventional procedures are not widely used in the clinic, in part because they add to already high clinical demand for MRI scanners, which can be limiting for many sites. Low-field portable MRI systems have seen development in recent years and are capable of producing images comparable to that of higher field strengths [160]. Coupled with the fact that distortions due to susceptibility mismatching are lower at decreased field strengths [158], development of a low-field scanner could be a promising approach to minimize distortion from needles and reduce the cost of using MRI for such procedures. For needle-based techniques such as biopsy and brachytherapy delivery, the cost and added complexity of using MR guidance is too high when readily-available techniques such as ultrasound guidance are cheaper and much more readily available. [161]. A low-field system with optimized Z-shim master sequence could be designed and deployed as a tool in a practitioner's office for rapid, orientation-independent artifact correction and guidance of these needle-based therapies. This would allow Z-shimming to be used to further reduce distortions near the metal needles without needing to calibrate the imaging for each needle or image orientation.

6.3.4 Bioeffects of FUS

The constructed open-source MRgFUS system's closed-loop feedback system lends itself well to the exploration of FUS parameters and how they relate to downstream bioeffects. For example, immunotherapy with FUS is an active area of research and it has been shown that different strengths and duration of FUS application can effect the amount of immunomodulation [162]. This system could be used to more closely examine this relationship under a controlled setting. Another area of interest is in neuromodulation, where mechanical FUS disruption is thought to trigger a neurological response. However, the mechanisms behind the activation or inhibition of activity are only beginning to be explored. Recently it was

proposed that FUS neuromodulation could be due to an auditory startle reflex and not focal activation [163]. This system could be used to explore these effects in detail with controlled testing in small animals. Due to its inherent modularity, additional mechanisms of neuronal activation, such as laser, could be integrated into the system to directly compare the *in vivo* response of the two methods of neuromodulation in order to better understand the underlying biological mechanisms activated by FUS.

BIBLIOGRAPHY

[1] Stephan Clasen, Hansjörg Rempp, Rüdigger Hoffmann, Hansjörg Graf, Philippe L. Pereira, and Claus D. Claussen. Image-guided radiofrequency ablation of hepatocellular carcinoma (HCC): Is MR guidance more effective than CT guidance? *European Journal of Radiology*, 83(1):111–116, 2014.

[2] Jon T Willie, Nealen G Laxpati, Daniel L Drane, Ashok Gowda, Christina Appin, Chunhai Hao, Daniel J Brat, Sandra L Helmers, Amit Saindane, Sherif G Nour, and Robert E Gross. Real-Time Magnetic Resonance-Guided Stereotactic Laser Amygdalohippocampotomy for Mesial Temporal Lobe Epilepsy. *Neurosurgery*, 74(6):569–585, 2014.

[3] Matthew T. Silvestrini, Elizabeth S. Ingham, Lisa M. Mahakian, Azadeh Kheirolomoom, Yu Liu, Brett Z. Fite, Sarah M. Tam, Samantha T. Tucci, Katherine D. Watson, Andrew W. Wong, Arta M. Monjazeb, Neil E. Hubbard, William J. Murphy, Alexander D. Borowsky, and Katherine W. Ferrara. Priming is key to effective incorporation of image-guided thermal ablation into immunotherapy protocols. *JCI Insight*, 2(6):1–16, 2017.

[4] Nathan McDannold, Sigrid L Fossheim, Henrik Rasmussen, Heather Martin, Natalia Vykhodtseva, and Kullervo Hynynen. Heat-activated liposomal MR contrast agent: initial in vivo results in rabbit liver and kidney. *Radiology*, 230(3):743–752, 2004.

[5] Stephen Sapareto and William Dewey. Thermal dose determination in cancer therapy. *Journal of Radiation Oncology Biology Physics*, 10(February):787–800, 1984.

[6] R. Martin Arthur, W. L. Straube, J. W. Trobaugh, and E. G. Moros. Non-invasive estimation of hyperthermia temperatures with ultrasound. *International Journal of Hyperthermia*, 21(6):589–600, 2005.

[7] Dennis L. Parker, Vernon Smith, Philip Sheldon, Lawrence E. Crooks, and Lauren Fussel. Temperature distribution measurements in two dimensional NMR imaging. 10:321–325, 1983.

[8] Nikol Snoeren, Joost Juiskens, Arjen M. Rijken, Arian R. van Hillegersberg, Richard, va Erkel, Gerrit D. Slooter, Joost M. Klaase, Petrousjka M. van den Tol, Fibo J.W. Ten Kate, Maarten C. Jansen, and Thomas M. van Gulik. Viable Tumor Tissue Adherent to Needle Applicators after Local Ablation: A Risk Factor for Local Tumor Progression. *Annals of Surgical Oncology*, 18:3702–3710, 2011.

[9] J. C. Hindman. Proton Resonance Shift of Water in the Gas and Liquid States. *J. Chem. Phys.*, 44(12):4582, 1966.

[10] J. De Poorter, C. De Wagter, Y. De Deene, C. Thomsen, F. Stahlberg, and E. Achten. The Proton-Resonance-Frequency-Shift Method Compared with Molecular Diffusion for Quantitative Measurement of Two-Dimensional Time-Dependent Temperature Distribution in a Phantom. *J. Magn. Reson.*, Series B(103):234–241, 1994.

[11] Y Ishihara, A Calderon, H Watanabe, K Okamoto, Y Suzuki, K Kuroda, and Y Suzuki. A precise and fast temperature mapping using water proton chemical shift. *Magnetic Resonance in Medicine*, 34:814–823, 1995.

[12] Viola Rieke and Kim Butts Pauly. MR thermometry. *Journal of magnetic resonance imaging : JMRI*, 27:376–390, feb 2008.

[13] Karl K Vigen, Bruce L Daniel, John M Pauly, and Kim Butts. Triggered, navigated, multi-baseline method for proton resonance frequency temperature mapping with respiratory motion. *Magnetic resonance in medicine*, 50:1003–10, nov 2003.

[14] Viola Rieke, Karl K. Vigen, Graham Sommer, Bruce L. Daniel, John M. Pauly, and Kim Butts. Referenceless PRF shift thermometry. *Magnetic Resonance in Medicine*, 51:1223–1231, 2004.

[15] William A. Grissom, Viola Rieke, Andrew B. Holbrook, Yoav Medan, Michael Lustig, Juan Santos, Michael V. McConnell, and Kim Butts Pauly. Hybrid referenceless and multibaseline subtraction MR thermometry for monitoring thermal therapies in moving organs. *Medical Physics*, 37(9):5014–26, 2010.

[16] Sébastien Roujol, Mario Ries, Bruno Quesson, Chrit Moonen, and Baudouin Denis de Senneville. Real-time MR-thermometry and dosimetry for interventional guidance on abdominal organs. *Magn. Reson. Med.*, 63:1080–7, apr 2010.

[17] Cory R. Wyatt, Brian J. Soher, and James R. MacFall. Correction of breathing-induced errors in magnetic resonance thermometry of hyperthermia using multiecho field fitting techniques. *Med. Phys.*, 37(12), 2010.

[18] Pooja Gaur, Ari Partanen, Beat Werner, Pejman Ghanouni, Rachelle Bitton, Kim Butts Pauly, and William A. Grissom. Correcting heat-induced chemical shift distortions in proton resonance frequency-shift thermometry. *Magn. Reson. Med.*, 76:172–182, 2016.

[19] Bryant T. Svedin, Allison Payne, and Dennis L. Parker. Respiration artifact correction in three-dimensional proton resonance frequency MR thermometry using phase navigators. *Magn. Reson. Med.*, 76:206–213, 2016.

[20] Rudolf Stollberger, Peter W. Ascher, Dietrich Huber, Werner Renhart, Herbert Radner, and Franz Ebner. Temperature monitoring of interstitial thermal tissue coagulation using MR phase images. *J. Magn. Reson. Imaging*, 8:188–196, 1997.

[21] Roel Deckers, Laura Merckel, B Denis de Senneville, Gerald Schubert, Max Kohler, Floor Knuttel, W P Th M Mali, Chrit T W Moonen, M A A J van den Bosch, and L W Bartels. Performance analysis of a dedicated breast MR-HIFU system for tumor ablation in breast cancer patients. *Phys. Med. Biol.*, 60:5527–42, 2015.

[22] H E Cline, K Hynynen, E Schneider, C J Hardy, S E Maier, R D Watkins, and F a Jolesz. Simultaneous magnetic resonance phase and magnitude temperature maps in muscle. *Magnetic resonance in medicine : official journal of the Society of Magnetic Resonance in Medicine / Society of Magnetic Resonance in Medicine*, 35(3):309–315, 1996.

[23] Robert V. Mulkern, Lawrence P. Panych, Nathan J. McDannold, Ferenc a. Jolesz, and Kullervo Hynynen. Tissue temperature monitoring with multiple gradient-echo imaging sequences. *J. Magn. Reson. Imaging*, 8(2):493–502, 1998.

[24] C. H. Meyer, J. M. Pauly, A. Macovski, and D. G. Nishimura. Simultaneous spatial and spectral selective excitation. *Magn. Reson. Med.*, 15(2):287–304, 1990.

[25] William a Grissom, Adam B Kerr, Andrew B Holbrook, John M Pauly, and Kim Butts-Pauly. Maximum linear-phase spectral-spatial radiofrequency pulses for fat-suppressed proton resonance frequency-shift MR Thermometry. *Magn. Reson. Med.*, 62(5):1242–50, nov 2009.

[26] Thorsten A. Bley, Oliver Wieben, Christopher J. Francois, Jean H. Brittain, and Scott B. Reeder. Fat and Water Magnetic Resonance Imaging. *Journal of Magnetic Resonance Imaging*, 31:4–18, 2010.

[27] Valentina Taviani, Diego Hernando, Christopher J. Francois, Ann Shimakawa, Karl K. Vigen, Scott K. Nagle, Mark L. Schiebler, Thomas M. Grist, and Scott B. Reeder. Whole-Heart Chemical Shift Encoded Water–Fat MRI. *Magnetic Resonance in Medicine*, 72:718–725, 2014.

[28] WT Dixon. Simple proton spectroscopic imaging. *Radiology*, 153, 1984.

[29] G H Glover and E Schneider. Three-point Dixon technique for true water/fat decomposition with B0 inhomogeneity correction. *Magn. Reson. Med.*, 18:371–83, apr 1991.

[30] D Hernando, P Kellman, JP Haldar, and ZP Liang. Robust Water/Fat Separation in the Presence of Large Field Inhomogeneities Using a Graph Cut Algorithm. *Magn. Reson. Med.*, 63(1):79–90, 2010.

[31] Johan Berglund and Joel Kullberg. Three-dimensional water/fat separation and T2* estimation based on whole-image optimization–application in breathhold liver imaging at 1.5 T. *Magn. Reson. Med.*, 67:1684–93, jun 2012.

[32] Houchun Harry Hu, Peter Börnert, Diego Hernando, Peter Kellman, Jingfei Ma, Scott Reeder, and Claude Sirlin. ISMRM workshop on fat-water separation: Insights, applications and progress in MRI. *Magn. Reson. Med.*, 68:378–388, 2012.

[33] Kagayaki Kuroda. Non-invasive MR thermography using the water proton chemical shift. *International Journal of Hyperthermia*, 21(6):547–560, 2005.

[34] Nathan McDannold, Agnieszka Szot Barnes, Frank J Rybicki, Koichi Oshio, Nan-kuei Chen, Kullerbo Hynynen, and Robert V Mulkern. *Magnetic Resonance in Medicine*, 58:1117–1123, 2007.

[35] Bruno Quesson, Jacco a. De Zwart, and C. T W Moonen. Magnetic resonance temperature imaging for guidance of thermotherapy. *Journal of Magnetic Resonance Imaging*, 12(4):525–533, 2000.

[36] Andriy V Shmatukha, Paul R Harvey, and Chris J G Bakker. Correction of proton resonance frequency shift temperature maps for magnetic field disturbances using fat signal. *Journal of magnetic resonance imaging*, 25:579–87, mar 2007.

[37] K Kuroda, R V Mulkern, K Oshio, L P Panych, T Nakai, T Moriya, S Okuda, K Hynynen, F a Jolesz, and F a Joles. Temperature Mapping Using the Water Proton Chemical Shift: Self-Referenced Method with Echo-Planar Spectroscopic Imaging. *Magnetic Resonance in Medicine*, 43(2):220–5, 2000.

[38] Temperature monitoring with line scan echo planar spectroscopic imaging. *Medical Physics*, 28(3):346–355, 2001.

[39] Brian A. Taylor, Ken Pin Hwang, Andrew M. Elliott, Anil Shetty, John D. Hazle, and R. Jason Stafford. Dynamic chemical shift imaging for image-guided thermal therapy: Analysis of feasibility and potential. *Medical Physics*, 35(2):793–803, 2008.

[40] Cheng Li, Xinyi Pan, Kui Ying, Qiang Zhang, Jing An, Dehe Weng, Wen Qin, and Kuncheng Li. An internal reference model-based PRF temperature mapping method with cramer-rao lower bound noise performance analysis. *Magnetic Resonance in Medicine*, 62(5):1251–1260, 2009.

[41] E Brian Welch, Aliya Gifford, and Theodore F Towse. Phantom validation of temperature mapping using fat-water MRI with explicit fitting of water peak location. In *Proceedings of the 22nd Anual Meeting of ISMRM, Milan, Italy*, page 3673, 2014.

[42] Brian A. Taylor, Andrew M. Elliott, Ken-Pin Hwang, Anil Shetty, John D. Hazle, and R. Jason Stafford. Measurement of temperature dependent changes in bone marrow using a rapid chemical shift imaging technique. *Journal of Magnetic Resonance Imaging*, 33(5):1128–1135, 2011.

[43] Brian J. Soher, Cory Wyatt, Scott B. Reeder, and James R. MacFall. Noninvasive temperature mapping with MRI using chemical shift water-fat separation. *Magnetic Resonance in Medicine*, 63:1238–1246, 2010.

[44] Lorne W Hofstetter, Desmond T B Yeo, W Thomas Dixon, James G Kempf, Cynthia E Davis, and Thomas K Foo. Fat-referenced MR thermometry in the breast and prostate using IDEAL. *J. Magn. Reson. Imaging*, 36:722–32, sep 2012.

[45] Bryant T. Svedin, Allison Payne, Bradley D. Bolster, and Dennis L. Parker. Multi-echo pseudo-golden angle stack of stars thermometry with high spatial and temporal

resolution using k-space weighted image contrast. *Magnetic Resonance in Medicine*, 79(3):1407–1419, 2018.

[46] Multicoil Dixon chemical species separation with an iterative least-squares estimation method. 51:35–45, 2004.

[47] Kagayaki Kuroda, Taku Iwabuchi, Makoto Obara, Masatoshi Honda, Kensuke Saito, and Yutaka Imai. Temperature dependence of relaxation times in proton components of fatty acids. *Magnetic Resonance in Medicine*, 10(3):177–83, 2011.

[48] Nick Todd, Mahamadou Diakite, Allison Payne, and Dennis L. Parker. Hybrid proton resonance frequency/T1 technique for simultaneous temperature monitoring in adipose and aqueous tissues. *Magnetic Resonance in Medicine*, 69:62–70, 2013.

[49] Kullervo Hynynen, Nathan McDannold, Robert V. Mulkern, and Ferenc A. Jolesz. Temperature monitoring in fat with MRI. *Magnetic Resonance in Medicine*, 43(6):901–904, 2000.

[50] Paul Baron, Mario Ries, Roel Deckers, Martijn De Greef, Jukka Tanttu, Max Kohler, Max A. Viergever, Chrit T W Moonen, and Lambertus W. Bartels. In vivo T2-based MR thermometry in adipose tissue layers for high-intensity focused ultrasound near-field monitoring. *Magnetic Resonance in Medicine*, 72(4), 2014.

[51] Eugene Ozhinsky, Maureen P Kohi, Pejman Ghanouni, and Viola Rieke. T2-based temperature monitoring in abdominal fat during MR-guided focused ultrasound treatment of patients with uterine fibroids. *J. Ther. Ultrasound*, 3(15):1–10, 2015.

[52] Paul Baron, Roel Deckers, Floor M. Knuttel, and Lambertus W. Bartels. T1 and T2 temperature dependence of female human breast adipose tissue at 1.5 T: Groundwork for monitoring thermal therapies in the breast. *NMR in Biomedicine*, 28(11):1463–1470, 2015.

[53] Sara M. Sprinkhuizen, Maurits K. Konings, Martijn J. Van Der Bom, Max a. Viergever, C. J G Bakker, and Lambertus W. Bartels. Temperature-induced tissue susceptibility changes lead to significant temperature errors in PRFS-based MR thermometry during thermal interventions. *Magn. Reson. Med.*, 64:1360–1372, 2010.

[54] Sara M. Sprinkhuizen, Chris J G Bakker, Johannes H. Ippel, Rolf Boelens, Max a. Viergever, and Lambertus W. Bartels. Temperature dependence of the magnetic volume susceptibility of human breast fat tissue: An NMR study. *Magn. Reson. Mater. Physics, Biol. Med.*, 25:33–39, 2012.

[55] Robert D. Peters, R. Scott Hinks, and R. Mark Henkelman. Heat-source orientation and geometry dependence in proton-resonance frequency shift magnetic resonance thermometry. *Magnetic Resonance in Medicine*, 41(5):909–918, 1999.

[56] Paul Baron, Roel Deckers, Job G. Bouwman, Chris J. G. Bakker, Martijn de Greef, Max A. Viergever, Chrit T. W. Moonen, and Lambertus W. Bartels. Influence of water and fat heterogeneity on fat-referenced MR thermometry. *Magnetic Resonance in Medicine*, 75:1187–1197, 2015.

[57] Paul Baron, Roel Deckers, Martijn de Greef, Laura G Merckel, Chris J G Bakker, Job G Bouwman, Ronald L a W Bleys, Maurice a a J van den Bosch, and Lambertus W Bartels. Correction of proton resonance frequency shift MR-thermometry errors caused by heat-induced magnetic susceptibility changes during high intensity focused ultrasound ablations in tissues containing fat. *Magnetic resonance in medicine : official journal of the Society of Magnetic Resonance in Medicine / Society of Magnetic Resonance in Medicine*, 72(6):1580–9, dec 2014.

[58] Bryant Svedin, Allison Payne, and Dennis Parker. Rapid, simultaneous multiparametric thermometry using a signle reference variable flip angle T1 method. In *International Society for Therapeutic Ultrasound Symposium*, 2018.

[59] Nick Todd, Mahamadou Diakite, Allison Payne, and Dennis L Parker. In vivo evaluation of multi-echo hybrid PRF/T1 approach for temperature monitoring during breast MR-guided focused ultrasound surgery treatments. *Magnetic Resonance in Medicine*, 72(3):793–9, 2014.

[60] Brian A. Hargreaves, Pauline W. Worters, Kim Butts Pauly, John M. Pauly, Kevin M. Koch, and Garry E. Gold. Metal-induced artifacts in MRI. *American Journal of Roentgenology*, 197(3):547–555, 2011.

[61] K M Koch, B a Hargreaves, K Butts Pauly, W Chen, G E Gold, and K F King. Magnetic resonance imaging near metal implants. *Journal of Magnetic Resonance Imaging*, 32(4):773–787, 2010.

[62] Z H Cho, D J Kim, and Y K Kim. Total inhomogeneity correction including chemical shifts and susceptibility by view angle tilting. *Medical physics*, 15(7):7–11, 1988.

[63] Kim Butts, John M. Pauly, and Garry E. Gold. Reduction of blurring in view angle tilting MRI. *Magnetic Resonance in Medicine*, 53(2):418–424, 2005.

[64] D. Gensler, F. Fidler, P. Ehses, M. Warmuth, T. Reiter, M. Düring, O. Ritter, M. E. Ladd, H. H. Quick, P. M. Jakob, W. R. Bauer, and P. Nordbeck. MR safety: Fast T1 thermometry of the RF-induced heating of medical devices. *Magnetic Resonance in Medicine*, 68(5):1593–1599, 2012.

[65] Hans Weber, Valentina Taviani, Daehyun Yoon, Pejman Ghanouni, Kim Butts Pauly, and Brian A. Hargreaves. MR thermometry near metallic devices using multispectral imaging. *Magnetic Resonance in Medicine*, 00:1–8, 2016.

[66] Kevin M. Koch, John E. Lorbiecki, R. Scott Hinks, and Kevin F. King. A multispectral three-dimensional acquisition technique for imaging near metal implants. *Magnetic Resonance in Medicine*, 61(2):381–390, 2009.

[67] Wenmiao Lu, Kim B. Pauly, Garry E. Gold, John M. Pauly, and Brian A. Hargreaves. Slice encoding for metal artifact correction with noise reduction. *Magnetic Resonance in Medicine*, 65(5):1352–1357, 2011.

[68] Hans Weber, Brian A. Hargreaves, and Bruce L. Daniel. Artifact-reduced imaging of biopsy needles with 2D multispectral imaging. *Magnetic Resonance in Medicine*, 80:655–661, 2018.

[69] Hans Weber, Pejman Ghanouni, Aurea Pascal-Tenorio, Kim Butts Pauly, and Brian A. Hargreaves. MRI monitoring of focused ultrasound sonications near metallic hardware. *Magnetic Resonance in Medicine*, 00:1–13, 2017.

[70] Christophe Aubé, Diethard Schmidt, Jens Brieger, Martin Schenk, Thomas Helmberger, Claudius W. Koenig, Fritz Schick, Claus D. Claussen, and Philippe L. Pereira. Magnetic Resonance Imaging Characteristics of Six Radiofrequency Electrodes in a Phantom Study. *Journal of Vascular and Interventional Radiology*, 15(4):385–392, 2004.

[71] Philipp Ehses, Florian Fidler, Peter Nordbeck, Eberhard D. Pracht, Marcus Warmuth, Peter M. Jakob, and Wolfgang R. Bauer. MRI thermometry: Fast mapping of RF-induced heating along conductive wires. *Magnetic Resonance in Medicine*, 60(2):457–461, 2008.

[72] Olivier Seror, Matthieu Lepetit-Coiffé, Brigitte Bail, Baudouin Denis Senneville, Hervé Trillaud, Chrit Moonen, and Bruno Quesson. Real time monitoring of radiofrequency ablation based on MR thermometry and thermal dose in the pig liver in vivo. *European Radiology*, 18(2):408–416, 2008.

[73] John A. Moriarty, Julian C. Chen, Carrie M. Purcell, Lee C. Ang, R. Scott Hinks, Robert D. Peters, R. Mark Henkelman, Donald B. Plewes, Michael J. Bronskill, and Walter Kucharczyk. MRI monitoring of interstitial microwave-induced heating and

thermal lesions in rabbit brain in vivo. *Journal of Magnetic Resonance Imaging*, 8(1):128–135, 1998.

[74] David B Comber, E Bryn Pitt, Hunter B Gilbert, Matthew W Powelson, Emily Matijevich, Joseph S Neimat, Robert J Webster III, and Eric J Barth. Optimization of Curvilinear Needle Trajectories for Transforamenal Hippocampotomy. *Operative Neurosurgery: Instrumentation and Technique*, 0(0):1–7, 2016.

[75] Devashish Shrivastava, Aviva Abosch, John Hughes, Ute Goerke, Lance DelaBarre, Rachana Visaria, Noam Harel, and J T Vaughan. Heating induced near Deep Brain Stimulation Lead Electrodes during Magnetic Resonance Imaging with a 3T Transceive Volume Head Coil. *Physics in Medicine and Biology*, 57(17):5651–5665, 2012.

[76] Jan Henry Seppenwoolde, Max A. Viergever, and Chris J G Bakker. Passive tracking exploiting local signal conservation: The white marker phenomenon. *Magnetic Resonance in Medicine*, 50(4):784–790, 2003.

[77] Adrienne E. Campbell-Washburn, Toby Rogers, Hui Xue, Michael S. Hansen, Robert J. Lederman, and Anthony Z. Faranesh. Dual echo positive contrast bSSFP for real-time visualization of passive devices during magnetic resonance guided cardiovascular catheterization. *Journal of cardiovascular magnetic resonance : official journal of the Society for Cardiovascular Magnetic Resonance*, 16:88, 2014.

[78] Jens Frahm, Klaus-Dietmar Merboldt, and Wolfgang Hanicke. Direct FLASH MR Imaging of Magnetic Field Inhomogeneities by Gradient Compensation. *Magnetic Resonance in Medicine*, 480:474–480, 1988.

[79] R T Constable and D D Spencer. Composite Image Formation in z -Shimmed Functional MR Imaging. 117(1988):110–117, 1999.

[80] Yuxin Zhang, Megan E Poorman, and William A Grissom. Dual echo z-shimmed pro-

ton resonance frequency-shift MR thermometry near metallic ablation probes: Technique and temperature precision. *Magnetic Resonance in Medicine*, 78, 2017.

[81] Katrina F. Chu and Damian E. Dupuy. Thermal ablation of tumours: biological mechanisms and advances in therapy. *Nat. Rev. Cancer*, 14:199–208, 2014.

[82] J Arnott. Practical illustrations of the remedial efficacy of a very low or anesthetic temperature in cancer. *West. J. Med. Surg.*, page 154, 1851.

[83] Irving S. Cooper. Cryogenic Surgery of the Basal Ganglia. *J. Am. Med. Assoc.*, 181(7):600–604, 1962.

[84] William T. Bovie. Electrosurgical Apparatus: No 1,813,902, 1931.

[85] W.J. Fry, J.W. Barnard, F.J. Fry, R.F Krumins, and J.F. Brennan. Ultrasonic Lesions in the Mammalian Central Nervous System. *Science (80-.).*, 122(3168):517–518, 1955.

[86] A J Welch, M Motamedi, S Rastegar, G L LeCarpentier, and D Jansen. Laser thermal ablation. *Photochem. Photobiol.*, 53(6):815–823, 1991.

[87] Thomas J. Vogl, Ralf Straub, Katrin Eichler, Dirk Woitaschek, and Martin G. Mack. Malignant Liver Tumors Treated with MR Imaging guided Laser induced Thermotherapy: Experience with Complications in 899 Patients (2,520 lesions). *Radiology*, 225(2):367–377, 2002.

[88] Muneeb Ahmed, Christopher L. Brace, Fred T. Lee, and S. Nahum Goldberg. Principles of and Advances in Percutaneous Ablation. *Radiology*, 258(2):351–369, 2011.

[89] D. Haemmerich and P. F. Laeseke. Thermal tumour ablation: Devices, clinical applications and future directions. *Int. J. Hyperth.*, 21(8):755–760, 2005.

[90] S. Nahum Goldberg, G. Scott Gazelle, and Peter R. Mueller. Thermal Ablation Therapy for Focal Malignancy. *Am. J. Roentgenol.*, 174(2):323–331, 2000.

[91] Chris J. Diederich. Thermal ablation and high-temperature thermal therapy: Overview of technology and clinical implementation. *Int. J. Hyperth.*, 21(8):745–753, 2005.

[92] Y. Ni, S. Mulier, Y. Miao, L. Michel, and G. Marchal. A review of the general aspects of radiofrequency ablation. *Abdom. Imaging*, 30:381–400, 2005.

[93] Ender Gunes Yegin, Erkan Oymaci, Emrah Karatay, and Ahmet Coker. Progress in surgical and nonsurgical approaches for hepatocellular carcinoma treatment. *Hepatobiliary Pancreat. Dis. Int.*, 15(3):234–256, 2016.

[94] Dieter Haemmerich. Biophysics of Radiofrequency Ablation. *Crit. Rev. Biomed. Eng.*, 38(1):53–63, 2010.

[95] Stephan Clasen and Philippe L. Pereira. Magnetic resonance guidance for radiofrequency ablation of liver tumors. *J. Magn. Reson. Imaging*, 27(2):421–433, 2008.

[96] Steffen L. Hokland, Michael Pedersen, Rares Salomir, Bruno Quesson, Hans Stødkilde-Jørgensen, and Chrit T W Moonen. MRI-guided focused ultrasound: Methodology and applications. *IEEE Transactions on Medical Imaging*, 25(6):723–731, 2006.

[97] Li-Feng Ran, Xun-Peng Xie, Ji-Zhu Xia, Fang-Lin Xie, Yan-Min Fan, and Feng Wu. Specific antitumour immunity of HIFU-activated cytotoxic T lymphocytes after adoptive transfusion in tumour-bearing mice. *International Journal of Hyperthermia*, pages 1–7, 2015.

[98] Azadeh Kheirolomoom, Elizabeth S. Ingham, Lisa M. Mahakian, Sarah M. Tam, Matthew T. Silvestrini, Spencer K. Tumbale, Josquin Foiret, Neil E. Hubbard, Alexander D. Borowsky, William J. Murphy, and Katherine W. Ferrara. CpG expedites regression of local and systemic tumors when combined with activatable nanodelivery. *Journal of Controlled Release*, 220:253–264, 2015.

[99] W Jeffrey Elias, Diane Huss, Tiffini Voss, Johanna Loomba, Mohamad Khaled, Eyal Zadicario, Robert C Frysinger, Scott a Sperling, Scott Wylie, Stephen J Monteith, Jason Druzgal, Binit B Shah, Madaline Harrison, and Max Wintermark. A pilot study of focused ultrasound thalamotomy for essential tremor. *The New England journal of medicine*, 369:640–8, 2013.

[100] Seung Schik Yoo, Alexander Bystritsky, Jong Hwan Lee, Yongzhi Zhang, Krisztina Fischer, Byoung Kyong Min, Nathan J. McDannold, Alvaro Pascual-Leone, and Ferenc a. Jolesz. Focused ultrasound modulates region-specific brain activity. *NeuroImage*, 56:1267–1275, 2011.

[101] K Hynynen, N McDannold, N Vykhodtseva, and F a Jolesz. Noninvasive MR imaging-guided focal opening of the blood-brain barrier in rabbits. *Radiology*, 220:640–646, 2001.

[102] Shengping Qin and Katherine W. Ferrara. Acoustic resoponse of compliable microvessels containing ultrasound contrast agents. *Phys. Med. Biol.*, 51(20):5065–5088, 2006.

[103] Adam Maxwell, Gabe Owens, Hitinder Gurm, Kimberly Ives, Daniel Myers, and Zhen Xu. Noninvasive treatment of deep venous thrombosis using pulsed ultrasound cavitation therapy (histotripsy) in a porcine model. *Journal of Vascular Interventional Radiology*, 22(3), 2011.

[104] Vera A. Khokhlova, J. Brian Fowlkes, William W. Roberts, George R. Schade, Zhen Xu, Tatiana D. Khokhlova, Timothy L. Hall, Adam D. Maxwell, Yak-Nam Wang, and Charles A. Cain. Histotripsy methods in mechanical disintegration of tissue: Towards clinical applications. *International Journal of Hyperthermia*, 31(2):145–162, 2015.

[105] Diseases and Conditions Overview, 2018.

[106] Y-F Zhou. High intensity focused ultrasound in clinical tumor ablation. *World J. Clin. Oncol.*, 2(1):8–27, 2011.

[107] M. Sherar, F. F. Liu, M. Pintilie, W. Levin, J. Hunt, R. Hill, J. Hand, C. Vernon, G. Van Rhoon, J. Van Der Zee, D. G. Gonzalez, J. Van Dijk, J. Whaley, and D. Machin. Relationship between thermal dose and outcome in thermoradiotherapy treatments for superficial recurrences of breast cancer: Data from a phase III trial. *International Journal of Radiation Oncology Biology Physics*, 39(2):371–380, 1997.

[108] Justin P McWilliams, Edward W Lee, Shota Yamamoto, Christopher T Loh, and Stephen T Kee. Image-Guided Tumor Ablation : Emerging Technologies and Future Directions. *Seminars in Interventional Radiology*, 27(3):302–313, 2010.

[109] Rajan Ramanathan and Raymond J. Leveillee. Ablative therapies for renal tumors. *Therapeutic Advances in Urology*, 2(2):51–68, 2010.

[110] Anderanik Tomasian, Adam N WAllace, Travis J Hillen, and Jack W Jennings. Percutaneous Ablation in Painful Bone Tumors. *Seminars in Musculoskeletal Radiology*, 20(5):472–485, 2016.

[111] D Hernando, ZP Liang, and P Kellman. Chemical Shift-Based Water/Fat Separation: A Comparison of Signal Models. *Magn. Reson. Med.*, 64(3):811–822, 2010.

[112] Diego Hernando, C D G Hines, H Yu, and Scott B. Reeder. Addressing Phase Errors in Fat-Water Imaging Using a Mixed Magnitude/Complex Fitting Method. *Magn. Reson. Med.*, 67(3):638–644, 2012.

[113] Vincent Auboiroux, Magalie Viallon, Joerg Roland, Jean Noël Hyacinthe, Lorena Petrusca, Denis R. Morel, Thomas Goget, Sylvain Terraz, Patrick Gross, Christoph D. Becker, and Rares Salomir. ARFI-prepared MRgHIFU in liver: Simultaneous mapping of ARFI-displacement and temperature elevation, using a fast GRE-EPI sequence. *Magn. Reson. Med.*, 68(3):932–946, 2012.

[114] Jacco a. De Zwart, Frédéric C. Vimeux, Christophe Delalande, Paul Canioni, and Chrit T W Moonen. Fast lipid-suppressed MR temperature mapping with echo-shifted

gradient- echo imaging and spectral-spatial excitation. *Magn. Reson. Med.*, 42(1):53–59, 1999.

[115] Jacco A. De Zwart, Frdric C. Vimeux, Jean Palussire, Rares Salomir, Bruno Quesson, Christophe Delalande, and Chrit T W Moonen. On-line correction and visualization of motion during MRI-controlled hyperthermia. *Magn. Reson. Med.*, 45:128–137, 2001.

[116] R. Jason Stafford, Roger E. Price, Chris J. Diederich, Marko Kangasniemi, Lars E. Olsson, and John D. Hazle. Interleaved echo-planar imaging for fast multiplanar magnetic resonance temperature imaging of ultrasound thermal ablation therapy. *Journal of Magnetic Resonance Imaging*, 20(4):706–714, 2004.

[117] J. I. Sirven. The silent gap between epilepsy surgery evaluations and clinical practice guidelines. *European Journal of Neurology*, 17:522–523, 2010.

[118] Rares Salomir, Baudouin Denis De Senneville, and Chrit T W Moonen. A fast calculation method for magnetic field inhomogeneity due to an arbitrary distribution of bulk susceptibility. *Concepts Magn. Reson. Part B Magn. Reson. Eng.*, 19(1):26–34, 2003.

[119] J. P. Marques and R. Bowtell. Application of a Fourier based method for rapid calculation of field inhomogeneity due to spatial variation of magnetic susceptibility. *Concepts Magn. Reson. Part B Magn. Reson. Eng.*, 25(1):65–78, 2005.

[120] Paul Ramm. *High Field 1 H NMR Spectroscopy on Cell Suspensions of Neural Progenitor Cells and Brain Tumor Initiating Cells.* PhD thesis, DER UNIVERSITAT REGENSBURG, 2011.

[121] Kevin M. Koch, Xenophon Papademetris, Douglas L. Rothman, and Robin A. De Graaf. Rapid calculations of susceptibility induced magnetostatic field perturbations for in vivo magnetic resonance. *Phys. Med. Biol.*, 51(24):6381–6402, 2006.

[122] C. J. Durrant, M. P. Hertzberg, and P. W. Kuchel. Magnetic susceptibility: Further insights into macroscopic and microscopic fields and the sphere of Lorentz. *Concepts in Magnetic Resonance Part A*, 18A(1):72–95, 2003.

[123] John F. Schenck. The role of magnetic susceptibility in magnetic resonance imaging: MRI magnetic compatibility of the first and second kinds. *Med. Phys.*, 23(6):815–850, 1996.

[124] Megan E Poorman and William A Grissom. Orientation-independent Z-shimmed temperature mapping near ablation probes. In *International Society for Magnetic Resonance in Medicine*, 2017.

[125] Yue Chen, Megan E Poorman, David B Comber, E Brynn Pitt, Cindy Liu, Isuru Godage, Yu Hong, William A Grissom, Eric J Barth, and Robert J Webster III. Treating Epilepsy via Thermal Ablation: Initial Experiments with an MRI-Guided Concentric Tube Robot. In *Design of Medical Devices Conference*, 2017.

[126] Axel Krieger, Iulian I Iordachita, Peter Guion, Anurag Singh, Aradhana Kaushal, Cynthia Ménard, Peter Pinto, Kevin Camphausen, Gabor Fichtinger, and Louis Whitcomb. An MRI Compatible Robotic System With Hybrid Tracking for MRI Guided Prostate Intervention. *IEEE transactions on biomedical engineering*, 58(11):3049–3060, 2011.

[127] Megan E Poorman, Vandiver L Chaplin, Ken Wilkens, Mary D Dockery, Todd D Giorgio, William A Grissom, and Charles F Caskey. smallAnimalMRgHIFU https://github.com/poormanme/smallAnimalMRgHIFU, 2016.

[128] Nathan McDannold and Stephan E. Maier. Magnetic resonance acoustic radiation force imaging. *Medical Physics*, 35(8):3748–58, 2008.

[129] Jiming Zhang, Pei-Herng Hor, and Raja Muthupillai. Non Invasive Estimation of Tissue Viscoelasticity from Broad-band Mechanical Excitation Using High Intensity Focused Ultrasound. In *Proc. Intl. Soc. Mag. Reson. Med. 22*, page 6385, 2014.

[130] J. De Poorter, Carlos De Wagter, Yves De Deene, Carsten Thomsen, Freddy Stahlberg, and Eric Achten. Noninvasive MRI thermometry with the proton resonance frequency (PRF) method: In vivio results in Human Muscle. *Magnetic Resonance in Medicine*, 33:74–81, 1995.

[131] AbdEl Monem El-Sharkawy, Michael Schär, Paul a. Bottomley, and Ergin Atalar. Monitoring and correcting spatio-temporal variations of the MR scanner's static magnetic field. *Magnetic Resonance Materials in Physics, Biology and Medicine*, 19:223–236, 2006.

[132] E L Madsen, J a Zagzebski, R a Banjavie, and R E Jutila. Tissue mimicking materials for ultrasound phantoms., 2008.

[133] C T Guy, R D Cardiff, and W J Muller. Induction of mammary tumors by expression of polyomavirus middle T oncogene: a transgenic mouse model for metastatic disease. *Molecular and cellular biology*, 12(3):954–961, 1992.

[134] Kenji Takegami, Yukio Kaneko, Toshiaki Watanabe, Toshiyuki Maruyama, Yoichiro Matsumoto, and Hirokazu Nagawa. Polyacrylamide gel containing egg white as new model for irradiation experiments using focused ultrasound. *Ultrasound in Medicine and Biology*, 30(10):1419–1422, 2004.

[135] Nick Todd, Urvi Vyas, Joshua de Bever, Allison Payne, and Dennis Parker. The Effects of Spatial Sampling Choices on MR Temperature Measurements. 65(2):515–521, 2011.

[136] Chang W Song. Effect of Local Hyperthermiaon Blood Flow and Microenvironment: A Review. *Cancer Research*, 44(OCTOBER):4721–4730, 1984.

[137] W L Lin, R B Roemer, and K Hynynen. Theoretical and experimental evaluation of a temperature controller for scanned focused ultrasound hyperthermia. *Medical physics*, 17(4):615–625, 2012.

[138] N B Smith, N K Merrilees, K Hynynen, and M Dahleh. Control system for an MRI compatible intracavitary ultrasound array for thermal treatment of prostate disease. *International journal of hyperthermia*, 17(3):271–282, 2001.

[139] Megan E Poorman, Mary D Dockery, Stephanie O Dudzinski, Vandiver L Chaplin, Ryan A Spears, Charles F Caskey, Todd D Giorgio, and William A Grissom. Time-resolved in vivo measurements of FUS immunomodulation in a novel reporter mouse model of breast cancer. In *International Society for Therapeutic Ultrasound Symposium*, 2016.

[140] Brett Z Fite, Yu Liu, Dustin E Kruse, Charles F Caskey, Jeffrey H Walton, Chun-Yen Lai, Lisa M Mahakian, Benoit Larrat, Erik Dumont, and Katherine W Ferrara. Magnetic resonance thermometry at 7T for real-time monitoring and correction of ultrasound induced mild hyperthermia. *PloS one*, 7(4):e35509, jan 2012.

[141] Kiam Heong Ang, Gregory Chong, and Yun Li. PID control system analysis, design, and technology. *IEEE Transactions on Control Systems Technology*, 13(4):559–576, 2005.

[142] Andrew B. Holbrook, Juan M. Santos, Elena Kaye, Viola Rieke, and Kim Butts Pauly. Real Time MR Thermometry for Monitoring HIFU Ablations of the Liver. *Magnetic Resonance in Medicine*, 63(2):365–373, 2010.

[143] Chenchen Bing, Joris Nofiele, Robert Staruch, Michelle Ladouceur-Wodzak, Yonatan Chatzinoff, Ashish Ranjan, and Rajiv Chopra. Localised hyperthermia in rodent models using an MRI-compatible high-intensity focused ultrasound system. *International Journal of Hyperthermia*, (November):1–10, 2015.

[144] Hh Pennes. Analysis of tissue and arterial blood temperatures in the resting human forearm. *Journal of applied physiology*, pages 5–34, 1948.

[145] Philips. Sonalleve MR-HIFU Therapy platform, 2016.

[146] Rémi Magnin, Fabien Rabusseau, Frédéric Salabartan, Sébastien Mériaux, Jean-François Aubry, Denis Le Bihan, Erik Dumont, and Benoit Larrat. Magnetic resonance-guided motorized transcranial ultrasound system for blood-brain barrier permeabilization along arbitrary trajectories in rodents. *Journal of Therapeutic Ultrasound*, 3(1):22, 2015.

[147] Matthieu Lepetit-Coiffe, Bruno Quesson, Olivier Seror, Erik Dumont, Brigitte Le Bail, Chrit T. W. Moonen, and Hervé Trillaud. Real-time monitoring of radiofrequency ablation of rabbit liver by respiratory-gated quantitative temperature MRI. *Journal of Magnetic Resonance Imaging*, 24:152–159, 2006.

[148] Shigehiro Morikawa, Toshiro Inubushi, Yoshimasa Kurumi, Shigeyuki Naka, Koichiro Sato, Koichi Demura, Tohru Tani, and Hasnine a Haque. Feasibility of respiratory triggering for MR-guided microwave ablation of liver tumors under general anesthesia. *Cardiovascular and interventional radiology*, 27:370–3, 2004.

[149] Kagayaki Kuroda, Daisuke Kokuryo, Etsuko Kumamoto, Kyohei Suzuki, Yuichiro Matsuoka, and Bilgin Keserci. Optimization of self-reference thermometry using complex field estimation. *Magnetic resonance in medicine*, 56(4):835–43, oct 2006.

[150] McDannold, Kullervo Hynynen, Delia Wolf, Gerald Wolf, Ferenc Jolesz, and Nathan McDannold. MRI evaluation of thermal ablation of tumors with focused ultrasound. *Journal of magnetic resonance imaging : JMRI*, 8:91–100, 1998.

[151] William A. Grissom, Michael Lustig, Andrew B Holbrook, Viola Rieke, John M Pauly, and Kim Butts-Pauly. Reweighted l1 referenceless PRF shift thermometry. *Magnetic resonance in medicine*, 64(4):1068–77, oct 2010.

[152] Baudouin Denis de Senneville, Charles Mougenot, and Chrit T W Moonen. Real-time adaptive methods for treatment of mobile organs by MRI-controlled high-intensity focused ultrasound. *Magnetic Resonance in Medicine*, 57:319–330, feb 2007.

[153] Sébastien Roujol, Mario Ries, Bruno Quesson, Chrit Moonen, and Baudouin Denis De Senneville. Real-time MR-thermometry and dosimetry for interventional guidance on abdominal organs. In *Proceedings International Society of Magnetic Resonance in Medicine 18*, page 1830, 2010.

[154] Rares Salomir, Magalie Viallon, Antje Kickhefel, Joerg Roland, Denis R. Morel, Lorena Petrusca, Vincent Auboiroux, Thomas Goget, Sylvain Terraz, Christoph D. Becker, and Patrick Gross. Reference-free PRFS MR-thermometry using near-harmonic 2-D reconstruction of the background phase. *IEEE Transactions on Medical Imaging*, 31(2):287–301, 2012.

[155] Pooja Gaur and William Grissom. Improved k-space-based MR thermometry by joint PRF phase shift and T1/T2* attenuation estimation. In *Journal of Therapeutic Ultrasound*, volume 3, page P19. BioMed Central Ltd, 2015.

[156] Dan Ma, Vikas Gulani, Nicole Seiberlich, Kecheng Liu, Jeffrey L. Sunshine, Jeffrey L. Duerk, and Mark A. Griswold. Magnetic resonance fingerprinting. *Nature*, 495(7440):187–192, 2013.

[157] Yun Jiang, Dan Ma, Nicole Seiberlich, Vikas Gulani, and Mark a. Griswold. MR fingerprinting using fast imaging with steady state precession (FISP) with spiral readout. *Magnetic Resonance in Medicine*, 00:n/a–n/a, 2014.

[158] Clifford R. Weiss, Sherif Gamal Nour, and Jonathan S. Lewin. MR-guided biopsy: A review of current techniques and applications. *Journal of Magnetic Resonance Imaging*, 27(2):311–325, 2008.

[159] Peter R Seevinck, Hendrik de Leeuw, Clemens Bos, and Chris J G Bakker. Highly localized positive contrast of small paramagnetic objects using 3D center-out radial sampling with off-resonance reception. *Magnetic Resonance in Medicine*, 65(1):146–56, 2011.

[160] Mathieu Sarracanie, Cristen D. LaPierre, Najat Salameh, David E. J. Waddington, Thomas Witzel, and Matthew S. Rosen. Low-Cost High-Performance MRI. *Scientific Reports*, 5:15177, 2015.

[161] R Jason Stafford, Ivan A Brezovich, and Colin G Orton. Image-guided prostate brachytherapy should be MRI-based. *Medical Physics*, 43(12):6213–6216, 2016.

[162] Johan Unga and Mitsuru Hashida. Ultrasound induced cancer immunotherapy. *Advanced Drug Delivery Reviews*, 72:144–153, 2014.

[163] Tomokazu Sato, Mikhail G. Shapiro, and Doris Y. Tsao. Ultrasonic Neuromodulation Causes Widespread Cortical Activation via an Indirect Auditory Mechanism. *Neuron*, 98:1031–1041.e5, 2018.